

Cyanobacterial Photosystem II in a native-like superstructure at 2.44 Å resolution and first serial femtosecond X-ray studies

vorgelegt von Diplom Chemikerin
Julia Hellmich
aus Bonn

von der Fakultät II
Mathematik und Naturwissenschaften
der Technischen Universität Berlin
zur Erlangung des akademischen Grades
Doktor der Naturwissenschaften
Dr. rer. nat.

genehmigte Dissertation

Promotionsausschuss:

Vorsitzender: Prof. Dr. N. Budisa

Gutachterin: Prof. Dr. A. Zouni

Gutachter: Prof. Dr. T. Friedrich

Gutachter: Prof. Dr. B. Grimm

Tag der wissenschaftlichen Aussprache: 2.10.2014

Berlin 2014

D83

Zusammenfassung

Photosystem II (PSII) ist ein homodimerer Protein-Kofaktor-Komplex und ein Schlüsselenzym in der Elektronentransportkette der Photosynthese, in der Wasser und Kohlenstoffdioxid zu Sauerstoff und Kohlenhydraten umgewandelt werden. PSII befindet sich in der Thylakoidmembran von Pflanzen, Algen und Cyanobakterien. Nach der Absorption von Licht im Reaktionszentrum von PSII wird Wasser am katalytischen Zentrum, einem Mn_4CaO_5 -Cluster, oxidiert. Der detaillierte Mechanismus der Wasseroxidation ist bislang ungeklärt. Um diesen einzigartigen katalytischen Mechanismus und die native strukturelle Anordnung des PSII Komplexes aufzuklären, werden hochqualitative PSII Kristalle benötigt.

Der erste Teil dieser Arbeit konzentriert sich auf die Optimierung der Kristallisation von dimeren PSII Kernkomplexen (dPSIIcc) des Cyanobakteriums *Thermosynechococcus elongatus*. Dafür wurde eine neue Extraktions-, Aufreinigungs- und Kristallisationsprozedur entwickelt, bei der ausschließlich das Detergenz Octaethyleneglycolmonododecylether ($C_{12}E_8$), anstelle des sonst üblichen n-dodecyl- β -D-maltoside (β DM) verwendet wurde. Das Detergenz β DM kokristallisiert mit den dPSIIcc (zu Membranproteinkristallen des Typs II) und wurde teilweise in die dPSIIcc eingebaut, weswegen ein destabilisierender Effekt auf die native dPSIIcc-Form angenommen wurde. Mit der neuen Prozedur wurden fast ausschließlich dPSIIcc und nur minimale Mengen monomerer PSIIcc erhalten, wobei alle 20 Proteinuntereinheiten vorhanden sind, einschließlich der Proteinuntereinheit PsbY, welche zumindest teilweise in allen vorherigen PSIIcc-Kristallstrukturen fehlte. Zunächst erzielten die erhaltenen Typ II-Kristalle Röntgenbeugungsdaten mit maximal 6 Å Auflösung. Eine Kristallisationsnachbehandlung der dPSIIcc Kristalle mit PEG 5000 MME bewirkte die Extraktion von Wasser und $C_{12}E_8$ und wandelte die Kristalle zu Typ I-Membrankristallen um (Kristallpackung ohne kokristallisierte Detergenzgürtel), was zu einer verbesserten Auflösung von 2.44 Å führte. Die transformierten Kristalle zeigen die dPSIIcc in Reihen angeordnet, so wie sie durch Elektronenmikroskopie von cyanobakteriellen Thylakoidmembranen gefunden wurden. Die perfekte Übereinstimmung deutet darauf hin, dass die Röntgendiffraktionsdaten das erste hochaufgelöste Model von nativen dPSIIcc Superstrukturen liefern. Mögliche Folgerungen dieser Anordnung für die effiziente Nutzung der Sonnenenergie werden betrachtet.

Der zweite Teil dieser Arbeit konzentriert sich auf die Aufklärung des fünfschrittigen katalytischen Zyklus der Wasseroxidation am Mn_4CaO_5 -Cluster. Röntgendiffraktion an Synchrotronquellen führt zu Strahlenschädigung in den PSII Kristallen, welche Änderungen der Oxidationsstufen und der Mn-Mn Abstände im Mn_4CaO_5 -Cluster hervorruft. Eine neue Methode, in der in Serie geschaltete femtosekunden-Röntgenkristallographie in Kombination mit Röntgenemission benutzt wird, wurde mit dPSIIcc-Mikrokristallen durchgeführt. Mit dieser Methode konnten Daten vor dem Beginn von Strahlenschädigung bei Raumtemperatur aufgenommen werden. Präsentiert werden erste Daten von dPSIIcc Kristallen im dunkeladaptierten Zustand und im ersten belichteten Zustand. Ein negativer Einfluss des stark reduzierenden Röntgenlasers auf den Mn_4CaO_5 -Cluster konnte experimentell durch zeitgleiche Röntgenemissionsmessungen und den Vergleich mit Datensätzen von Synchrotronquellen ausgeschlossen werden. Mit dieser Arbeit wird ein erster Schritt hin zur Aufklärung des katalytischen Zyklus der Wasseroxidation präsentiert.

Abstract

Photosystem II (PSII) is a homodimeric protein-cofactor complex and a key enzyme of the electron transport chain of photosynthesis, the process where water and carbon dioxide are transformed to oxygen and carbohydrates. PSII is located in the thylakoid membrane of plants, algae and cyanobacteria. After the absorption of sunlight in PSII, water is oxidized at its catalytic center, a Mn_4O_5Ca -cluster. The detailed mechanism of water oxidation is yet unclear. To study this unique catalytic mechanism and the native structural organization of the PSII complex, high quality PSII crystals are needed.

The first part of the present work focuses on the optimization of the crystallization of the dimeric PSII core complex (dPSIIcc) from the cyanobacterium *Thermosynechococcus elongatus*. A new extraction, purification and crystallization procedure was established using the detergent octaethyleneglycolmonododecylether ($C_{12}E_8$) instead of the commonly used n-dodecyl- β -D-maltoside (β DM). The detergent β DM was found co-crystallized with dPSIIcc (type II membrane protein crystals) and was partly incorporated in the PSII complex, thereby it was assumed to destabilize the native dPSIIcc form. With the new procedure, almost exclusively dPSIIcc and only minimal amounts of monomeric PSIIcc are obtained. All 20 protein subunits are completely present including PsbY, which was at least partly absent in all earlier PSIIcc crystal structures. Initially, the obtained crystals were of type II and yielded X-ray diffraction (XRD) data of at most 6 Å resolution. A post-crystallization treatment with PEG 5000 MME effected an extraction of water and $C_{12}E_8$ and converted the dPSIIcc crystals to type I membrane protein crystals (packing without co-crystallized detergent belts), which resulted in an improved resolution of 2.44 Å. The transformed crystals show dPSIIcc packed in rows as found by electron microscopy of cyanobacterial thylakoid membranes. The perfect match suggests the new XRD data to represent the first high-resolution model of native dPSIIcc superstructures. Possible implications of this arrangement for an efficient use of solar energy are considered.

The second part of this work focuses on the elucidation of the five-step catalytic cycle of water oxidation at the Mn_4CaO_5 -cluster. The commonly established method of XRD at synchrotron sources leads to radiation damage within PSII crystals. A new method called serial femtosecond X-ray crystallography with combined XRD and X-ray emission (XES) was applied to dPSIIcc microcrystals. The method allows for data collection before the onset of radiation damage at room temperature. Here, first XRD and XES data of dPSIIcc crystals in the dark adapted state and the first illuminated state are presented. A negative impact of the highly reducing X-ray laser on the protein integrity and the radiation sensitive Mn_4O_5Ca -cluster could be excluded by simultaneous XES measurements and the comparison with XRD data sets obtained at synchrotron sources. With this work, a first step towards the elucidation of the catalytic cycle of water oxidation is presented.

Publications

Parts of the present work have been published in:

J. Hellmich, M. Bommer, A. Burkhardt, M. Ibrahim, J. Kern, A. Meents, F. Müh, H. Dobbek, A. Zouni, *Native-like photosystem II-superstructure at 2.44 Å resolution through detergent extraction from the protein crystal*, *Structure*, vol. 22, pp. 1–9, Nov, 2014.

J. Kern, R. Alonso-Mori, R. Tran, J. Hattne, R. J. Gildea, N. Echols, C. Glöckner, J. Hellmich, et al., “*Simultaneous femtosecond X-ray spectroscopy and diffraction of photosystem II at room temperature.*,” *Science*, vol. 340, no. 6131, pp. 491–5, Apr. 2013.

R. G. Sierra, H. Laksmono, J. Kern, R. Tran, J. Hattne, R. Alonso-Mori, B. Lassalle-Kaiser, C. Glöckner, J. Hellmich, et al., “*Nanoflow electrospinning serial femtosecond crystallography.*,” *Acta Crystallogr. D. Biol. Crystallogr.*, vol. 68, no. Pt 11, pp. 1584–7, Nov. 2012.

R. Alonso-Mori, J. Kern, R. J. Gildea, D. Sokaras, T.-C. Weng, B. Lassalle-Kaiser, R. Tran, J. Hattne, H. Laksmono, J. Hellmich, et al. , “*Energy-dispersive X-ray emission spectroscopy using an X-ray free-electron laser in a shot-by-shot mode.*,” *Proc. Natl. Acad. Sci. U. S. A.*, vol. 109, no. 47, pp. 19103–7, Nov. 2012.

J. Kern, R. Alonso-Mori, J. Hellmich, R. Tran, J. Hattne, et al. , “*Room temperature femtosecond X-ray diffraction of photosystem II microcrystals.*,” *Proc. Natl. Acad. Sci. U. S. A.*, vol. 109, no. 25, pp. 9721–6, Jun. 2012.

Further publications:

R. Tran, J. Kern, J. Hattne, S. Koroidov, J. Hellmich, et al., “*The Mn₄Ca photosynthetic water-oxidation catalyst studied by simultaneous X-ray spectroscopy and crystallography using an X-ray free-electron laser.*,” *Phil. Trans. R. Soc. B*, vol. 369, no. 1647, July 2014.

J. Hattne, N. Echols, R. Tran, J. Kern, R. J. Gildea, A. S. Brewster, R. Alonso-Mori, C. Glöckner, J. Hellmich, et al. , “*Accurate macromolecular structures using minimal measurements from X-ray free-electron lasers.*,” *Nat. Methods*, vol. 11, pp. 545-548, Mar. 2014.

M. Brecht, S. Skandary, J. Hellmich, C. Glöckner, A. Konrad, M. Hussels, A. J. Meixner, A. Zouni, and E. Schlodder, “*Spectroscopic properties of photosystem II core complexes from *Thermosynechococcus elongatus* revealed by single-molecule experiments.*,” *Biochim. Biophys. Acta*, vol. 1837, no. 6, pp. 773-781, Feb. 2014.

F. Müh, C. Glöckner, J. Hellmich, and A. Zouni, “*Light-induced quinone reduction in photosystem II.*,” *Biochim. Biophys. Acta*, vol. 1817, no. 1, pp. 44–65, Jan. 2012.

A. Guskov, A. Gabdulkhakov, M. Broser, C. Glöckner, J. Hellmich, J. Kern, J. Frank, F. Müh, W. Saenger, and A. Zouni, “*Recent progress in the crystallographic studies of photosystem II.*,” *Chemphyschem A Eur. J. Chem. Phys. Phys. Chem.*, vol. 11, no. 6, pp. 1160–1171, Apr. 2010.

Talks:

Crystal structure of Photosystem II purified and crystallized with a new introduced detergent – September 2013, 4th Joint MX Meeting, Berlin, Germany

Recent developments in Photosystem II crystals – June 2013, Department of plant physiology, Prof. Grimm, HU Berlin, Germany

Recent developments in Photosystem II crystals- slimming for the summer – June 2013, Retreat of the CRC 1078, Protonation dynamics in protein function, Erkner, Germany

Advances in the structural and functional elucidation of cyanobacterial Photosystem II – November 2010, UniCat mini symposium: Biological catalysis, TU Berlin, Germany

Integral Lipids in the structure of cyanobacterial Photosystem II – Invited speaker, July 2010, Sydney University, Australia

Poster presentations:

Integral Lipids in the structure of cyanobacterial Photosystem II, August 2010, 15th International Congress of Photosynthesis, Beijing, China

Integral Lipids in the structure of cyanobacterial Photosystem II, July 2010, 19th International Symposium on Plant Lipids, Cairns, Australia

Structure-function analysis of the cyanobacterial Photosystem II at 2.9 Ångstrom resolution, May 2010, SAB-Meeting, UniCat, FU Berlin

Group guidance:

Blualgen und die Photosynthese – Lange Nacht der Wissenschaften 2011, May 2011, TU Berlin, German

Abbreviations

BESSY	Berliner Elektronenspeicherring-Gesellschaft für Synchrotronstrahlung
BN-PAGE	Blue native polyacrylamide gel electrophoresis
C ₁₂ E ₈	octaethyleneglycolmonododecylether
Car	carotenoid
Chl	chlorophyll
CMC	critical micelle concentration
CSC	critical solubilization concentration
CSPAD	Cornell-SLAC Pixel Array Detector
CV	column volume
CXI	Coherent X-ray Imaging
cyt	cytochrome
DEAE	diethylaminoethyl
DESY	Deutsches Elektronen Synchrotron
DGDG	digalatosyldiacylglycerol
dPSIIcc	dimeric Photosystem II core complex
EET	excitation energy transfer
EM	electron microscopy
ENDOR	electron nuclear double resonance
EPR	electron paramagnetic resonance
ET	electron transfer
EXAFS	extended X-ray absorption fine structure
Fd	ferredoxin
FNR	ferredoxin-NADP-oxidoreductase
fs	femtosecond
FTIR	Fourier transform infrared
GDVN	gas dynamic virtual nozzle
HPF	high pressure freezing
HTG	n-Heptyl-β-D-thiogluco-side
HZB	Helmholtz-Zentrum Berlin
ID	inner diameter
LCLS	Linac Coherent Light Source
L _{CM}	core-membrane linker
LHC	Light harvesting complex
MES	2-(N-morpholino)ethanesulfonic acid
MGDG	monogalactosyldiacylglycerol

MIMS	Membrane-inlet mass spectrometry
mPSIIcc	monomeric Photosystem II core complex
NADPH	Nicotinamide adenine dinucleotide phosphate
OD	optical density
OEC	oxygen evolving complex
PC	plastocyanin
PDB	protein data bank
PEG	polyethylene glycol
PG	phosphatidylglycerol
Pheo	pheophytin
PQ	plastoquinone
PQH ₂	plastoquinol
PsbA-Z	protein encoded by the according PSII gene <i>psbA-Z</i>
PSI	Photosystem I
PSIIcc	Photosystem II core complex
Q _A	fixed plastoquinone
Q _B	mobile plastoquinone
Q _C	mobile plastoquinone
RC	reaction center
RT	room temperature
SFX	Serial femtosecond Crystallography
SLAC	Stanford Linear Accelerator Center
SQDG	sulfoquinovosyldiacylglycerol
SR	synchrotron radiation
<i>T. elongatus</i>	<i>Thermosynechococcus elongatus</i>
<i>T. vulcanus</i>	<i>Thermosynechococcus vulcanus</i>
TMH	transmembrane helix
UNL	unknown ligand
WOC	water oxidizing complex
XAS	X-ray absorption spectroscopy
XES	X-ray emission spectroscopy
XFEL	X-ray free electron laser
XRD	X-ray diffraction
βDM	n-Dodecyl-β-D-maltoside

Content

Zusammenfassung.....	I
Abstract.....	III
Publications.....	V
Abbreviations.....	IX
Content.....	XI
1 Introduction.....	1
1.1 Evolution of Photosynthesis - The basis for all aerobic life.....	1
1.2 Overview of oxygenic photosynthesis.....	2
1.2.1 Light harvesting.....	2
1.2.2 Reaction center.....	4
1.2.3 Photosynthetic membrane.....	5
1.2.4 Photosynthetic reactions.....	8
1.3 Photosystem II.....	11
1.3.1 Elucidation of the PSII core complex structure.....	11
1.3.2 Overall structure.....	12
1.3.3 The protein subunits.....	14
1.3.4 Overall function.....	18
1.3.5 Cofactors.....	19
1.3.6 Integral lipids.....	23
1.3.7 Structure of the Water oxidizing complex.....	28
1.3.8 The water oxidation site.....	29
1.3.9 Chloride and Calcium binding sites.....	32
1.4 Membrane protein crystallization.....	36
1.4.1 Crystallization of PSIIcc.....	40
1.4.2 X-ray radiation damage.....	42
1.4.3 Serial femtosecond X-ray Crystallography at an XFEL.....	46
1.5 Aims of this work.....	48
2 Materials and methods.....	50
2.1 Chemicals, buffers and materials.....	50
2.2 Methods.....	51
2.2.1 Cell cultivation.....	51
2.2.2 Preparation of thylakoid membranes.....	51
2.2.3 Protein solubilization.....	52
2.2.4 Protein purification.....	52
2.2.5 Chlorophyll <i>a</i> concentration measurements.....	53
2.2.6 Crystallization of dPSIIcc for SR XRD measurements.....	54
2.2.7 Size exclusion chromatography.....	54
2.2.8 Oxygen evolution measurements.....	54

2.2.9	Mass spectrometry	55
2.2.10	Blue native polyacrylamide gel electrophoresis	55
2.2.11	High pressure freezing	56
2.2.12	X-ray diffraction data collection	56
2.2.13	Critical Micelle Concentration measurements	57
2.2.14	XFEL diffraction data collection and processing	58
2.2.15	X-ray emission spectroscopy	58
2.2.16	XES / XFEL diffraction data collection and processing	60
3	Purification and crystallization of dPSIIcc using C ₁₂ E ₈	62
3.1	Purification procedure for PSIIcc with C ₁₂ E ₈	63
3.2	Characterization of dPSIIcc	66
3.2.1	Oxygen evolution activity	66
3.2.2	Size exclusion chromatography	67
3.2.3	Blue Native polyacrylamide gel electrophoresis	68
3.2.4	Mass Spectrometry	69
3.3	Crystallization of dPSIIcc	73
3.4	SR XRD measurements of dPSIIcc crystals	74
3.5	Structure of C ₁₂ E ₈ -dPSIIcc	76
3.5.1	Cofactors	77
3.5.2	Manganese cluster and Ca ²⁺ and Cl ⁻ binding sites	78
3.5.3	Lipids and detergent content	80
3.6	Crystal packing	84
3.7	CMC measurements	91
3.8	Summary	93
4	Serial femtosecond X-ray diffraction and X-ray emission spectroscopy of dPSIIcc microcrystals	95
4.1	Experimental setup for Serial Femtosecond Crystallography	97
4.2	Preparation of dPSIIcc microcrystals	99
4.3	Room temperature femtosecond X-ray diffraction of dPSIIcc microcrystals	103
4.4	Simultaneous fs XRD and XES measurements of dPSIIcc microcrystals	109
4.5	Summary	115
5	Outlook	116
	Figures and Tables	117
	References	119
	Danksagung	134

1 Introduction

1.1 Evolution of Photosynthesis - The basis for all aerobic life

It is believed that the earth was formed about 4.6 billion years ago. More than 3.5 billion years ago the conditions on earth were still harsh and inappropriate for aerobic life (1). A high pressure carbon dioxide atmosphere and an acidic ocean without any dissolved oxygen were present. Additionally the surface was blasted with unfiltered ultraviolet light. Then first organisms developed photosynthetic activity. The bacteria and primitive algae started to perform anoxygenic photosynthesis, which later developed to oxygenic photosynthesis (2). In anoxygenic photosynthesis the electron source is an inorganic substance, like hydrogen sulfide, instead of water. About 2 billion years ago, with the beginning of the oxygenic photosynthesis, cyanobacteria used water as an electron donor and released molecular oxygen into the atmosphere. The oxygen began to accumulate and aerobic life found an environment to develop and sustain. This fundamental happening produced the oxygen needed for cellular respiration and a protecting ozone layer (3, 4). Today cyanobacteria, plants and algae perform oxygenic photosynthesis by splitting water and transforming carbon dioxide to carbohydrates, using sunlight as an energy source and releasing molecular oxygen as a byproduct. All living creatures depend on photosynthesis as it provides oxygen for respiration and all organic compounds, like sugars, carbohydrates, lipids and proteins that build the biomass which serves for food. The total energy of sunlight that hits the earth is 1.2×10^{21} kcal/year. It was estimated that 6×10^{17} kcal/year of the total energy is used for photosynthesis, which corresponds to less than 0.1 % of the total sunlight energy available. With this amount of light energy, photosynthetic organisms produce 200 billion tons of biomass per year and fix ca 10 % of the total atmospheric carbon dioxide (1).

1.2 Overview of oxygenic photosynthesis

1.2.1 Light harvesting

The process of light conversion into a chemically amenable form starts with the absorption of sunlight by light harvesting pigment molecules. The major light absorbing molecules exhibit a tetrapyrrole π -electron ring system; in cyanobacteria chlorophyll *a* (Chl*a*) with a central ligated magnesium ion and its demetallation product the pheophytin *a* (Pheo*a*) are the two forms found. They absorb the light at a region around $\lambda = 430$ nm and $\lambda = 670$ nm. In other organisms closely related tetrapyrroles like chlorophyll *b* (Chl*b*), and bacteriochlorophyll *a* and *b*, which are incorporated in purple bacteria, can be found. In cyanobacteria the two classes of accessory pigments are the phycobilins and the caretonoids. Phycobilins are non-cyclic, open tetrapyrroles which are responsible for the distinctive color of cyanobacteria and red algae. In cyanobacteria two forms exist, the phycocyanobilin and phycoerythrobilin. Both are linked via a covalent thioether into phycobiliproteins. These assemble to phycobilisomes (5) and are further connected to the photosynthetic proteins by a core-membrane linker (L_{CM}) to build the functional major extrinsic antenna systems (6). Their light absorption maxima are in the region around $\lambda = 500$ nm and $\lambda = 650$ nm and fill the absorption gap of Chl*a* and the carotenoids. The latter are the third class of pigment cofactors which absorb at lower wavelength in a region between $\lambda = 430$ nm and $\lambda = 470$ nm. In cyanobacteria β -carotene, lutein and zeaxanthin are the most common forms. Carotenoids have a linear chain of conjugated isoprene units and different modifications at their cyclic ionone end groups. Together the three classes of pigment molecules capture almost the entire range of visible light. The chemical structures and the absorption spectra of the main photosynthetic pigments are shown in Figure 1-1, Figure 1-2 and Figure 1-3.

Introduction

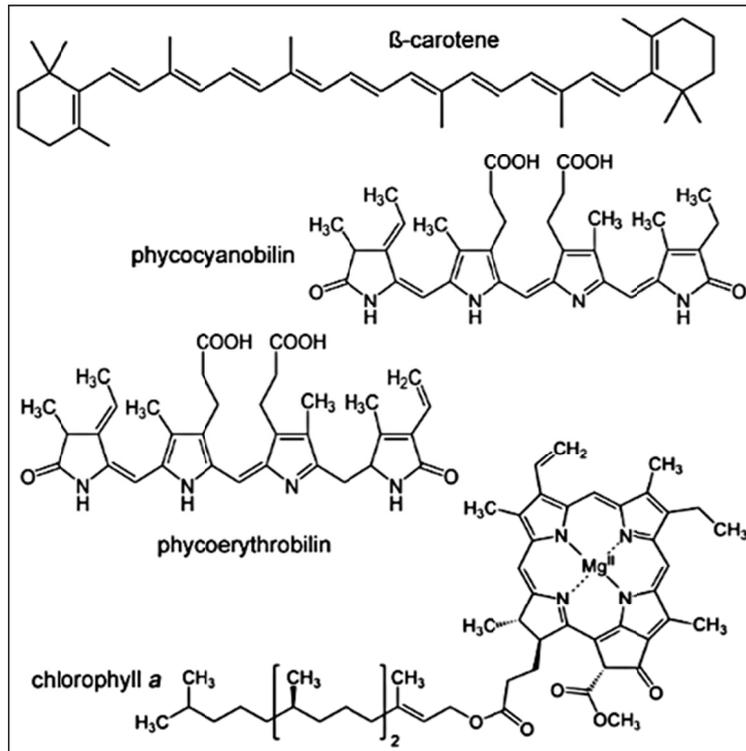


Figure 1-1 The light absorbing pigments of cyanobacteria

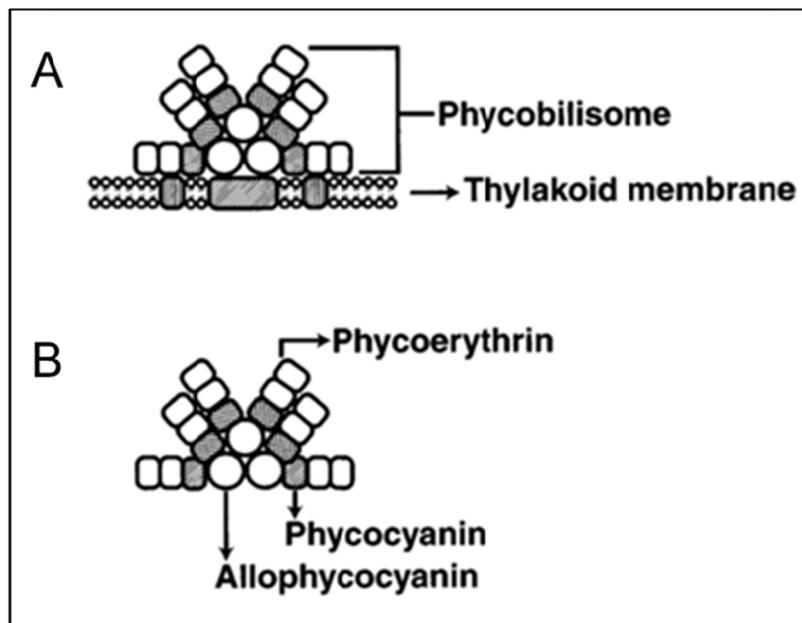


Figure 1-2 Model of a tricylindrical hemidiscoidal phycobilisome

A) A phycobilisome attached to photosystem II (rectangle in the thylakoid membrane) and two adjacent photosystem I particles (small rectangles in the thylakoid membrane) B) The tricylindrical core of the phycobilisome is built by allophycocyanin (lowest energy pigment). The cylinders are built by phycocyanin (intermediate energy pigment) and phycoerythrin (high energy pigment). The organization allows energy flow from the highest to the lowest energy pigment. Figure taken from (5), with kind permission from Elsevier.

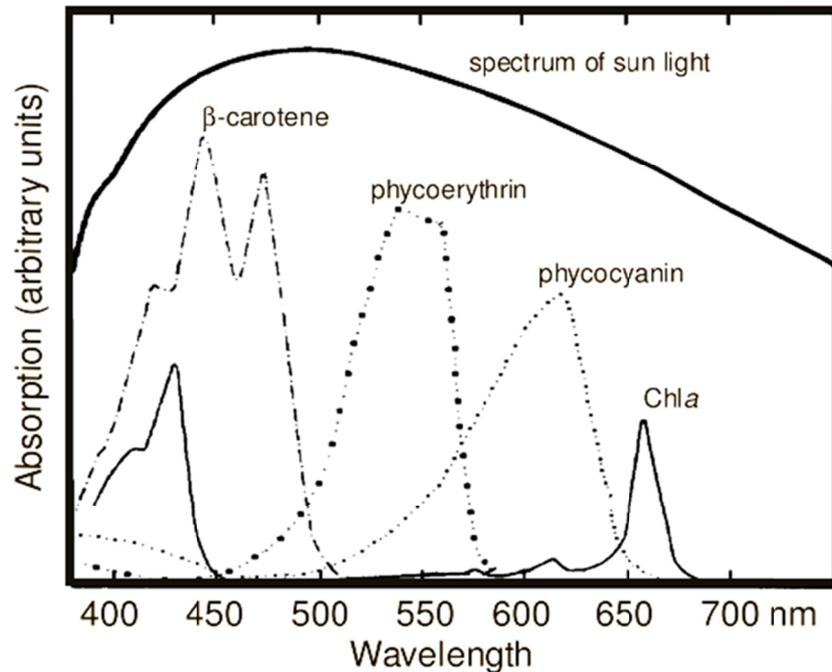


Figure 1-3 The light absorbing pigments of cyanobacteria

Absorption wavelength spectra of photosynthetic pigments in comparison with the solar irradiation of the sun. Figure taken from (1), with kind permission from Springer Science and Business Media.

1.2.2 Reaction center

All photosynthetic organisms can be categorized according to their photochemical reaction center unit. Type I reaction centers (RC) contain iron-sulfur proteins as electron acceptor, while type II RCs utilize pheophytin as the primary electron acceptor and quinones as the secondary electron acceptors. The bacterial photosystems are all anoxygenic and belong only to one of the two types of RCs. Purple bacteria and green filamentous bacteria possess a type II RC, whereas green sulfur bacteria and heliobacteria are provided with the type I RC. Cyanobacteria and higher plants possess a photosystem I (a type I RC) and a photosystem II (a type II RC); the combination enables them to perform oxygenic photosynthesis (4). Photosystem II (PSII) shows high structural similarity to the purple bacterial RC (7) which suggests an evolutionary relation. Cyanobacteria are photoautotrophic prokaryotes and belong to the group of bacteria of the phylogenetic tree, one large group beside the archaea and the eucarya. In the endosymbiotic theory the

chloroplasts of eukaryotic algae and green plants (both belong to the eucarya) evolved by the encapsulation of an ancestral cyanobacterium into a eukaryotic host cell (8). The here presented studies are conducted with PSII of the thermophilic cyanobacterium *Thermosynechococcus elongatus* BP1 (*T. elongatus*), mainly with dimeric PSII core complexes (dPSIIcc), which lack the light harvesting phycobilisomes. The organism originates from a hot spring in Beppu, Japan (9). A second dPSIIcc structure is discussed later which results from the thermophilic cyanobacterium *T. vulcanus*. The PSII of the two cyanobacteria is identical in the amino acid sequence with the exception of Alanine 286 in subunit D1 of *T. vulcanus*, which is a Threonine in *T. elongatus*. The genome of *T. elongatus* is fully unraveled (10), but since the cell growth of *T. elongatus* is photoautotrophic, mutations that reduce or prevent photosynthetic activity will result in reduced or no cultivation yield. Sugiura et al. have developed a mutagenesis system of PSII from *T. elongatus* that allows cultivation with efficient yield that is needed for crystallization (11). The crystallization of PSIIcc from the mesophilic cyanobacterium *Synechocystis* sp. PCC 6803, which is optimal for mutation studies, is not yet possible due to protein instability (12). Thermophilic organisms have a high growth temperature (ca 55°C) which avoids cross-contaminations with other bacteria. Further they show a high protein stability and robustness which is an essential advantage for purification, crystallization and storage of PSII.

1.2.3 Photosynthetic membrane

Photosynthetic protein complexes are directionally embedded in a lipid bilayer, the thylakoid membrane. In plants these membranes are located in the chloroplasts, where they form associated stacks of membranes (grana) connected through intergranal thylakoids (lamellae), which arrange throughout the stroma region (13). Cyanobacteria lack chloroplasts and the differentiation into grana and lamellae is not made. They form parallel sheets of thylakoid membranes, in most species these end close to the plasma membrane. The exact arrangement of the thylakoids in the cytoplasm is species-dependent; in *Synechococcus* they form concentric layers. The larger distance between the thylakoid sheets, compared to chloroplast thylakoids, provides the space that is needed for the large external light harvesting

phycobilisomes. The interior part of a thylakoid is the aqueous lumen, which is separated from the exterior region, the cytoplasm (14). Up to almost 50 % of the thylakoid mass consists of four different types of lipids, divided into the uncharged lipids monogalactosyldiacylglycerol (MGDG) and digalatosyldiacylglycerol (DGDG), and the charged lipids sulfoquinovosyldiacylglycerol (SQDG) and phosphatidylglycerol (PG). The lipid composition of thylakoid membranes is highly conserved among photosynthetic organisms with ~ 50 % MGDG, ~ 30 % DGDG, ~ 5-12 % SQDG and ~ 5-12 % PG (15). They form the matrix for the four proteins that are part of the electron transport chain of oxygenic photosynthesis: PSII, cytochrome (cyt) b_6f , photosystem I (PSI) and ATP synthase (Figure 1-4). Additionally, the soluble electron carrier ferredoxin is present at the cytoplasmic side of the membrane and the soluble electron carrier plastocyanin is present at the luminal side of the membrane. A plastoquinone pool in the hydrophobic interior part of the membrane permits the electron transport between PSII and cyt b_6f .

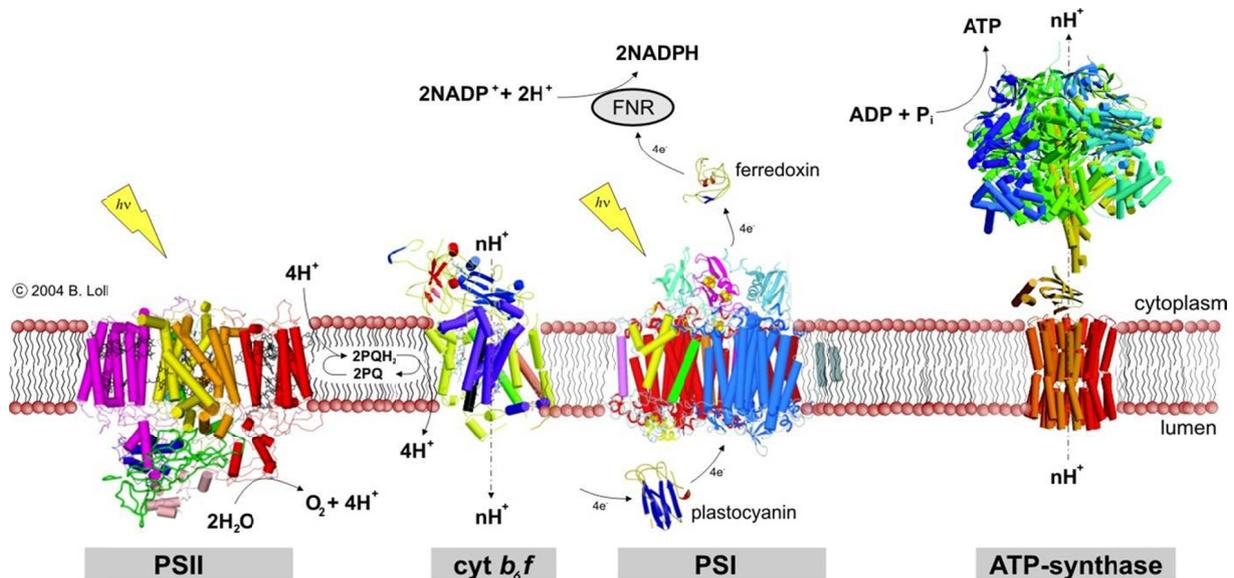


Figure 1-4 Schematic side view of a thylakoid membrane with incorporated integral membrane protein complexes of the photosynthetic electron transport chain

From left to right the crystal structures of PSII, cyt b_6f , PSI and ATP synthase are shown (for simplicity only one monomer of each complex). After light absorption PSII oxidizes water to dioxygen and releases protons into the lumen. Abstracted electrons are transferred via plastoquinol to the cyt b_6f complex that pumps protons into the lumen and releases electrons via plastocyanin to PSI. After light absorption PSI reduces NADP^+ to NADPH at the ferredoxin site. The electrochemical H^+ gradient along the membrane is used by the ATP synthase to drive the production of ATP from ADP. Figure copyright B. Loll.

The supramolecular organization of the protein complexes in the thylakoid membranes of plants is divided into the stacked thylakoid grana regions, where predominantly PSII and the light harvesting complexes (LHCII) exist and the unstacked thylakoid lamellae regions, where PSI and ATP synthase predominate. It is assumed that this separation leads to efficient photosynthesis, because PSI can capture the excitation energy much faster than PSII. For maximum efficiency of photosynthesis, the absorbed light energy has to be balanced between PSI and PSII. One balancing mechanism, which involves the mobile light harvesting antenna, is via the state transition mechanism. State 1 is induced by the favored excitation of PSII and state 2 is induced by the favored excitation of PSI. A second proposed mechanism is the spillover mechanism, where excess excitation energy is transferred from PSII to PSI (16). Thus, a short distance arrangement would lead to uncontrolled energy flow from PSII to PSI (spillover). The stacking further provides PSII a way to fine-regulate the light energy requirement, because the excitation energy can flow within a thylakoid membrane and between two stacked membranes. Additionally a way to adapt to low-light conditions is provided, as it has been shown that in this case the amount of LHCII and stacked membranes increases (17). In cyanobacteria the situation is different, no such domain organization is known. The stacking of membranes is not possible predominantly because of the phycobilisomes that are attached onto PSII and PSI. A study on exoplasmic freeze-fracture particles of thylakoids from the cyanobacterium *Synechococcus* revealed the particle arrangement of PSIIcc within the membrane (Figure 1-5 A) (18). With this study the formation of cyanobacterial dPSIIcc *in vivo* was presented. It shows the organization into rows, which was proposed to be a unique feature of PSII in cyanobacteria and red algae, induced by either specific binding sites of the dPSII complexes or induced by the phycobilisomes. It was further discussed that the resulting energy conducting row system would allow for an efficient energy distribution along the thylakoid membrane over the connected dPSII complexes. Folea et al. reported, after mild solubilization of membranes from the organism *Synechocystis* 6803, arrays of several rows of dPSII complexes, most of the arrays comprised of two rows (17). Additionally they also found PSII double dimers. In order to see if the PSII double dimers have the same overall features as the single dimers, they fitted the dPSIIcc X-ray structure at 3.0 Å resolution of Loll et al. (19) in the EM 2D map of the PSII double dimer, which resulted in a good match (Figure 1-5 B).

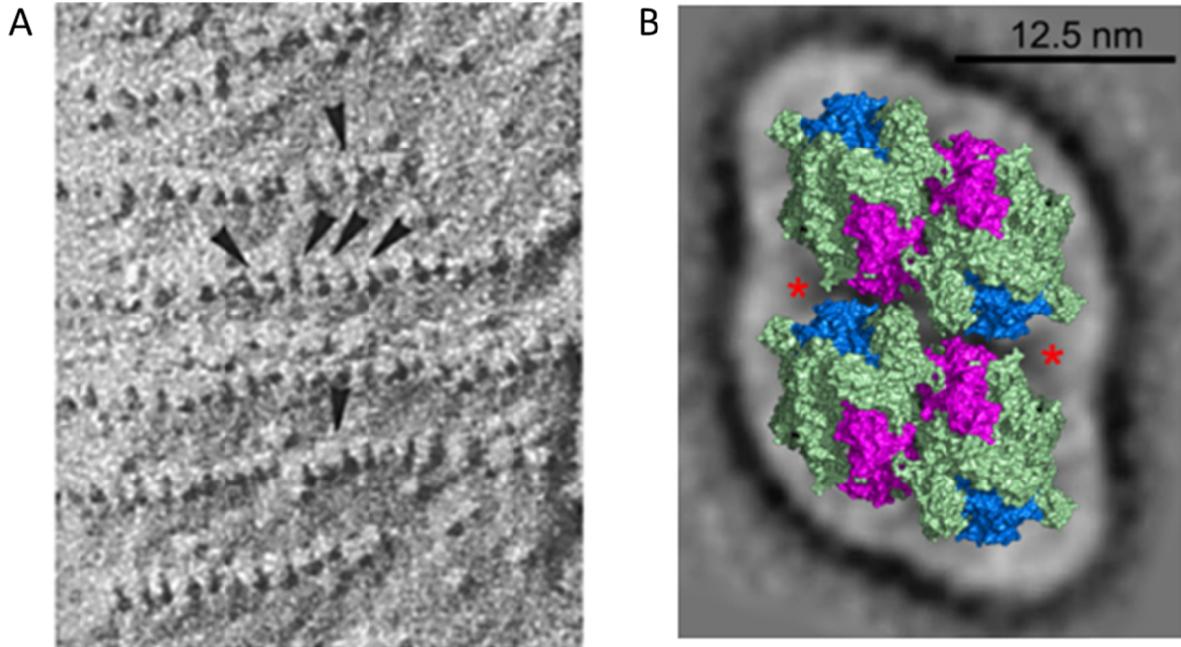


Figure 1-5 Cyanobacterial PSII arrangement in the thylakoid membrane and PSII double dimers

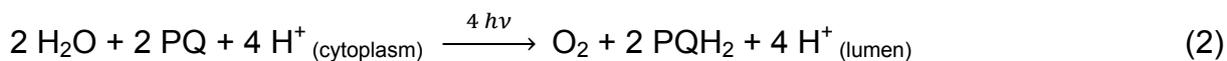
A) Freeze fracture through thylakoids of the cyanobacterium *Synechococcus spongarium*. Shown are exoplasmic fracture face (EF) particles (arrows) that correspond to dPSII complexes. The single EF particles have sizes of 10 nm x 20 nm and are attached by their longitudinal side to build rows of various lengths. They are divided into two identical parts of 10 nm x 10 nm corresponding to monomeric PSII. Figure taken from (18), with kind permission from Springer Science and Business Media. B) PSII double dimer EM map of *Synechocystis PCC6803* by Folea et al. (17) (grey background) with a fitted dPSIIcc X-ray structure of Loll et al. (19) (in green, blue, pink) seen from the luminal side. The red asterisks show where the EM map is larger than the X-ray structure and gives space for possible additional protein components. Figure taken from (17), with kind permission from Elsevier.

1.2.4 Photosynthetic reactions

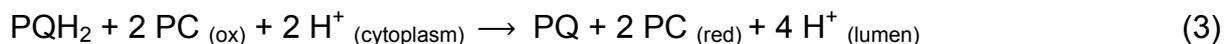
The overall basic equation of oxygenic photosynthesis (1) is frequently written as in (1a), because glucose (a six carbon sugar) is often an intermediate product of photosynthesis. The standard free energy for the synthesis of glucose is $\Delta H^\circ = +2870$ kJ/mol, available through light energy of the sun.



The electron transfer (ET) reactions that take place in a reaction chain along the thylakoid membrane proteins (Figure 1-4) occur rapidly, in a few picoseconds and are very specific. The process starts with the absorption of light at PSII, which is a water-plastoquinone-oxidoreductase, followed by charge separation in its RC. The following reactions can be divided into either happening at the acceptor side (cytoplasmic side) or at the donor side (lumenal side) of the protein complex. The primary electron acceptor in the RC oxidizes the manganese cluster (Mn-cluster) at the donor side, via a redox-active tyrosine. After four sequenced light excitations the Mn-cluster oxidizes two water molecules to form one molecule dioxygen and releases four protons into the lumen. Meanwhile the abstracted electrons finally doubly reduce the mobile electron carrier plastoquinone (PQ) at the acceptor side. Followed by double protonation the plastoquinol (PQH₂) leaves PSII into the membrane interior towards cyt b₆f (20), which reoxidizes PQH₂ to PQ and releases the protons into the lumen (2).

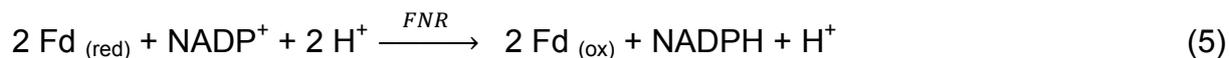


Via plastocyanin (PC), a soluble copper containing electron carrier in the lumen, the electrons are further transported to PSI (3). PSI is the next light-driven protein complex that functions as a plastocyanin-ferredoxin-oxidoreductase.

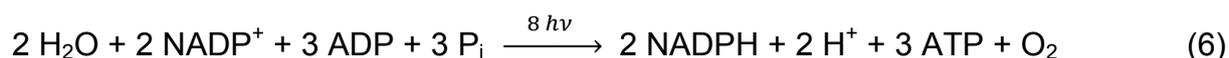


At PSI, after light absorption, the electron is transferred to a primary electron acceptor, the soluble electron carrier ferredoxin (Fd) at the cytoplasmic side (4). Fd leads the electron to the ferredoxin-NADP-oxidoreductase (FNR), where the reduction of NADP⁺ to NADPH is conducted (5).





This series of light driven ET reactions is called the light dependent reactions of photosynthesis. This reaction chain causes the change of the midpoint potentials of the participating proteins PSII, cyt b_6f and PSI. For illustration the linear ET chain is presented in a Z-scheme, which shows that after primary charge separation the ET is energetically downhill (Figure 1-6). The downhill flow of electrons provides the free energy for the creation of a proton gradient across the membrane in the linear electron transport. The proton motive force is used by the ATP synthase to produce ATP using ADP and P_i driven by protons (photophosphorylation). The reactions of the light dependent oxygenic photosynthesis can be summarized as in (6). Also a cyclic electron transport can occur under certain conditions. Then the electrons are transferred between cyt b_6f and PSI and a proton gradient is established across the thylakoid membrane to keep the production of the energetic molecules ATP operating. However, the oxidation of water and production of NADPH is not conducted.



In the light independent reactions or the Calvin-Benson cycle, the enzyme ribulose-1,5-bisphosphate carboxylase oxygenase uses NADPH and ATP to fix carbon dioxide to gain carbohydrates. The reduction of carbon dioxide includes a quantity of reactions in the cytoplasm summarized in (7).



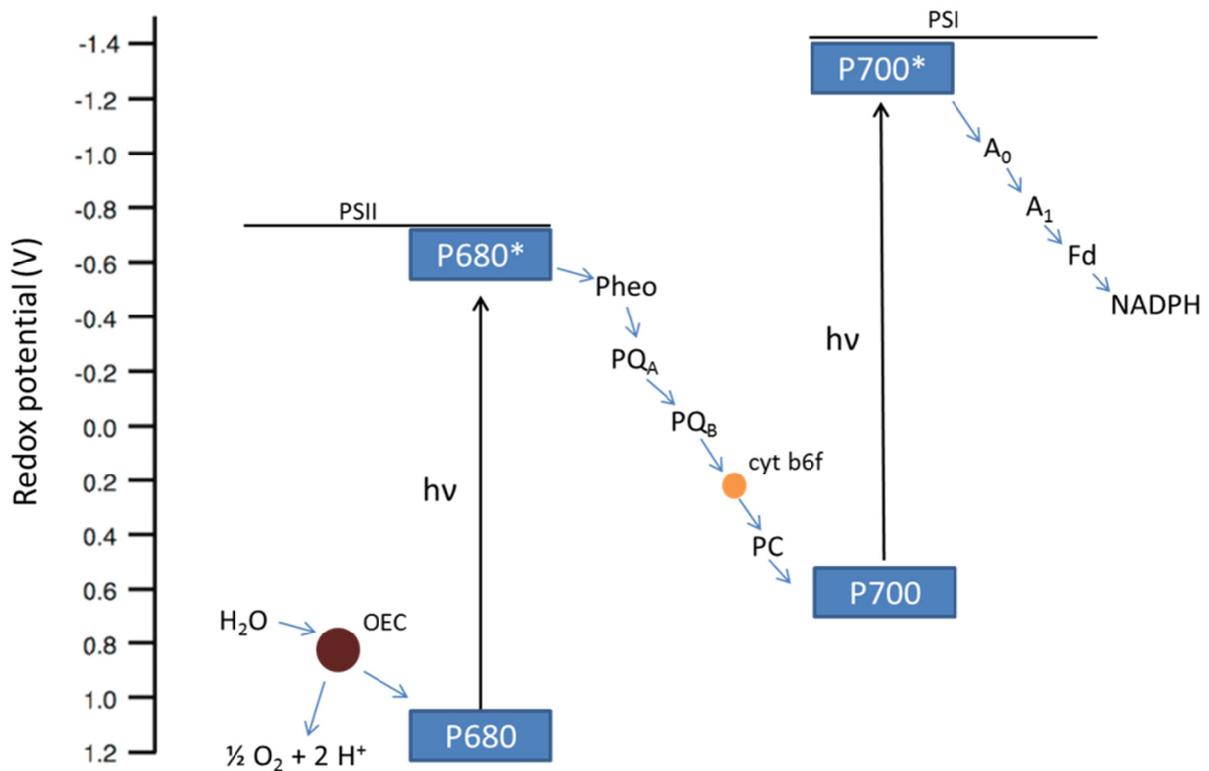


Figure 1-6 Z-Scheme of the oxygenic photosynthetic light reactions

The energy diagram of primary charge separation induced by light absorption ($h\nu$), and the linear electron transfer of oxygenic photosynthesis, with the involved proteins are presented in the Z-scheme. As indicated from left to right, the oxygen evolving complex (OEC), the primary electron donor of PSII (P680) ($E_m = +1.25$ eV) and the excited state (P680^{*}), pheophytin a (Pheo), the first electron acceptor (PQ_A) and the second electron acceptor (PQ_B), the cyt b₆f complex, plastocyanin (PC), the primary electron donor of PSI (P700) and the excited state (P700^{*}), a chlorophyll (A₀), a quinone (A₁), ferredoxin (Fd) and nicotinamide adenine dinucleotide phosphate (NADPH) are shown. After each charge separation step, the ET is energetically downhill.

1.3 Photosystem II

1.3.1 Elucidation of the PSII core complex structure

The method that gives most information on the overall structure of a protein complex and incorporated cofactors is X-ray diffraction (XRD) of protein crystals. For decades the structural elucidation of proteins had little success. Information on the PSII structure came from electron microscopy based techniques on 2D crystals or membrane fragments with low resolution, but allowed the construction of the overall

arrangement and subunit composition. Then a first crystal structure of the RC of a purple bacterium from *Rhodospseudomonas viridis* was published by Deisenhofer et al. in 1985 (21) and gave rise that this method can be applied to other membrane proteins. In 2001, the first dPSIIcc crystal structure from the cyanobacterial organism *T. elongatus* was published by Zouni et al. at 3.8 Å resolution (22). Constant improvement of the PSII crystals led to a 2.9 Å resolution crystal structure in the year 2009 (PDB codes 3BZ1, 3BZ2) (23). The monomeric PSIIcc (mPSIIcc) crystal structure was published in 2010 at a resolution of 3.6 Å (PDB code 3KZI) (24). In 2011, a group that is working with the cyanobacterial organism *T. vulcanus* published a crystal structure of dPSIIcc at 1.9 Å resolution (PDB code 3ARC) (25). This remains to date the best resolved structure of dPSIIcc and revealed the full composition of the catalytic center, the arrangement of the water oxidizing complex (WOC) and over 1000 water molecules within the protein complex. The structural information on plant PSII is still at an early stage. In 2010 a crystal structure of dPSIIcc from a higher plant, *Nicotiana tabacum*, with a resolution of 7 Å was obtained (26). In 2011 the first isolation of active mPSIIcc from the higher plant *Pisum sativum* (27) was achieved, but structural information are not yet available.

1.3.2 Overall structure

The structural description of PSIIcc presented now is based on cyanobacterial dPSIIcc from either the 2.9 Å crystal structure (23) or the 1.9 Å crystal structure (25). Both crystal structures exhibit the dPSIIcc to be a homodimeric, multisubunit protein-cofactor complex which is generally understood to be the fully functional form of PSII *in vivo*. The monomeric form of PSII is discussed to be an intermediate of the dimeric form during PSIIcc assembly and the repair cycle (28). Nevertheless a fully functional mPSIIcc crystal structure was obtained (24). The discussions about the two possible forms of PSII *in vivo* and their correlation are still ongoing (29-31).

The monomers of the homodimeric PSII are related by a C2 rotation axis perpendicular to the membrane plane. The hydrophobic intrinsic parts of the protein are embraced by the fatty acid chains of the thylakoid lipids, whereas the extrinsic hydrophilic parts are protruding in the hydrophilic surrounding of the lumen or the

cytoplasmic side of the lipid bilayer. PSII consists of four main intrinsic subunits (D1, D2, CP43, CP47) and cyt b559, which together build the RC core. They are surrounded by 13 small intrinsic subunits, consisting of either one or two transmembrane helices. The complex has additionally three membrane extrinsic subunits on the luminal side, which stabilize the WOC. One monomeric PSII complex harbors at least 70 cofactors. In the 2.9 Å resolution dPSII_{cc} crystal structure of *T.elongatus* (23) the following cofactor molecules have been revealed per monomer: 35 Chl_a molecules, 12 β-Car molecules, 2 Pheo_a, 2 heme (cyt b559 and cyt c550), three plastoquinone (PQ) molecules (Q_A, Q_B and Q_C), 25 integral lipids, seven n-Dodecyl-β-D-maltoside (βDM) molecules, a non-heme iron (Fe²⁺) with an associated bicarbonate ion, one calcium (Ca²⁺) and four manganese ions of the WOC, one chloride ion close to the WOC and two additional Ca²⁺-ions (Ca²⁺-PsbK and -PsbO). Associated to the whole protein complex is the special light harvesting antenna system, the phycobilisomes (Figure 1-2).

The RC core is built by the subunits D1 (PsbA) and D2 (PsbD) (the systematic names are given in parenthesis) which harbor the redox-active cofactors of the ET chain. The heterodimer D1/D2 is surrounded by the antenna proteins CP43 (PsbC) and CP47 (PsbB) and the α/β subunits of a cytochrome, the cyt b559. Together with the extrinsic subunits 33 kDa (PsbO), 12 kDa (PsbU) and cyt c550 (PsbV), it builds the minimal entity required to oxidize water. The architecture of D1 and D2 resembles the arrangement of subunits L and M in the purple bacterial reaction center (pbRC) (32) and the RC domains PsaA and PsaB of PSI (33).

The cofactors are arranged in a pseudo-C₂ symmetry related to the non-heme iron and form two vertical branches in D1 and D2. In detail present are four Chl_a molecules (P_{D1}, P_{D2}, Chl_{D1} and Chl_{D2} the latter two have formerly been named P680), two Pheo_a molecules (Pheo_{D1}, Pheo_{D2}) and two PQ molecules (Q_A, Q_B), in between the quinones lies the non-heme iron. The non-heme iron (for a recent review see (34)) is coordinated by a bicarbonate anion and conserved histidine residues of the proteins D1 and D2. The antenna proteins CP43 and CP47 harbor 13 and 16 Chl_a, respectively, which harvest light and funnel the excitation energy to the RC. Two Chl_a molecules, Chl_{ZD1} and Chl_{ZD2} are located at the RCs periphery. The catalytic heart of the protein complex is the WOC, which is a manganese cluster, containing four manganese ions and a calcium ion connected by μ-oxo bridges (Mn₄CaO₅) located in

the subunit D1 (Figure 1-12, page 29). Two redox active tyrosine molecules Y_Z and Y_D (in subunits D1 and D2, respectively) sit between the WOC and the redox-active chlorophylls of the RC.

1.3.3 The protein subunits

The crystal structure of cyanobacterial dPSII_{cc} by Guskov et al. at 2.9 Å resolution (23) revealed one monomer of the multisubunit complex to consist of at least 17 membrane intrinsic and three membrane extrinsic subunits (PsbO, PsbU and PsbV). The intrinsic protein subunits can be divided into the four large subunits CP47, CP43, D2, D1 with a molecular weight of more than 30 kDa and 13 low molecular weight (LMW) subunits PsbE, PsbF, PsbH, PsbI, PsbJ, PsbK, PsbL, PsbM, PsbT, PsbX, PsbY, PsbZ, Psb30 (ycf12) each with less than 15 kDa molecular mass (35) (Figure 1-7). All LMW subunits, except for PsbL, reveal post-translational modifications (23).

The two antenna proteins CP47, CP43 each possess six transmembrane α -helices (TMH) with additional extensive luminal loops. The RC proteins D1 and D2 possess five TMH, respectively. The four large subunits are closely related to the functioning of the electron transport chain as described before. The subunit D1 harbors most of the redox active cofactors (Figure 1-8) and is most sensitive to photodamage. At high light intensities Chl_a can form triplet states and when reacting with molecular oxygen may form singlet oxygen which further leads to oxidative damage of D1 and the incorporated cofactors (36). The excess light intensities can partly be balanced through excess energy dissipation, and the energy flow between the photosystems can be regulated by state transition, which means adjustment of the light harvesting outer antenna systems of PSII and PSI (37) as mentioned earlier. In a process called D1-turnover photodamaged, nonfunctional D1 is disassembled and replaced with newly synthesized intact D1 every 30 minutes (38-40). *T. elongatus* can express three different isoforms of subunit D1, namely PsbA1, PsbA2 and PsbA3. Under normal growth conditions PsbA1 is the dominant form and the here presented crystallized dPSII_{cc} exclusively contains this form. In response to high light conditions PsbA3 can replace PsbA1 (41). The two isoforms differ in 21 amino acid positions, most of them in the vicinity of redox active cofactors. A regulative

mechanism to adapt to changing environmental conditions through different gene expression is assumed (42).

Each LMW subunit has only one TMH, except for subunit PsbZ which has two TMHs. The final function of most of the LMW subunits is still unclear and remains a matter of debate. Subunit PsbI is tightly connected with the RC complex and is believed to have influence on the PSII dimer formation during PSII assembly. Nevertheless, once the dimer is formed, PsbI is no longer required for the dimer stability (43). PsbL, PsbM and PsbT form a three helix bunch located at the monomer-monomer interface of dPSII. Thus, these subunits have been suggested to be essential for PSII dimer formation and stability. Direct protein contacts are only formed between the opposed PsbM subunits. Their TMHs interact in a heptad motif as in a membrane-spanning leucine zipper (23). Surprisingly, the deletion of PsbM in a mutant of *Synechocystis* sp. PCC 6803, a mesophilic cyanobacterium, did not affect dimer formation, only the additional deletion of PsbT prevented dimerization (44). The direct role of subunit PsbY is still unclear. Its location close to cyt b559 was revealed by mutational studies (45) and corresponds to helix X2 in the 3.0 Å structure of *T. elongatus* (19) and an unassigned helix in *T. vulcanus* at 3.7 Å resolution (46). In the 2.9 Å resolution crystal structure of dPSIIcc (23) PsbY was present with poor electron density. In the 1.9 Å resolution crystal structure of dPSIIcc (25) and in the 3.6 Å resolution structure of mPSIIcc (24) the subunit was absent. These facts suggested a loose association with the complex and possible loss during purification steps. Surprisingly the 2.1 Å resolution structure of Sr-substituted dPSIIcc from *T. vulcanus* revealed PsbY only present in one of the monomers of the dPSIIcc (47). For a review on the LMW protein subunits of PSII see (48).

Three extrinsic subunits PsbO, PsbU and PsbV can be found at the luminal side of the PSII complex (Figure 1-7 B). PsbO, also called 33 kDa protein or manganese stabilizing protein, is the only β -barrel structure of PSII. It features a Ca^{2+} -binding site (49), which is believed to have an auxiliary role in H^+ ejection from the proton channel leading from the WOC to the lumen (23). It is essential for maintaining oxygen evolution activity as PsbO-lacking mutants from green algae and higher plants completely lost activity and in cyanobacteria the activity was markedly reduced (50, 51). The subunit PsbU likewise PsbO is of importance for oxygen evolution (52). Further the deficiency of PsbU leads to an increasing detachment of phycobilisomes

to the cytoplasmic side (53). The subunit PsbV (or cyt c550) is a heme-binding protein; the iron of the heme is ligated by two histidine residues of this subunit. It was suggested that PsbV has the same stabilizing and protecting effect on the manganese cluster as the other extrinsic proteins. The midpoint redox potential of PSII-bound cyt c550 has recently been corrected to a value of $E_m = + 200$ mV (54). The new value opens the possibility of a redox function of cyt c550, by serving in electron donation to the manganese cluster in a photoprotective cycle (55). Other extrinsic proteins found in cyanobacteria are either lost during purification or bind in intermediate states of PSII assembly, for example PsbQ, PsbP and Psb27 (28, 56). For a review on the extrinsic proteins see (57).

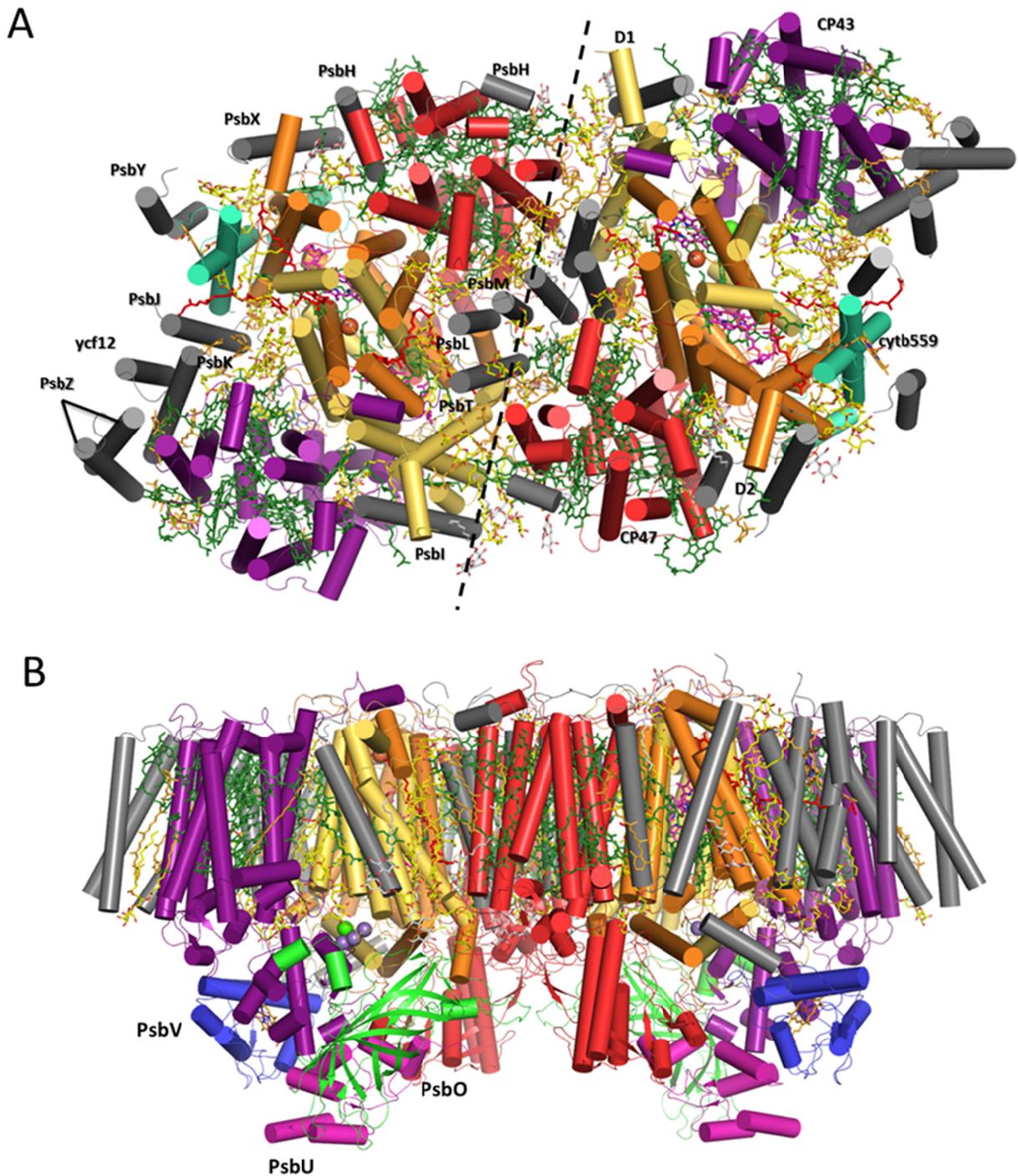


Figure 1-7 The protein subunit composition of dPSIIcc

The homodimeric PSIIcc at 2.9 Å resolution (PDB 3BZ1/3BZ2) A) Overview of the intrinsic PSII subunits from the cytoplasmic side in cylinder mode and cofactors in stick mode. Monomer-monomer interface indicated by dashed line. Monomer on the right side shows the eleven small TMHs (grey) labelled. Monomer on the right side shows the subunits D1 (yellow), D2 (orange), CP43 (purple), CP47 (red), cyt b559 (cyan) labelled. Lipids and detergent molecules (yellow), Chl_a (green), Car (orange), heme (orange), Pheo (pink), PQ (red), Mn₄Ca-cluster (grey/green spheres, only partly visible), non heme iron (orange sphere). B) View of the dPSIIcc along the membrane plane with cytoplasm above and lumen below. The intrinsic protein subunits with same color code as in A and the three membrane-extrinsic subunits labelled PsbO (green), PsbU (pink) and PsbV (blue).

1.3.4 Overall function

The key reaction conducted by dPSIIcc during oxygenic photosynthesis is given in equation (8).



This key reaction includes a sequence of light induced charge separation states with plastoquinol formation (9) (58).



About 100 water molecules per second are oxidized under full sunlight in PSII of plants and cyanobacteria (2). A complex network of reactions combines excitation energy transfer (EET) and ET carried out by the redox-active cofactors in the RC subunits of PSII. In EET excitation energy is transported to the next pigment, in ET electrons are passed over with modification of the pigments redox states. The charge separation and ET is further coupled with proton transfer. PSII acts as a water-plastoquinone-oxidoreductase and combines the two-step, one-electron reaction sequences on the acceptor side (plastoquinone site) with the 4-electron chemistry on the donor side (water oxidizing site). According to the ET, the PSII complex is divided into acceptor (electron uptake by plastoquinone) and donor side (electron donation by the water oxidizing complex).

The reactions can be summarized as follows: Oxygenic photosynthesis starts with light absorption by chlorophylls of the RC. An electron from a special chlorophyll is transmitted to Pheoa and via a bound PQ at the Q_A site further to the mobile electron carrier Q_B . The generated radical cation chlorophyll molecule abstracts an electron, via the redox active tyrosine Y_Z , from the WOC. During water oxidation the WOC is running through a five step catalytic cycle named S-cycle by stepwise abstraction of

electrons, each oxidation state of the Mn-cluster is denoted with S_i , with intermediate states $i=0-4$, (for more information on the S-states, see 1.3.8 The water oxidation site, page 29). The WOC is promoted from the dark adapted state S_1 to the S_2 state. The next light absorption step transfers a second electron to the Q_B in the same manner as in the first step. The abstraction of another electron from the WOC is accompanied with a promotion to the state S_3 . The doubly reduced Q_B is then doubly protonated and forms a plastoquinol (PQH_2) that leaves the Q_B site into the PQ pool of the thylakoid membrane to reach the next protein complex (cyt b_6f) of the ET chain (Figure 1-4, page 6). A new PQ molecule from the PQ pool refills the Q_B site. The next light absorption step induces a third ET to the second PQ at the Q_B site together with the third abstraction of an electron from the WOC and the proceeding of it to state S_4 . It is assumed that molecular oxygen is then built spontaneous in the reaction step to state S_0 without light absorption. The fourth light absorption step releases the second PQH_2 and the WOC is brought back to the dark stable S_1 state. Thus, one cycle splits two water molecules releases molecular oxygen and four protons into the lumen (Figure 1-13, page 30).

Details on charge separation and the roles of the involved pigment molecules (Figure 1-8) are given in the following sections. For a recent review on charge separation see (59).

1.3.5 Cofactors

Chlorophyll a

In the 2.9 Å resolution structure of dPSII_{cc} (23) 35 Chl_a molecules could be completely modelled for the first time. Of these, 16 Chl_a molecules are bound to CP47 (PsbB) and 13 Chl_a molecules are bound to CP43 (PsbC). They serve as light harvesting pigments and transfer the excitation energy to the RC, as mentioned before. The remaining six Chl_a molecules can be separated into the RC chlorophyll molecules (P_{D1} , P_{D2} , Chl_{D1} , Chl_{D2}) and the peripheral RC chlorophylls (Chl_{zD1} and Chl_{zD2}) (Figure 1-8). The RC chlorophylls conduct the charge separation steps and the ET along with modification of their redox states. Besides this, the Chl_a molecules contribute to the stabilization of the protein complex (60).

The excitation energy transfer (EET) from the antenna Chls within the PSIIcc to the RC takes about 40-50 ps (61, 62). This process is rather slow when compared to the EET from the outer antennae to the PSIIcc, which is faster with less than 10 ps, and seems to be the rate-limiting step of energy trapping (63, 64). The reason for this is ascribed to the relatively large distances between antenna Chls and the RC in PSIIcc (62, 65). When the excitation energy reaches a special chlorophyll molecule of the RC, the energy is not passed on to the next neighboring pigment molecule, but an electron is transferred instead and the first charge separation takes place. The most recent model sees the Chl_{D1} as the longest wavelength pigment, forming the excited state P^* , and as the first electron donor of the ET. It is assumed that charge separation starts from Chl_{D1} by the transfer of an electron to Pheo_{D1} in the range of 0.6-3.0 ps (Figure 1-8). Within 6-11 ps, a second radical pair $P^{++}_{D1} \text{Pheo}^-_{D1}$ is formed. The P^{++}_{D1} has the strong oxidizing power (1.25 eV) (66) that allows for water oxidation. Via the redox-active tyrosine Y_Z it is capable of extracting electrons from the WOC (see chapter 1.3.7, page 28 and chapter 1.3.8, page 29 for further details). In the third step the formation of $P^{++}_{D1} Q_A^-$ at the acceptor side of the PSII complex stabilizes the charge separation within 300 ps. For a review on charge separation see (59).

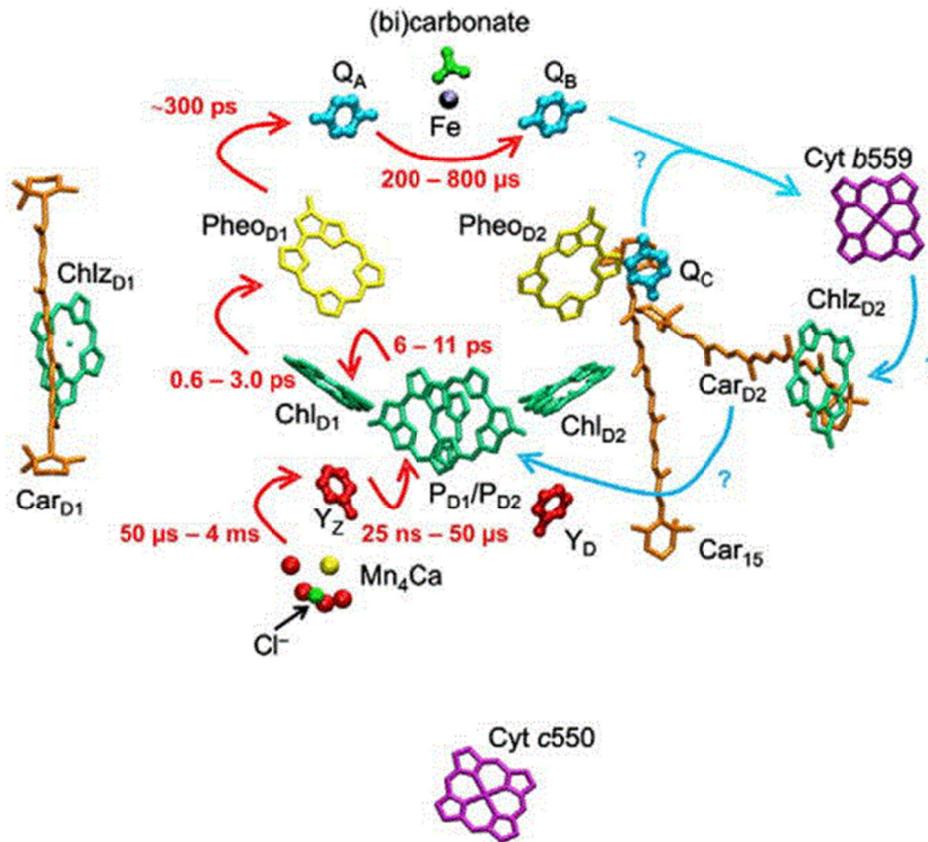


Figure 1-8 Arrangement of the redox-active cofactors of the PSII reaction center

Redox-active cofactors as labelled, red arrows indicate the electron transfer steps with times. Blue arrows indicate possible second side-path electron transfer processes, which are still unidentified (see question marks), possible reaction ways and involved cofactors are cyt b559, Chl_{D2}, Car_{D2}, Car₁₅, Q_C and P_{D2}. Figure according to the 2.9 Å resolution dPSII_{cc} crystal structure adapted from (64) with kind permission from Elsevier.

β-Carotene

The mPSII_{cc} crystal structure of *T. elongatus* (24) as well as the dPSII_{cc} from *T. vulcanus* (25) both revealed 11 β-carotenes (Car) per monomer. In the dPSII_{cc} of *T. elongatus* (23) one additional Car (Car₁₅ on the D2 side) was found summing up to 12 Car molecules per monomer. The obtained variations are probably due to differences in sample preparation. Car molecules play a role in light harvesting and in the protection against photooxidative damage of PSII. They stabilize the pigment-protein complex and fulfil quenching of excited state Chls and reactive oxygen species (67, 68). Eight Car molecules are located in the antenna proteins CP43 and CP47, arranged in close distance to Chl_a molecules, which is of importance for the ³Chl_a quenching. Two Car molecules (Car_{D1} and Car_{D2}) and the additional Car₁₅ are

part of the RC unit (Figure 1-8). Car_{D2} is orientated horizontally to the membrane plane, Car_{D1} and Car₁₅ almost perpendicular to it. Car_{D2} and Car₁₅ are believed to play a role in possible side path ET reactions with Q_C, cyt b559, Chl_{D2} and Chl_{D2}, while Car_{D1} is located too far away from the redox active cofactors to have an effect on them. It lies closely to Chl_{D1} within a 4.1 Å edge-to-edge distance of their π -systems, which implies a possible role in triplet quenching of ³Chl_{D1}. Five Car molecules are located next to the monomer-monomer interface which give the assumption for a structural involvement in dimerization of PSII (63, 69, 70). To evaluate the influence of β -Car molecules (Car_{D1}, Car_{D2} and Car₁₅) on the secondary ET reactions, initial measurements of dPSIIcc using polarization dependent Raman measurements were performed by Brose et al. (71). A satisfying answer to this issue is believed to come from similar measurements of mPSIIcc crystals, as simulations showed that upon excitation relatively strong signal changes occur for the three β -Car molecules, in contrast to those obtained from dPSIIcc crystals.

Plastoquinone

At the acceptor side of PSII, plastoquinones act as electron transmitter and electron carrier molecules. A plastoquinone (PQ) located at the Q_A site (embedded in subunit D1) is the fixed primary electron transmitter. A second PQ at the Q_B site (embedded in subunit D2) is the mobile, two-electron carrier molecule that delivers the electrons in the reduced form as PQH₂ to the thylakoid interior towards cyt b₆f. PQH₂ is replaced by a fresh PQ that comes from the PQ-pool situated in the thylakoid membrane. The two PQs, Q_A and Q_B, have been revealed in both crystal structures of dPSIIcc (23, 25). The crystal structure of *T. elongatus* (23) revealed an additional third mobile PQ molecule named Q_C, ca 14 Å away from Q_B (Figure 1-8) in subunit D2 next to cyt b559. The absence of Q_C in the other PSII structures suggests a low affinity to its binding site and/or that the presence is very much dependent on the sample preparation. All three PQs are PQ-9 molecules with a 2,3-dimethyl-1,4-bezoquinone head group and a hydrophobic tail of nine isoprenoid units. The Q_A molecule is fixed via its head group with two hydrogen bonds to its keto-oxygens (one to a His residue and one to a Phe residue) and a π -stacking interaction to a Trp residue. The isoprenoid residue of Q_A is bound by van der Waals interactions to the mainly unpolar protein environment. In contrast to that, Q_B is a substrate and only

temporarily bound to the Q_B site, which can lead to an incomplete occupancy in the PSII crystal structures. Q_B builds hydrogen bonds to a His and a Phe residue. In contrast to Q_A , the Q_B molecule is surrounded by several protonatable groups. The binding of Q_C to the protein is not revealed. It is stated that for all three quinones dispersion forces contribute to the stabilization rather than electrostatic interactions (72). For the proton-coupled ET steps between the PQs, two turnovers are necessary to release PQH_2 into the membrane. The first ET step creates a semiplastoquinone anion radical $Q_B^{\cdot-}$ which is stabilized by nearby protonated amino acids residues. The second ET to $Q_B^{\cdot-}$ is combined with the first protonation of the semiplastoquinone. Three different models are suggested for the steps with the final state $Q_AQ_BH_2$. The most likely sequence is the pathway where proton transfer is followed by ET via $Q_A^{\cdot-}Q_BH$. For further details and illustration of all three pathways see (64, 73, 74).

1.3.6 Integral lipids

The dPSIIcc has the largest number of integral lipids among all other photosynthetic proteins (75). The crystal structure of dPSIIcc at 2.9 Å resolution (23) revealed the so far highest number of 25 integral lipids per monomer (Figure 1-9 and Figure 1-10). In the 1.9 Å resolution dPSIIcc structure (25) 20 integral lipids (+3 lipids with unknown identity) per monomer and additionally 15 single alkyl chains with unknown molecular identity have been detected. Some of these may belong to further lipids. The deviation in lipid content in the two crystal structures are supposed to result from different growth conditions, purification protocols and a varied detergent application (Figure 1-11). Four types of integral lipids MGDG, DGDG, SQDG and PG are incorporated into PSII (Figure 1-10). In the same manner as the thylakoid membrane lipids, integral lipids of PSII face with their headgroups towards the membrane surface, their hydrophobic tails interfuse the protein complex. Of the 25 lipids per monomer, three are located at the periphery of the protein complex, seven lipids (and 4 detergent molecules β DM) are situated at the monomer-monomer interface, 15 lipids (and one β DM) can be found between protein subunits. The latter are always grouped in clusters of 2-3 lipids, the biggest cluster consists of 8 lipids, and together they surround the RC proteins. In detail 11 MGDG, 7 DGDG, 5 SQDG and 2 PG molecules per monomer were assigned in the 2.9 Å resolution structure (23). In the

1.9 Å resolution structure (25) 6 MGDG, 5 DGDG, 4 SQDG and 5 PG molecules have been assigned. The headgroups of uncharged DGDG are exclusively located at the luminal side, negatively charged headgroups of PG and SQDG only on the cytoplasmic side and those of MGDG can be found on both sides of the protein complex. The fatty acid chains could only be modeled partial (~ 10-12 C-atoms) in the crystal structures due to their high flexibility and/or insufficient resolution so far. For both organisms, *T. vulcanus* and *T. elongatus*, the fatty acids of thylakoid membrane lipids and integral lipids of PSIIcc are 16:0, 16:1, 18:0 and 18:1 (76). The nature of the lipid headgroup determines the number of hydrogen bonds and polar interactions between amino acids and the lipids. Smaller headgroups of MGDG form 4.5 interactions, PG forms 4.3, SQDG forms 6.5 and the larger DGDG forms 8.5 interactions in average. The weakest interaction is found for the detergent molecules β DM with only 3.3 polar protein interactions, which supports the anticipated weaker binding compared to the natively incorporated lipid molecules. The differences in binding pocket architecture of each specific lipid show no indication for chemical heterogeneity of lipid headgroups to their binding sites.

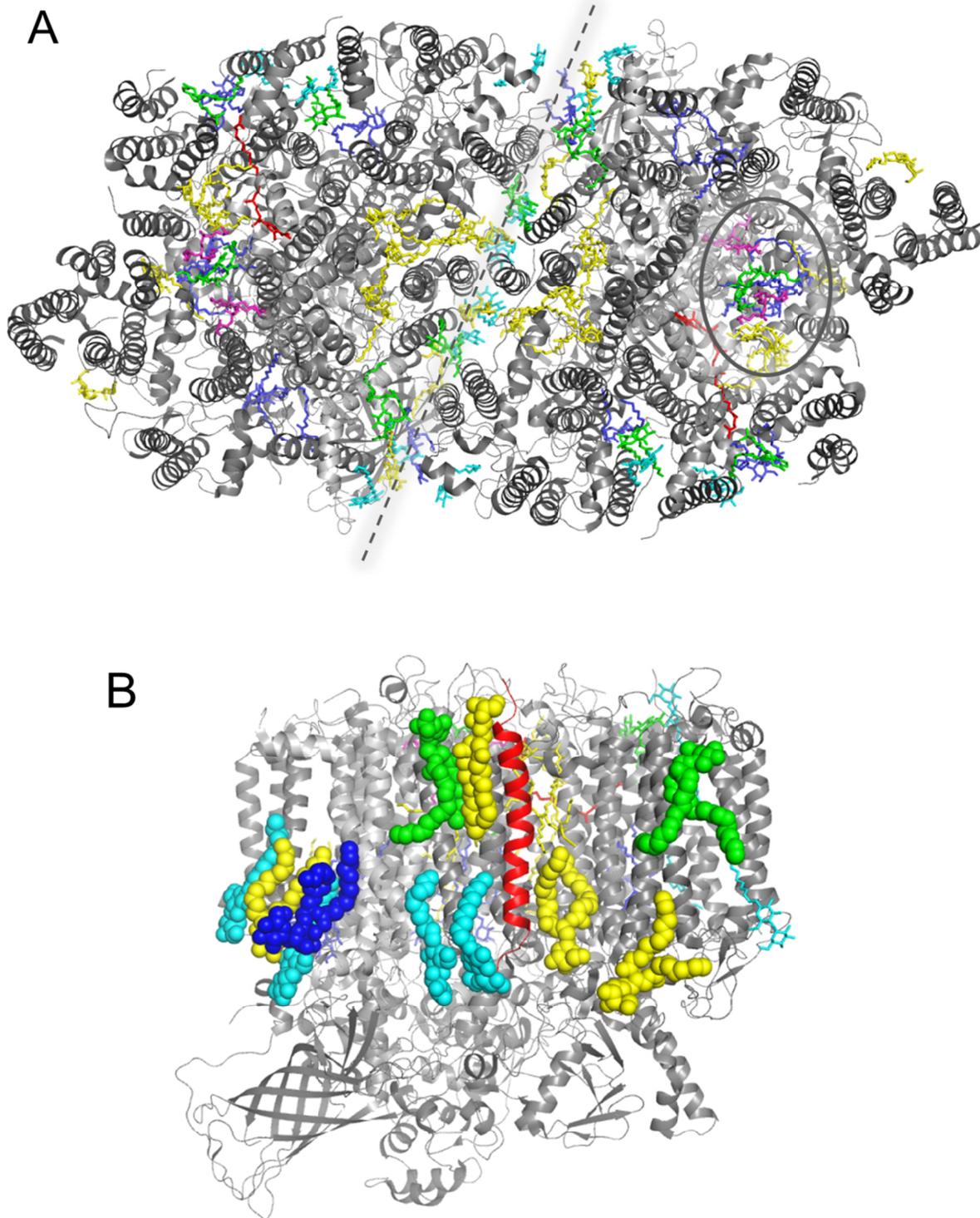


Figure 1-9 Integral lipids of dPSIIcc at 2.9 Å resolution

Lipids in the dPSIIcc according to the 2.9 Å resolution structure (PDB 3BZ1/3BZ2) A) View from the cytoplasmic side onto the dPSIIcc. Protein subunits are shown in cartoon mode in grey, lipids and additional detergent molecules in stick mode, MGDG (yellow), DGDG (dark blue), PG (pink), SQDG (green) and detergent β DM (cyan). Most lipids are arranged around subunits D1/D2 and CP43/CP47 or along the monomer-monomer interface. A lipid bilayer cluster close to Q_B (red) is encircled. B) view along the membrane plane onto the monomer-monomer interface of PSII with same colour code as in A, but lipids and detergent molecules are shown as spheres and subunit PsbM highlighted in red.

Introduction

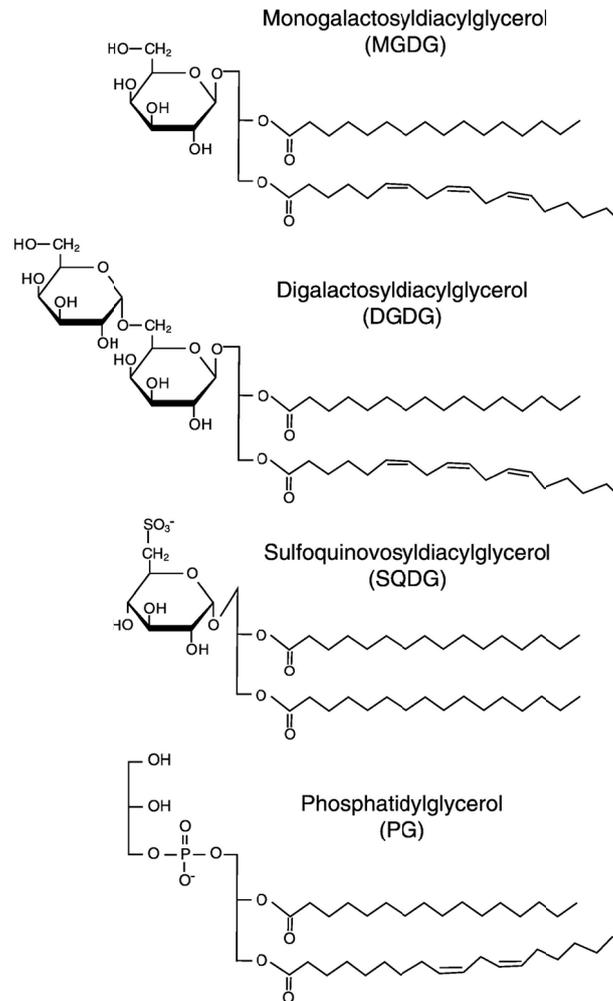


Figure 1-10 Structure of integral lipids of PSII

Chemical structures of the four integral lipids digalactosyldiacylglycerol (DGDG), monogalactosyldiacylglycerol (MGDG), phosphatidylglycerol (PG) and sulfoquinovosyl (SQDG). The most common forms of fatty acids for *T. vulcanus* and *T. elongatus* are 16:0, 16:1, 18:0 and 18:1 (76). Here the typical fatty acids bound to each class of lipid in *Synechocystis* sp. PCC 6803 are shown as example. Figure taken from (77), with kind permission from Elsevier.

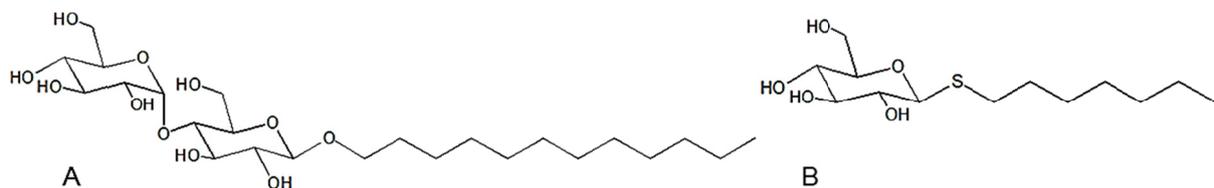


Figure 1-11 Detergent molecules found in dPSIIcc structures

Chemical structures of A) *n*-Dodecyl-β-D-maltoside (βDM) and B) *n*-Heptyl-β-D-thioglucoside (HTG), both detergents have been used for purification and/or crystallization of dPSIIcc. For obtaining the 2.9 Å resolution crystals structure (23) the detergent βDM was used, for the 1.9 Å resolution crystal structure (25) both detergents were used.

Due to the structural similarity of the headgroups of DGDG (a digalactoside) and β DM (a maltoside) (Figure 1-10 DGDG and Figure 1-11 A) it is assumed that β DM which is bound to PSII has substituted DGDG in the native, non-solubilized PSII complex (78). Since the lipid headgroups form a lot of inter-subunit contacts (hydrogen bonds and salt bridges) with two to three different protein subunits, they play an important role in providing stability and at the same time offer a certain flexibility that is needed for assembly and disassembly for example during the D1-turnover. Lipids are further believed to play a role in dimer formation, as a total of 14 lipids (7 from each monomer) namely 2 DGDG, 8 MGDG, 4 SQDG, (and additional 8 β DM molecules) fill the monomer-monomer interface in the 2.9 Å resolution dPSIIcc structure (23). In the 1.9 Å resolution dPSIIcc crystal structure (25) 12 lipids (2 SQDG, 1 MGDG, 3 PG, per monomer) and additional 4 β DM and 6 n-Heptyl- β -D-thiogluconide (HTG) detergent molecules (Figure 1-11 B) have been found to occupy the monomer-monomer interface. In this structure 3 PG molecules have been found behind subunits PsbL and PsbT of the monomer-monomer interface, which are believed to stabilize the PSII dimer. This finding is supported by studies on depletion of PG, which resulted in a destabilization of the dPSIIcc (79, 80). However, SQDG molecules are found at the direct interface in both dPSIIcc structures, but are lacking partly in the mPSIIcc (24) and are therefore discussed to be important for dimer formation. Negatively charged lipids (SQDG, PG) can also be found ligating Mg^{2+} of Chl molecules, which can influence the electronic distribution within the π -systems of the Chls or the energies of their excited electronic states, thereby changing their spectral and redox properties (78). Second, the ligation by lipids allows for the incorporation of Chls into regions where no other ligation is possible, thus giving lipids a chaperone-like role.

As the quinone binding site Q_B is buried in the D1/D2 subunits and not directly located at the surface of the PSIIcc, the large bilayer cluster of 8 lipids close to the Q_B site provides a hydrophobic environment for quinone diffusion. Further is possible that they have impact on the redox potential of the quinones, because the Q_A site is dominated by uncharged lipids (MGDG, DGDG) and the Q_B site is dominated by charged lipids (SQDG, PG) which could influence the electron transfer from Q_A to Q_B via the lipid environment. It has further been revealed that lipids contribute to the removal of oxygen from the protein complex. Results from Xe derivatization showed that lipids, due to their hydrophobic character, can serve as a pathway channels for

oxygen from the luminal side to the cytoplasmic side of the dPSIIcc (81). Oxygen concentration profile measurements of lipid bilayers using spin labels revealed oxygen accumulation within the hydrophobic fatty acid tails of lipids which supports the above assumption (82). For recent reviews on lipids in PSII see (77, 78, 83).

1.3.7 Structure of the Water oxidizing complex

To understand the functional details and unravel the overall process of water splitting it is further essential to elucidate the structure of the WOC. Methods including electron paramagnetic resonance (EPR), electron nuclear double resonance (ENDOR), fourier transform infrared (FTIR) and X-ray absorption (XAS) spectroscopy and XRD of PSIIcc crystals using synchrotron radiation (SR) have been used to reveal the composition and arrangement. XRD of PSIIcc from *T. vulcanus* at an improved crystal structure resolution of 1.9 Å (25) revealed the first reliable structure of the OEC and the WOC in its dark state S_1 . Note that Grundmeier et al. calculated the S state of the 1.9 Å resolution structure of dPSIIcc and suggest it to be denoted as S_{-3} , which means a reduction by four electrons of the prevalent S_1 state (84). At this high resolution it was possible for the first time to assign four manganese, one calcium and five μ -oxo-bridging oxygen atoms linking the metal atoms, resulting in a Mn_4O_5Ca -cluster. The exact geometry of the cluster, which was unclear before, can now be described as a cubane, with one manganese (labeled Mn4) being located outside this arrangement resulting in a “distorted chair” (Figure 1-12 A). The bond lengths of the manganese to oxygen atoms vary between 1.8-2.6 Å and those of the calcium to oxygen atoms vary between 2.4-2.7 Å. This difference results in an asymmetric arrangement of the cubane. Additionally four water molecules associated with the cluster were identified. Two water molecules are bound to Mn4 with a distance of 2.1 and 2.2 Å. The two other water molecules are bound to the one calcium atom with distances of 2.4 Å. No other water molecules were identified in the vicinity of the cluster, which implies a possible role for one or more of these as substrate water molecule(s). The first ligand sphere of the WOC (Figure 1-12 B) consists of the surrounding amino acids of subunit D1 and CP43. The manganese and calcium atoms are coordinated by six and five amino acids, respectively. D1-Glu 189 serves as a monodentate ligand to Mn1, all the other ligands, D1-Asp 170 to

Mn4 and Ca, D1-Glu 333 to Mn3 and Mn4, D1-Asp 342 to Mn1 and Mn2, D1-Ala 344 to Mn2 and Ca, and CP43-Glu 354 to Mn2 and Mn3, serve as bidentate ligands. All of them are in distances between 1.9-2.4 Å and are believed to have a high importance for the water splitting mechanism and the O-O bond formation. In the second ligation sphere, three amino acids (D1-His 337, D1-Asp 61, D1-Arg357) are highlighted to be of importance for the structure of the WOC (25). For recent reviews see (85, 86).

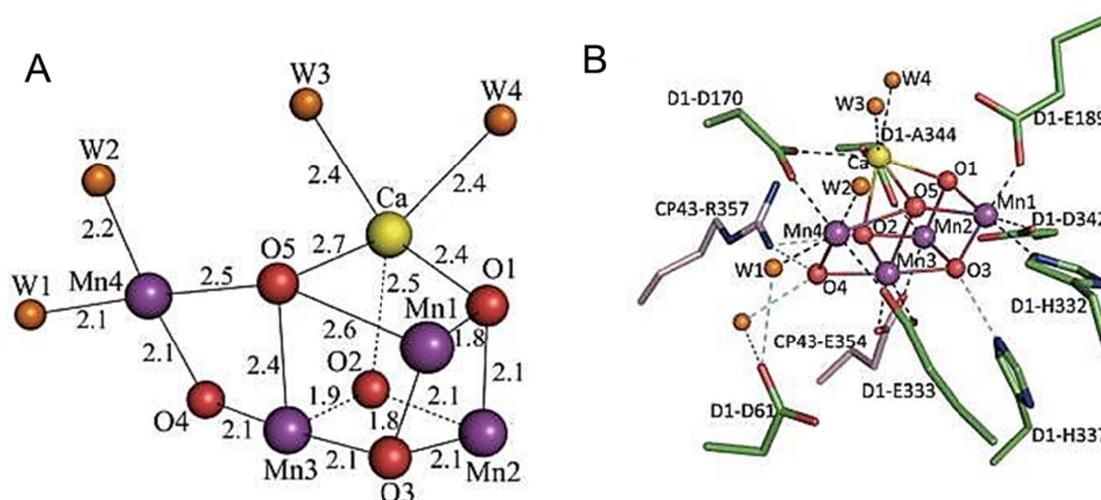


Figure 1-12 WOC and OEC as derived from 1.9 Å resolution crystal structure of dPSIIcc

A) Mn_4O_5Ca -Cluster with ligated water molecules (W) and distances given in Å B) Ligation sphere of amino acids to the Mn_4O_5Ca -Cluster and the water molecules (W). Taken from (25), reprinted by permission from Macmillan Publishers Ltd: *Nature*, (25), copyright 2011.

1.3.8 The water oxidation site

At the donor side of the PSIIcc, which is situated at the luminal side of the protein complex in subunit D1 (PsbA), the oxidative water splitting takes place. A manganese cluster, in particular the inorganic Mn_4CaO_5 -cluster (25, 85), is the catalytic RC that forms the oxygen evolving complex (OEC) together with surrounding coordinating amino acids, as mentioned before. Already in 1969, first studies on flash-induced oxygen evolution yield on dark adapted PSII samples have shown a maximum in oxygen evolution after every fourth flash and the first maximum after the third flash (87) (Figure 1-13 A). Based on these studies, Kok and coworkers proposed a cycle for the stepwise oxidation of water (88) which is valid until today. This model has

been named Kok-cycle, or more frequently it is called S-cycle of water oxidation (Figure 1-13 B). Each S-state represents one oxidation state of the Mn_4CaO_5 -cluster, which is cycling through a five-step catalytic cycle, with the intermediate states S_i ($i=0-4$), starting and restarting at the dark stable S_1 state.

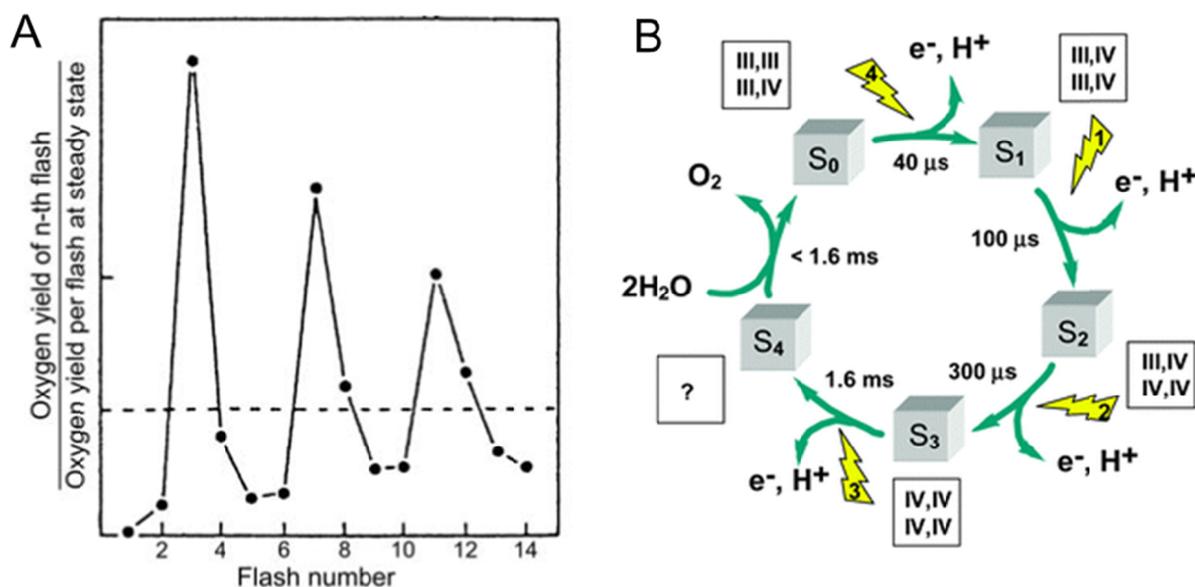


Figure 1-13 S-Cycle of water oxidation

A) Typical four period oscillation pattern of the oxygen yield as induced by single turnover flashes on dark-adapted PSII from spinach thylakoids. Figure adapted from (61), with kind permission from Springer Science and Business Media. B) Based on the original S-cycle the basic knowledge about the single S steps is illustrated. The cycle starts at the dark stable state S_1 . With every flash the Mn oxidation states change (see small boxes; for S_4 the oxidation states are unknown) and one e^- and one H^+ are released. After the S_4 state oxygen is produced and released. Time constants for the proceeding of the reactions are labeled inside the cycle. Figure adapted from (89).

Many studies support the direct coupling of the oxidation and ET processes with the proton-transfer reactions (90, 91). Starting from S_1 , each light absorption step leads to a proton and an electron release and a proceeding of the WOC to the next oxidation state. After the third flash and the release of a proton and an electron, molecular oxygen is spontaneously and light-independently formed during the S_4 to S_0 transition. The release of oxygen resets the WOC to its lowest, dark stable oxidation state S_1 (61, 92). The S_0 to S_3 states are stable over a timescale of seconds, whereas the S_4 state is highly reactive and has not been characterized experimentally in a conclusive way (93-96). Even so, it is almost certainly agreed that

the O-O bond formation takes place at the S_4 oxidation state after a sequence of events, including deprotonation, O-O bond formation, oxygen evolution, rearrangement of the WOC and substrate water binding (97-99). Several models for the O-O bond formation have been proposed and are summarized in the recent review (84). Unravelling the O-O bond formation requires the identification of the two substrate sites and the elucidation of the chemical mechanism via which the substrates couple together (100). Rapatzkiy et al. performed EPR studies to find water substrate binding sites of the Mn_4O_5Ca -cluster via measurement of ^{17}O -hyperfine couplings (99) and concluded two possible chemical mechanisms for O-O bond formation: (I) mechanisms involving a nucleophilic attack between substrate oxygen atoms and (II) oxo/oxyl radical coupling of two Mn oxygen ligands (Figure 1-14). In the nucleophilic attack mechanisms, the two substrates (W2 and W3) are either water/hydroxyl bound to Ca^{2+} (W3) and the second substrate (W2) building a Mn^{IV} -oxyl or Mn^V -oxo species at MnA4 (Figure 1-14, Ia), or the two substrates are terminal water/hydroxyl ligands to MnA4, probably W1 and W2 (Figure 1-14, Ib). The proposed radical coupling mechanism (Figure 1-14, II) considers the O5 μ -oxo bridge between MnA4 and MnB3 to be one substrate and the second substrate to bind to the open coordination site of the Mn_4CaO_5 -cluster to MnD1. The latter substrate binds as water/hydroxy in the S_2/S_3 state and forms an oxyl radical in the S_4 state (99). An essential step to understand the water oxidation mechanism is to capture the S_4 state intermediates by following the transition $S_3 \rightarrow (S_4) \rightarrow S_0$ in a time resolved manner (see Chapter 4, page 95).

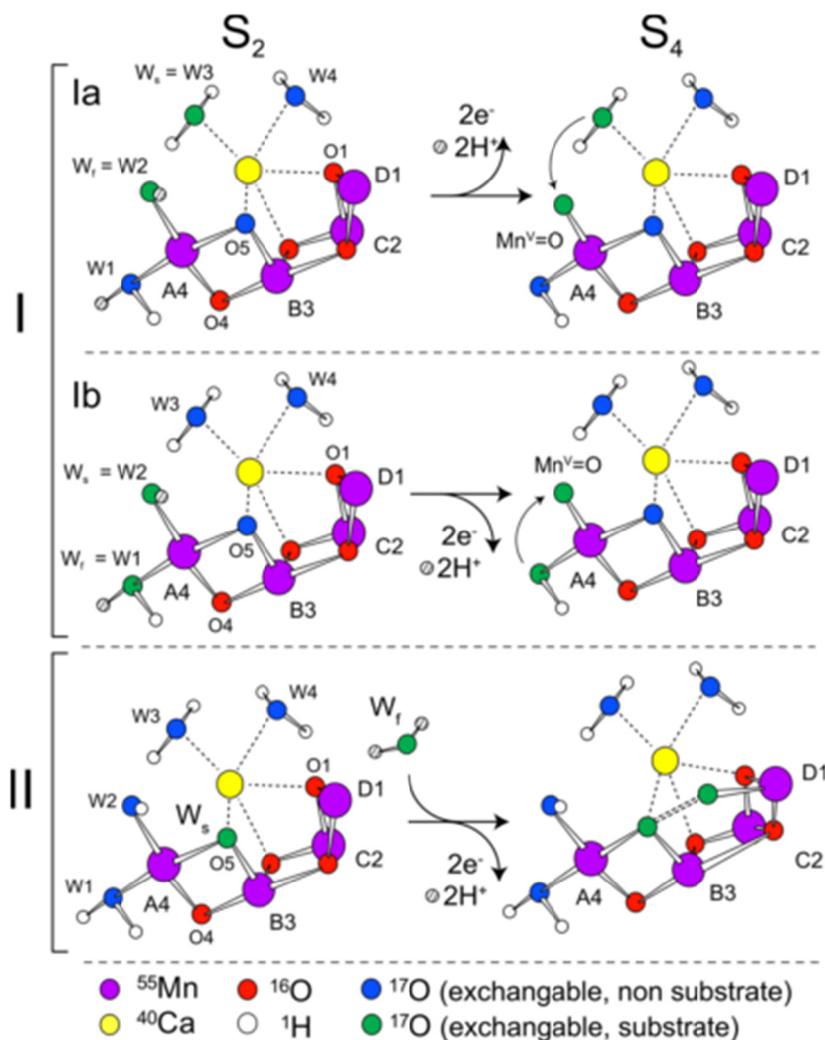


Figure 1-14 Possible pathways for O-O bond formation

The possible catalytic pathways of O-O bond formation as consistent with the dPSIIcc crystal structure of Umena et al. (25) and substrate exchange data by Rapatskiy et al (99). Class I (nucleophilic attack) with two possible modes Ia and Ib and class II (oxo/oxyl radical coupling) with one possible mode for O-O bond formation are shown. The left side structures represent the S₂ states, as probed by electron paramagnetic resonance/electron-electron double resonance detected NMR. The right side structures represent the inferred S₄ structures prior to the O-O bond formation and oxygen release. Figure adapted with permission from (99), copyright 2012, American Chemical Society.

1.3.9 Chloride and Calcium binding sites

Studies on PSII structures, where Cl⁻ was substituted with Br⁻ or I⁻ have identified two chloride binding sites in the vicinity of the Mn₄CaO₅-cluster (101, 102). Due to the limited resolution of 3.6 Å, the assignment of chloride and calcium was not possible in the mPSIIcc crystal structure (24). In the 2.9 Å resolution structure of dPSIIcc only one chloride binding site was identified (23) with a distance of 6.5 Å to the Mn₄ of the

Mn₄Ca-cluster (Figure 1-15 A). It is coordinated by amino acid residues and sits close to the entrance of the putative proton channels. The Cl⁻ was considered to have influence on the pK_a value of the adjacent amino acids and thus affect proton escape from the Mn-cluster (103). Above all, Cl⁻ is known to be essential for a fast turnover of water oxidation in PSII and might be a direct ligand stabilizing the WOC (101, 104, 105). The Q_B site in PSII binds inhibitors (herbicide molecules) with high affinity. The inhibitors compete with the native PQ molecules and are able to block the ET from Q_A to Q_B. In the herbicide-bound dPSIIcc structure two chloride binding sites with different occupancies for one chloride have been found, named Cl-1A (~30%) and Cl-1B (~70%) (Figure 1-15 B) (106). These different occupancies are interpreted as a movement of one chloride between the two binding sites coupled to proton transfer away from the WOC during water oxidation. It is further proposed that upon treatment with terbutryn and binding to the Q_B site at the acceptor side, the donor side is structurally affected (106). The presence of only one Cl⁻ binding site is consistent with studies of PSII from spinach (107). Deviating from these findings, the dPSIIcc crystal structure of Umena et al. revealed three chloride binding sites denoted as Cl-1, Cl-2 (see Figure 1-15 C) and Cl-3 (see Figure 1-16). The first two chloride binding sites are in accordance with the Br⁻/I⁻ substitution studies by Kawakami et al. as mentioned before (101). The observation of only one of these two in the 2.9 Å PSII crystal structure suggests a weak binding of Cl-2 to its binding site and thus it might be impossible to observe it at the lower resolution (85). Cl-1 is located with 6.7 Å distance to Mn₄, identical to the one binding site found in the dPSIIcc structure of Guskov et al. (23). The other two binding sites were located additionally. Cl-2 is located at a distance of 7.4 Å to Mn₂. The chloride in the binding site Cl-1 interacts with two water molecules at 3.0 and 3.5 Å distance and two amino acid residues D2-Lys 317 and the backbone nitrogen of D1-Glu 333. The second chloride in binding site Cl-2 interacts with two water molecules at 2.9 and 3.2 Å distance and the backbone nitrogens of Asn 338 and Glu 354 (85). As the binding of the Cl-1 and Cl-2 is predominantly established by rather weak hydrogen bonds, an easy release of Cl⁻ would result in an inactivation of water oxidation, whereas a reactivation is possible by rebinding of Cl⁻ to PSII with concurrent recovery of oxygen evolution (85).

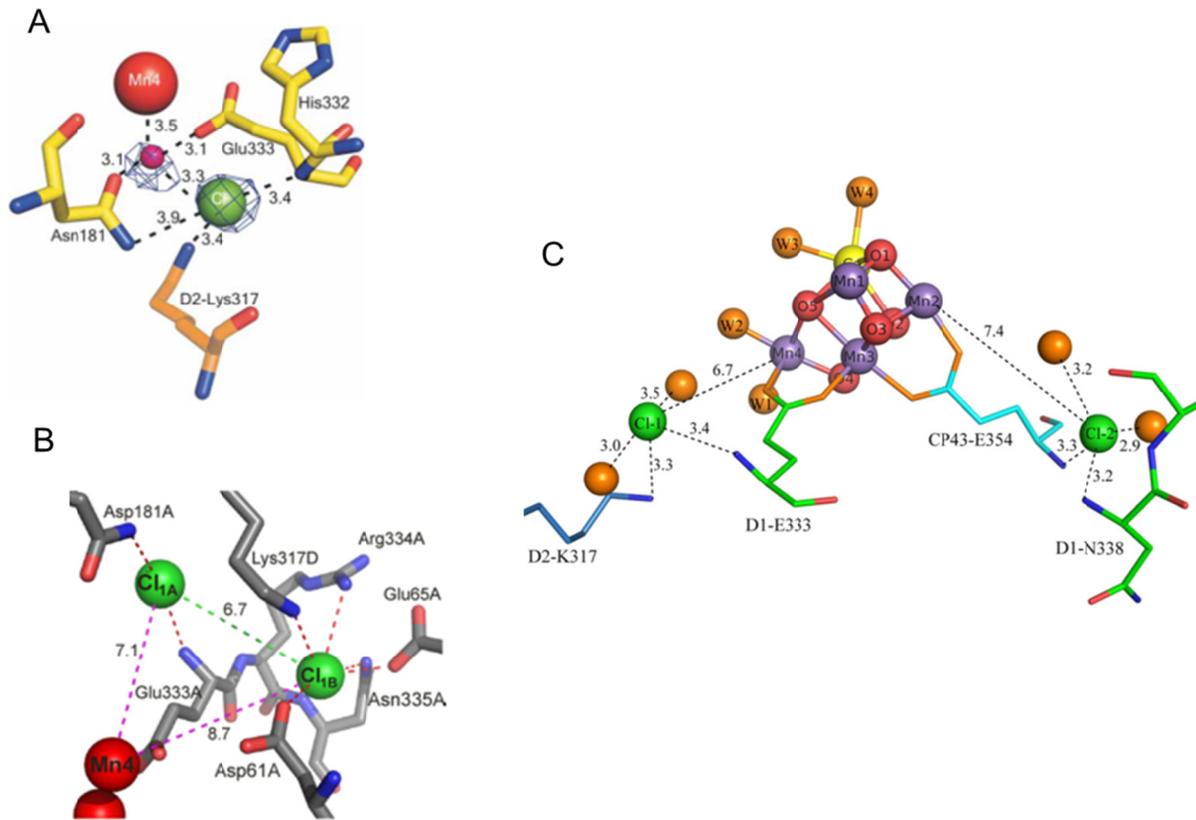


Figure 1-15 Comparison of Cl⁻ binding sites in the vicinity of the Mn₄CaO₅-cluster

A) Position of the Cl⁻ ion (green sphere) in the 2.9 Å resolution dPSIIcc structure, Mn4 (red) of the Mn₄Ca-cluster, coordinating amino acids (as labeled) and a putative water molecule (purple sphere), distances are given in Å. Figure taken from (23), reprinted by permission from Macmillan Publishers Ltd: [Nature Structural & Molecular Biology], © 2009. B) Cl⁻ ions (green) of the 3.2 Å resolution herbicide-dPSIIcc structure, Mn4 (red) of the Mn₄Ca-cluster, coordinating amino acids (as labeled) This research was originally published in (106), the American Society for Biochemistry and Molecular Biology. C) Chloride binding sites Cl-1 and Cl-2 (green) in the 1.9 Å resolution dPSIIcc structure with the surrounding amino acid residues (as labeled) and the Mn₄CaO₅-cluster (Mn in purple, oxygen in red, Ca in yellow) with bound water molecules (orange). Hydrogen bond distances of the chloride binding sites are given in Å. Figure taken from (85) with kind permission from Elsevier.

The additional Cl-3 is located 25 Å away from the Mn₄CaO₅-cluster between subunits PsbU and PsbV (Figure 1-16) surrounded by six water molecules, which implies a rather weak binding (85). Further three Ca²⁺ binding sites at the luminal side of PSII have been found by Umena et al. (25) (Figure 1-16). (Note that a fourth Ca²⁺ binding site was found for only one monomer of the PSII dimer and thus was excluded from any discussion in the publication of Kawakami et al. (85).) Two Ca²⁺ ions are in a vicinity of ca 40 Å away from the Mn₄CaO₅-cluster, the third is located 36 Å away. The Ca²⁺ ion located in PsbO has been revealed by Loll et al. (108) and two Ca²⁺ ions in PsbK and PsbO have been found in the dPSIIcc crystal structure by Guskov

et al. (23). It is discussed that Ca^{2+} -PsbO may have an auxiliary role to facilitate H^+ ejection from the proton channel (23). The role of further Ca^{2+} binding sites (Ca-2 and Ca-3, Figure 1-16) remains a matter of debate and it is questioned if these are all physiological functional binding sites as they are rather in the surface or the periphery of the protein subunits and Ca^{2+} is present in the crystallization condition and thus they are much likely believed to be incorporated during crystallization. An answer to this issue may be obtained by examining the functional role of the surrounding amino acid residues of these Ca^{2+} binding sites (85).

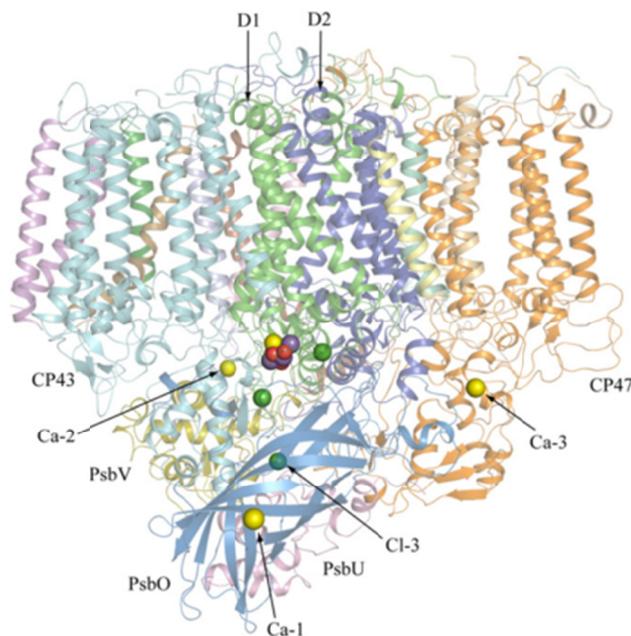


Figure 1-16 Additional Ca^{2+} and Cl^- binding sites in dPSIIcc

One monomer of the 1.9 Å resolution dPSIIcc structure is shown along the membrane plane, with core and extrinsic subunits in cartoon mode and labelled. Mn_4CaO_5 -cluster presented with manganese in purple, oxygen in red and calcium in yellow. Ca-1, Ca-2, Ca-3 as indicated in yellow and Cl-3 as indicated in green. Figure taken from (85), with kind permission from Elsevier.

For a comparison of chloride and calcium ions found in the two dPSIIcc structures (2.9 Å and 1.9 Å resolution), as well as an overall comparison of the subunits, cofactor and water molecules see Table 1-1.

	2.9 Å	1.9 Å
Protein subunits	20	19
Chlorophyll <i>a</i>	35	35
Pheophytin <i>a</i>	2	2
β Carotene	12	11
Integral lipids	25	20 (+3)
Calcium ions	3	5/4
Chloride ions	1	3
Plastoquinones	3	2
Water molecules	(1)	1438/1357

Table 1-1 Summary of the subunit and cofactor composition of dPSII_{cc} crystal structures

Listed are the subunit and cofactor composition of the 2.9 Å (23) and the 1.9 Å (25) resolution dPSII_{cc} crystal structures (per monomer).

1.4 Membrane protein crystallization

In order to obtain detailed structural information of a protein, as mentioned earlier, XRD is the most powerful method. The prerequisite and at the same time one of the most difficult steps is to achieve good diffracting high quality crystals. The main steps that lead to high quality crystals are the following: protein growth and purification of the target protein, search for initial crystallization conditions, optimization of the crystal quality, searching for an ideal condition for XRD measurements (109). Despite technical advances like crystallization robots, crystallization and optimization remains a matter of trial and error, a time and sample consuming procedure. The crystalline state is a well ordered three-dimensional arrangement of the membrane protein. Crystals can only be formed when the protein molecules arrange in an ordered fashion while they are in the supersaturated state. When a solution of proteins is mixed with the crystallizing reagent it can reach three different states of solubility, as shown in a schematic crystallization phase diagram (Figure 1-17). In the unsaturated region or nonsaturated zone, the protein is fully dissolved and cannot form crystal contacts to start formation of a three-dimensional arrangement. In the saturated

region or metastable zone no crystal nucleation occurs but existing crystals can further grow in size in this concentration region. The supersaturation zone can be divided into the nucleation zone, where crystal nucleation occurs spontaneously and crystals grow, and the precipitation zone where only amorphous aggregates appear (110). The optimum concentration for crystallization of a protein is thus, somewhere in the labile zone of supersaturation. The insights into the crystallization process are still very limited and until today there are no systematic methods that ensure a successful crystallization experiment (111). Once a crystal has appeared the nucleation can be induced in the respective concentration zone by the technique of seeding (112). Crystal nucleation and growth is dependent on a multitude of factors, such as sample concentration, buffer system, precipitant, additives, detergent, temperature and pH value. One of the most important starting points is the sufficient purity of a homogenous protein solution which is then mixed with the crystallizing agent. The precipitant pushes the protein into a supersaturated state by reinforcing the attractions among the protein molecules or increases the molecular crowding and can be a salt or a polyethyleneglycol (PEG) of various chain lengths (111). The buffer (usually 20-200 mM) maintains the pH value of the system, which is of importance for the protein stability and the solubility which can dramatically change as the pH is changed. Often small salts are used as additives, which can modify and/or stabilize the conformation of the protein and manipulate protein-protein and protein-solvent interactions and change the surface energy of the crystal. The "Hofmeister-series" gives an empirical scale for the efficiency of ions in precipitating protein molecules in solution (113).

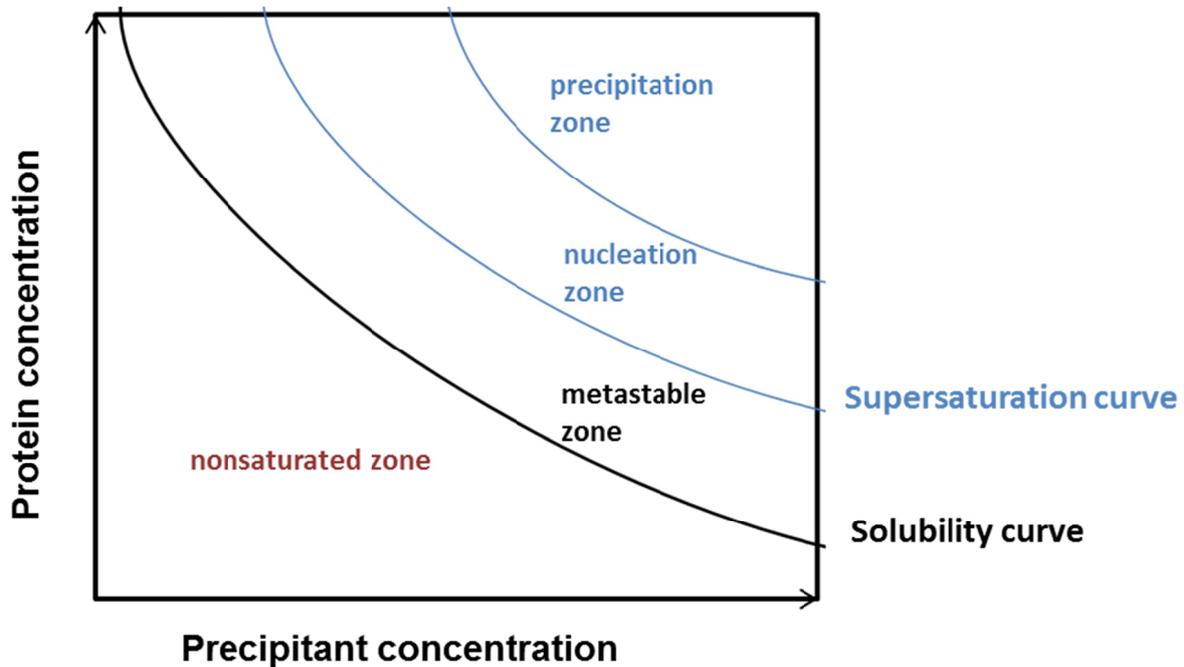


Figure 1-17 Schematic crystallization phase diagram

Illustrated is the protein concentration against the precipitant concentration. The concentration area is divided into the nonsaturated (n), metastable (m) and supersaturated (s) (nucleation and precipitation) zones, divided by the supersaturation and the solubility curves. In the n region no crystals form, the m region supports crystal growth but no nucleation, in the s zone nucleation and crystal growth occur. Above a certain protein concentration the precipitation zone is reached and only amorphous precipitation occurs.

The most common techniques for crystallization are vapour diffusion, batch crystallization and dialysis, each method intends to bring the protein in a supersaturated state. In the vapour diffusion method, a droplet containing protein and precipitant (1-10 μl) are equilibrated against a reservoir (>100 μl) that contains a solution with a higher precipitant concentration than the droplet, all in a closed system. The protein containing droplet increases in concentration through reduction of volume and reaches supersaturation. In the batch method protein solution and crystallization solution are mixed, directly bringing the protein in a supersaturated state. In a sealed capillary or plate, the crystallization eventually occurs after incubation time (114). In the dialysis method protein solution and crystallizing reagent are directly mixed and equilibrated against a higher concentrated solution separated through a semipermeable membrane. For a recent review see (115). Membrane proteins are particularly difficult to handle, because of their amphipathic character expressed through hydrophilic and predominantly hydrophobic surfaces. The use of

detergent molecules is a necessary tool to work with membrane proteins. The appropriate detergent keeps the protein soluble in solution and is in the final step cocrystallized with the protein (116). Therefore the choice of detergent is of great importance as it interacts with the protein and contributes to the interactions and contacts in the protein crystal (117). Detergents are surface-active molecules that can self-associate and in a certain concentration bind to hydrophobic surfaces. They can be classified depending on their headgroup into ionic, nonionic and zwitterionic detergents. The mildest ones are the non-ionic detergents. Their behavior is strongly dependent on their headgroup and chain length. Detergents also have an amphipathic character. What distinguishes them from lipids is the tendency to self-associate and form multimolecular micellar structures. At a specific detergent-dependent concentration, the critical micellar concentration (CMC), the monomers form self-associated micelles (116). The CMC is dependent on pH, ionic strength, temperature and other molecules like lipids, proteins and detergents in the solution. Above the critical solubilization concentration (CSC), a detergent is able to solubilize a membrane protein to create water soluble protein-detergent complexes. The CSC is higher than the CMC and depends on the membrane protein concentration (118). Once membrane protein crystals have formed, they can be divided into type I, II and III, depending on the way they arrange (Figure 1-18).

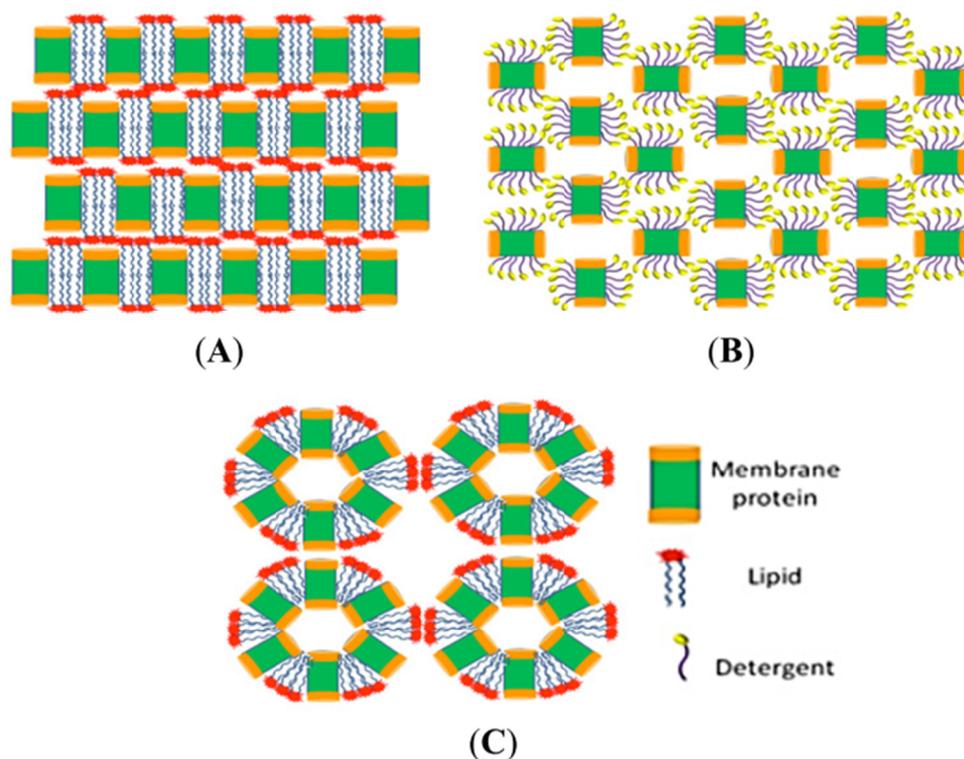


Figure 1-18 Crystal types of membrane proteins

(A) Type I crystals are 2D layers of stacked membrane proteins; each layer contains proteins oriented as in a bilayer with the hydrophobic surfaces providing the crystal contacts. (B) Type II crystals are cocrystallized protein-detergent complexes, the hydrophilic surfaces of detergents provide the crystal contacts. (C) Type III crystals originate from vesicular proteoliposomes, made of closed loops of stacked 2D membrane proteins, the inner and outer surfaces are hydrophilic. Figure taken from (115), copyright (2013) lies with the authors, original work can be found here: <http://www.mdpi.com/1422-0067/14/6/11643>.

1.4.1 Crystallization of PSIIcc

Several ways for improvement of the 2.9 Å resolution dPSII structure (23) have been tried in the group of Prof. Dr. A. Zouni, ahead of and during this work. Besides the improvement of the structure a second aspect regarding to function or structure was always considered. One reason for cocrystallization of dPSII with the herbicide terbutryn was to avoid microheterogeneity of the Q_B site, which was hoped to improve the crystal diffraction (106). This study resulted in the first herbicide-bound dPSIIcc structure at a resolution of 3.2 Å. The crystallization of the monomeric PSIIcc structure by Broser et al. intended to establish a different space group and/or different protein contacts between the smaller detergent/PSII-monomer complexes in the crystal. The study resulted in the first mPSIIcc structure with 3.6 Å resolution and

a different space group (C222₁) suitable for orientation-dependent spectroscopy (24). During my diploma thesis (119) an exchange of detergent molecules with native lipids was tried, to avoid heterogeneity induced by detergents and in order to stabilize the dPSIIcc, but this did not result in an improved diffraction of crystals. In 2011, a drastic improvement of the dPSIIcc to 1.9 Å resolution was presented by Umena et al. (25). The dPSIIcc from *T. elongatus* have been isolated with 0.6 % βDM (120), whereas dPSIIcc from *T. vulcanus* have been treated with 1.2 % βDM for extraction and an additional second detergent HTG (Figure 1-11 B, page 26) (25) unmentioned in the publication and only visible in the 1.9 Å resolution dPSIIcc crystal structure (PDB code 3ARC). The resulting crystal improvement included a dehydration procedure of the crystals prior to diffraction measurement. Dehydration is a popular method to improve the diffraction of a crystal by increasing the order and molecular contacts within a crystal. It was found empirically that dehydration works best with small sized detergents, particularly because it is impossible to shrink the volume of an existing large micelle surrounding the protein (111). Thus the mixture of the two detergents βDM and HTG could have manipulated the detergent belt and altered the micellar structure around the protein in the crystal as compared with βDM-PSII which exhibits rather large and stable micellar belts (121). Most likely the detergent belt manipulation together with the applied dehydration procedure led to the obtained improvement. With dPSIIcc crystals solely treated with βDM it was not possible to induce an improvement of the diffraction quality with a dehydration procedure. Detailed knowledge of the protocol, most of all the unknown concentration of the second detergent HTG, prevented us to obtain similar results. The difference in the choice of detergent(s), the detergent(s) concentration, purification and the crystallization procedure furthermore contribute to a differing lipid and detergent composition of the two structures. This fact encouraged us to proceed with a different strategy, as presented in chapter 3. It is also of great interest to reveal all natively bound lipids in the PSIIcc structure as they are important cofactors (see Chapter 1.3.6 Integral lipids). A comparison of lipid and detergent molecules found in both dPSIIcc structures is presented in Table 1-2.

Lipids	2.9 Å	1.9 Å
MGDG	11	6
DGDG	7	5
SQDG	5	4
PG	2	5
Unknown alky chains	-	15
Unknown diglycerides	-	3
Detergents		
βDM	7	6/5
HTG	-	9/10

Table 1-2 Lipid and detergent comparison of dPSI_{lcc} crystal structures

*Content of lipid and detergent molecules within dPSI_{lcc} per monomer, derived from dPSI_{lcc} crystal structures of *T. elongatus* at 2.9 Å resolution (23) and of *T. vulcanus* at 1.9 Å resolution (25).*

1.4.2 X-ray radiation damage

Theoretical introduction

X-ray damage of biological macromolecules results from the absorbed photons, when protein crystals are exposed to ionizing radiation of an X-ray beam. They generate free radicals, which can diffuse through the crystal and eventually recombine. As a consequence the atomic B-factor (or temperature factor) and the unit cell volume can increase, disulfide bond breakage and decarboxylation of acidic residues can occur (122-124). The effects can be diminished by cooling a crystal to around 100 K, which can immensely improve the crystal lifetime. In order to cool crystals to 100 K the addition of a cryoprotective agent is necessary to prevent crystalline ice formation of the water within the crystal. Ice formation disrupts the macromolecular crystal lattice and reduces diffraction quality in most cases. Henderson and Garman calculated an absorbed dose of $2 - 3 \times 10^7$ Grays (Gy or J/kg) (125, 126) as the value required to totally destroy crystalline diffraction of a protein crystal. This dose is easily obtained by third generation synchrotron sources during collection of one data set (127).

When photons interact with a crystal a) Thomson scattering, b) Compton scattering as well as c) photoelectric absorption occur (Figure 1-19). Thomson scattering is an elastic scattering arising from the interaction of the X-ray photon with the electrons of the atoms and results in the aimed diffraction pattern. While Compton scattering the photon scatters incoherently from electrons, which means they give a small amount of energy to the electron, which can then be ejected from the atom. During photoelectric absorption an X-ray photon is absorbed and an inner shell electron is ejected from the atom. The so called primary damage is caused by photoelectric absorption and Compton scattering, and occurs on a timescale of fs (124). X-ray irradiation of water molecules in the solvent area of the crystal releases highly reactive species, including hydrogen and hydroxyl radicals, and hydrated electrons (e^-_{aq}) (128). The reactive species can diffuse, then further break bonds within a macromolecule and generate more radicals which is referred to as secondary damage and occurs in a timescale of picoseconds to milliseconds (124).

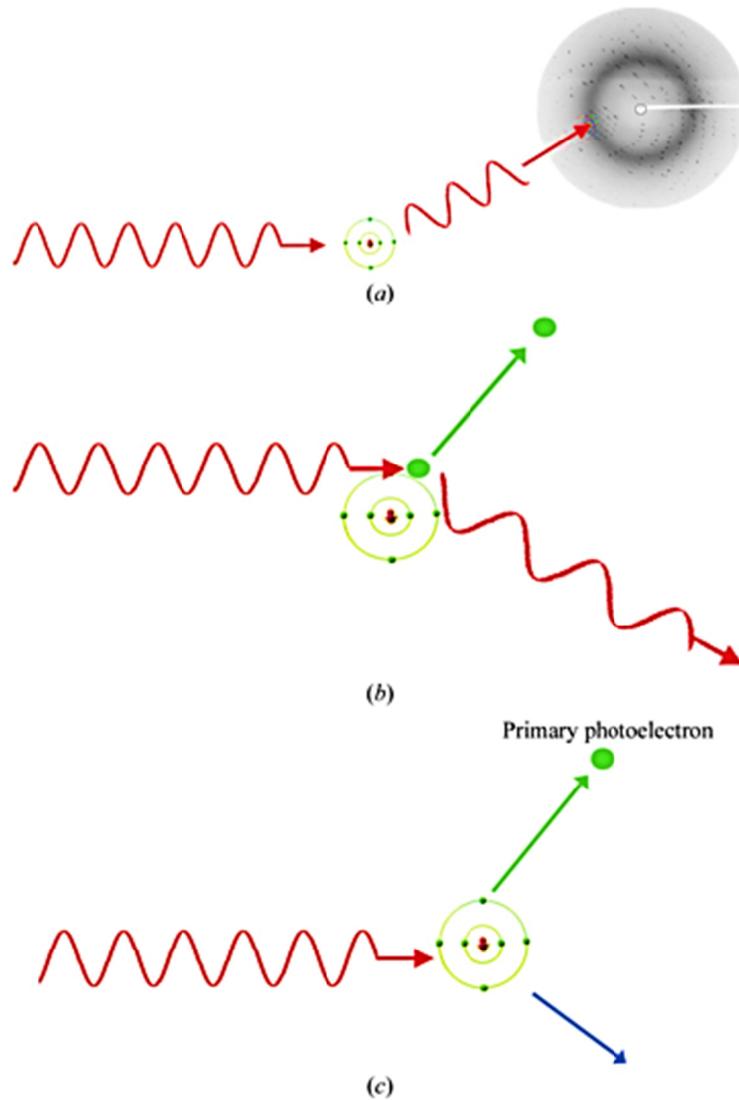


Figure 1-19 Primary X-ray interaction processes with atoms of crystals and solvent

(a) Thomson scattering (elastic), the waves are phase-shifted by 180° when scattering and add vectorially, building the diffraction pattern. (b) Compton scattering (incoherent), the X-ray transfers energy to an atomic electron and thus has lower energy (higher wavelength) after the interaction. Energy is lost in the crystal, contributing to the absorbed dose. (c) Photoelectric absorption, the X-ray transfers all its energy to an atomic electron, which is then ejected and can give rise to the ionization of up to 500 other atoms. The excited atom can then emit a characteristic X-ray or an Auger electron to return to its ground state. Figure taken from (123), copyright © Garman 2010.

Radiation damage to the Mn-cluster

A critical problem of the elucidation of the WOC with SR is the high radiation sensitivity of the redox-active, high valent Mn_4CaO_5 -cluster when XRD is performed. Mobile e^-_{aq} and radicals are able to change the oxidation states of the Mn ions (129, 130). Due to the high electron affinity of the Mn in the Mn-cluster, the exposure of PSII crystals with X-rays leads to the reduction of Mn^{III} and Mn^{IV} to Mn^{II} . This was examined with EXAFS studies on PSII solutions and crystals at low temperatures (100K) (129, 131), (Figure 1-20). XRD measurements of PSII crystals are commonly carried out at cryo temperatures around 100K. The reduction to Mn^{II} is combined with a change in the environment of the Mn and a disruption of μ -oxo-bonds and modifications in amino acid and Mn-Mn distances, as compared to the undamaged Mn_4CaO_5 -cluster (131). From radiation damage studies on PSII it is deduced that in all current XRD studies the Mn_4CaO_5 -cluster is reduced at levels around approximately 80% (for the structures reported in the following references (19, 22, 23, 46, 132), and 25% for the latest reported high-resolution structure by Umena et al. (25), the latter being applied to a much lower X-ray dose. Predominantly photoreduction directly depends on the applied X-ray dose and energy of the photons, but further influences such as temperature additionally play a role, as a decrease of temperature decreases the radiation damage (Figure 1-20), in particular the secondary damage (122, 131). To circumvent the problem of radiation damage of the OEC a method is needed that collects diffraction data before destruction of the sensitive metal sites occurs, as will be presented in Chapter 4. Another method that avoids radiation damage of the OEC was recently applied by Glöckner et al. who investigated the structural changes of the Mn_4CaO_5 cluster during the S-state transitions by using X-ray absorption spectroscopy (XAS) (133).

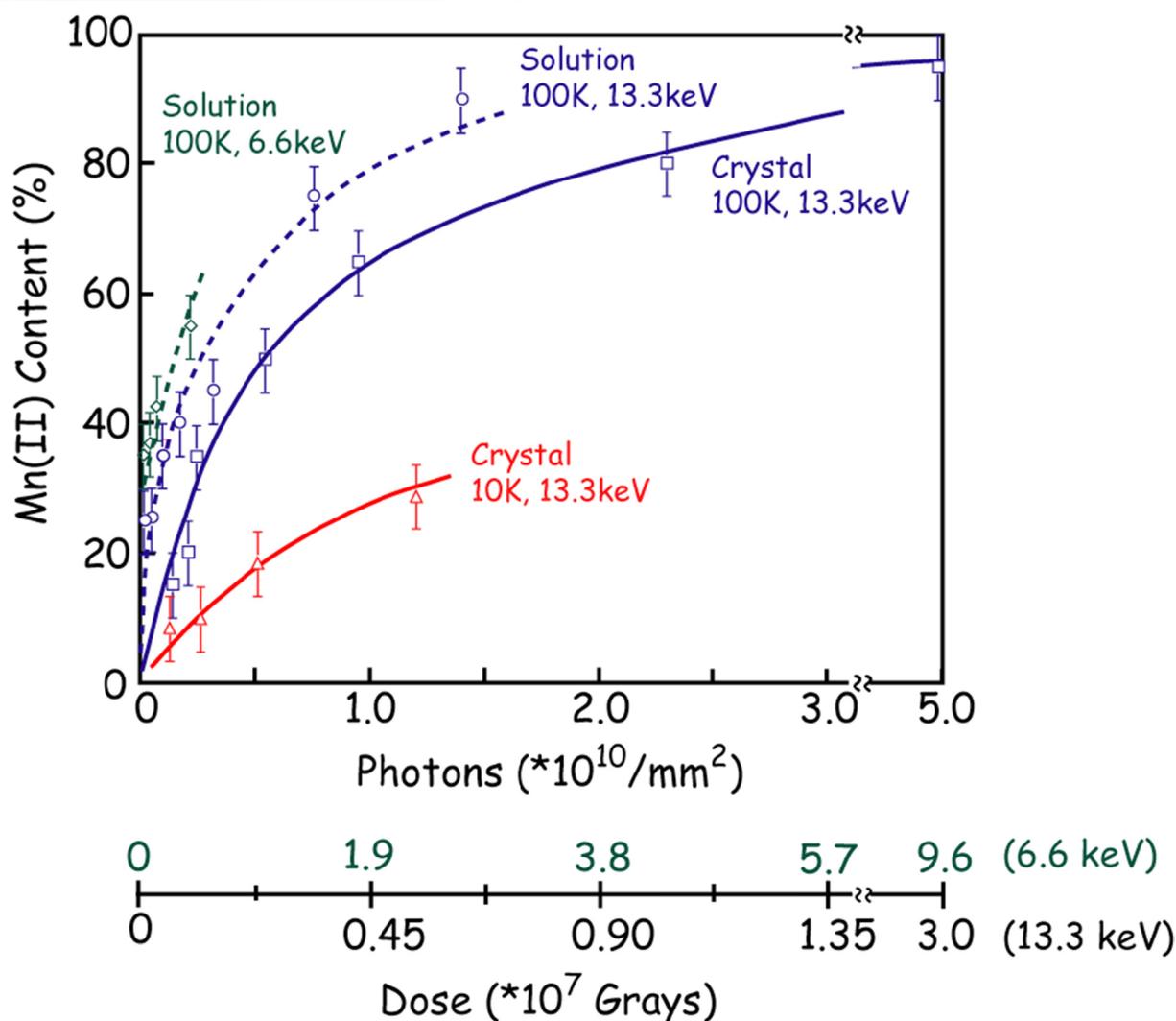


Figure 1-20 Increasing Mn(II) content in PSII caused by radiation damage

The blue line shows the Mn(II) content of PSII crystals at 100K and 13.3 keV (0.933Å) X-ray radiation, values typical for XRD data collection. The points on the curve represent samples that absorbed between 0.14 and 5×10^{10} photons per mm^2 . At the dose of 2.3×10^{10} photons per mm^2 which is 66 % of the average dose used in crystallography (3.5×10^{10} photons per mm^2), crystals already contain 80 % of Mn(II). The dashed blue line shows a slightly higher damage profile for PSII solution. The dashed green line shows the Mn(II) for PSII solution at 100K and 6.6 keV (1.89 Å), at this energy anomalous diffraction measurements are performed. This results in even higher damage profile. The solid red line shows the Mn(II) content for PSII crystals conducted at 10 K, 13.3 keV, which results in an decrease of damaged Mn, decrease in temperature thus provides a way to reduce radiation damage. Figure taken from (131), copyright (2005) National Academy of Sciences, USA.

1.4.3 Serial femtosecond X-ray Crystallography at an XFEL

The so called serial femtosecond (fs) X-ray crystallography, a new established method for the unravelling of dynamic enzymatic processes in protein crystals, accounts for the problem of radiation damage (134). A fs-laser is used as a beam,

providing very intense X-ray pulses, which are in the same time so short (< 70 fs) that diffraction data can be collected before the onset of radiation damage occurs, even at RT. In X-ray free electron laser (XFEL) studies, specific radiation damage and its temperature dependence, which arises from radical migration during SR XRD are no more a limiting factor due to the short fs X-ray pulses. Single XRD crystal 'snapshots' are collected from a hydrated stream of nanocrystals, where crystals are randomly orientated and a full dataset is collected from millions of single snapshots. This approach had been successfully tried with the membrane protein PSI (135) and was carried out at the newly-built fs laser at the Linac Coherent Light Source (LCLS) in Stanford, CA, USA. As radiation damage is the most serious problem for PSII crystals at conventional SR sources, this method provided a new way to circumvent the destructive processes that foremost alter the OEC within PSII. It further presents a new way to study the enzymatic S-cycle of PSII at RT in a time-resolved manner. Following the structural dynamics by simultaneous X-ray emission spectroscopy (XES) measurements is possible and a further benefit of the method.

1.5 Aims of this work

Two approaches have been aimed on during this work. The first study (i) focused on a new static picture of PSII as close to the native state as possible. For this an XRD crystal structure of PSII should be attained by establishing a new protocol using a detergent dissimilar to native integral lipids of PSII with the aim of retaining and stabilizing the native PSII subunit cofactor complex. The second study (ii) focused on the enzymatic processes during the catalytic S-state cycle, to unravel the dynamic mechanism of water oxidation. In order to achieve this goal a protocol for PSII microcrystals should be established to perform serial fs X-ray crystallography and combined XES of PSII.

(i) When this work was started the best crystal structure of dPSIIcc had been solved from cyanobacterial *T. elongatus* to a resolution of 2.9 Å (23). The information about the PSII cofactor composition and especially the WOC were still limited to a certain extent, due to the medium resolution. The applied purification and crystallization methods on dPSIIcc did not exceed the 2.9 Å resolution structure and a different attempt to improve the structural knowledge about dPSIIcc was considered. The PSIIcc harbors a very high number of integral lipids. The latest structure of *T. elongatus* unraveled 25 integral lipids per monomer (23). Besides the lipids an amount of 14 detergent molecules β DM has been found incorporated into the crystal structure of dPSIIcc. A possible exchange of native lipids with detergents that causes intramolecular heterogeneities was assumed, due to a highly structural homogeneity of the detergent β DM and one particular integral lipid; the DGDG. The detergent β DM has been routinely used for PSII extraction and purification. It co-crystallizes with the protein and forms specific interactions that influence the packing of the protein within the unit cell of the crystal. In order to prevent a possible exchange of native lipids with detergent molecules and thereby stabilizing the native dPSIIcc structure, a structural dissimilar detergent should be introduced. The mild, non-ionic detergent C₁₂E₈ does not possess a prominent sugar headgroup as β DM, but features an ether chain (E₈) with a hydroxyl headgroup and a long hydrocarbon chain (C₁₂). The difference in the overall structure made it suitable for the study. First tests with C₁₂E₈ showed high PSII oxygen evolution activity after extraction from the thylakoid membrane and the extraction yield was comparable to that derived with β DM. A new purification protocol

to gain highly active and homogeneous purified dPSIIcc solution had to be established, followed by the crystallization of the protein. It was hoped to result in an improved resolution, on new information on cofactors and integral lipids and retain dPSIIcc as close to the *in vivo* state as possible. During this work Umena et al. published an improved dPSIIcc crystal structure at 1.9 Å resolution. This dPSIIcc structure unraveled an even higher number of incorporated detergent molecules inside PSII as a second detergent (HTG) was used additionally to β DM. This result was a further impulse to achieve a structure where no incorporation of detergent molecules and/or exchange with integral lipids should have occurred. The stabilization of the whole native dPSIIcc by the detergent $C_{12}E_8$ was anticipated to be a possible result. The detergent $C_{12}E_8$ further produces its own detergent protein complexes that may exhibit new contacts within a unit cell and a different packing may result in an improved resolution. Further a dehydration method, a post-crystallization procedure which was also applied to dPSIIcc crystals by Umena et al. (25), should be adapted to the $C_{12}E_8$ -dPSIIcc crystals.

(ii) The new established method of serial fs X-ray crystallography should be applied to dPSIIcc microcrystals. This method results in intact XRD dPSIIcc crystal structures, and additionally gives the possibility to measure the enzymatic processes without radiation damage at RT. A combination with simultaneous XES additionally provides a way to unravel oxidation states and bond distances of the catalytic manganese cluster. The prerequisite for first measurements at the fs-X-ray laser was to routinely gain microcrystals (10-30 μ m) of dPSIIcc. The size of PSII crystals obtained with batch crystallization, which diffracted to 2.9 Å resolution, have been in the size range of 300-600 μ m. A crystallization protocol to gain microcrystals with good yield and diffraction quality had to be established. With this approach the dPSIIcc crystal structure should deliver a picture of an intact OEC without radiation damage. The ultimate goal of this method should be to elucidate various catalytic states of the S-cycle of water oxidation with the help of additionally probing the local electronic structure of the WOC with simultaneously using fs-X-ray emission spectroscopy. To understand the O-O bond formation in a time resolved manner is one of the most amazing challenges for protein scientists working on Photosystem II. This study should be a first step towards this ultimate goal.

2 Materials and methods

2.1 Chemicals, buffers and materials

Chemicals

All chemicals used for this work were of analytical grade. Octaethylene glycol monododecyl ether, Betaine monohydrate and Polyethylene glycol monomethyl ether 5000 were supplied by Aldrich. n-Dodecyl- β -maltoside was supplied by Glycon. All other chemicals were supplied by Merck, Fluka and AppliChem. For all aqueous buffers and solutions, filtered and autoclaved Milipore MilliQ water was used.

Buffers

A	40 mM MES-NaOH pH 6.0, 10 mM CaCl ₂ , 500 mM betaine, 0.013 % (w/w) C ₁₂ E ₈
B	40 mM MES-NaOH pH 6.0, 10 mM CaCl ₂ , 500 mM betaine, 0.013 % (w/w) C ₁₂ E ₈ , 1 M NaCl
Anode buffer	25 mM imidazole/ HCl pH 7.0
Cathode buffer	50 mM tricine, 7.5 mM imidazole, 0.02 % Comassie G-250
Cathode buffer/10	50 mM tricine, 7.5 mM imidazole, 0.002 % Comassie G-250
Cb0	20 mM MES-NaOH pH 6.0, 10 mM CaCl ₂ , 500 mM betaine, 0.013 % (w/w) C ₁₂ E ₈
Cb100	20 mM MES-NaOH pH 6.0, 10 mM CaCl ₂ , 500 mM betaine, 100 mM Mg ₂ SO ₄ , 0.013 % (w/w) C ₁₂ E ₈
MCM	20 mM MES-NaOH pH 6.5, 10 mM CaCl ₂ , 10 mM MgCl ₂
MC*M*	MCM + 0.15 M MgCl ₂ , 0.3 M CaCl ₂
MCMB	MCM + 500 mM betaine
MCMG	MCM + 25 % (w/v) glycerol
MMCM	MCM + 500 mM mannitol

Crystallization screens

The following crystallization screens have been used to obtain crystal hits for C₁₂E₈-PSII. Hampton Research: ProPlex Screen HT-96, PEG/Ion Screen, Natrix, MembFac. Molecular Dimensions: ProPlex, PACT^{premier}TM, JCSG-*plus*, MIDASTM, Structure Screen 1+2, MemGold. Qiagen: MbClass Suite, MbClassII Suite, Jena Bioscience: JBScreen Membrane

Chromatography materials

For chromatographic separation of protein material an ÄKTATM Explorer FPLC System (Amersham Pharmacia Biotech) was used. Anion exchange chromatography was performed with columns (Kronlab GmbH) of various sizes, self-packed with ToyoPearl DEAE 650 S Sepharose (Toso Haas). Strong anion exchange chromatography was performed on a prepacked MonoQ column (h 10 cm, ø 1 cm). For size-exclusion chromatography a pre-packed Superose 6 column (h 30 cm, ø 1 cm) (GE Healthcare) was used.

2.2 Methods

2.2.1 Cell cultivation

Cyanobacterial cells of *T. elongatus* were grown in a PBR25 photobioreactor (IGV Potsdam, Germany and Satorius-BBI Systems, Melsungen, Germany) at 49 °C. The cultivation volume of 32 l was continuously circulated and illuminated. The cultivation was carried out in the Castenholz Medium D and was constantly kept at pH 7.8 by automatically adding CO₂ to the suspension.

The growth was controlled by observing the optical density (OD) of the cell suspension starting at an OD of 0.15. Typically harvesting of the cells at an OD of 1.3 was carried out after 5-7 days (120).

2.2.2 Preparation of thylakoid membranes

Harvesting of the cells was followed by a washing step with ca 3 l buffer MCM, centrifugation at 4500 rpm for 5min in a Beckman centrifuge (JLA rotor). The

sediment was resuspended with ca 300 ml MMCM buffer containing 0.2 % (w/v) lysozyme. Incubation of the cells for 30 min was followed by disruption of the cells with a Yeda-Press at 30 atm nitrogen pressure. Broken cells were diluted with 3 l of MCM buffer and centrifuged for 5 min at 8000 rpm (JLA rotor) for sedimentation.

To reduce the amount of phycobilisomes in the sample, a washing step was introduced. Thylakoid membranes were washed twice with ca 6 l MC*M* buffer (JLA rotor, 8000 rpm, 5 min), salt concentration was then reduced again by washing with ca 3 l MCM buffer and the final sample was either in MCMB or in MCMG buffer.

2.2.3 Protein solubilisation

Solubilization of the thylakoid membranes was carried out under dim green light at room temperature by incubation with 1.2 % (w/w) C₁₂E₈ and few crumbs PEFA in buffer MCMB or MCMG for 5 min under gentle shaking. The incubation was then stopped by adding an equal amount of buffer Cb0 and centrifugation at 4°C (Beckman, 70 Ti rotor, 48,000 rpm, 20 min). The supernatant containing the solubilized protein mixture was then used for subsequent purification steps.

2.2.4 Protein purification

Purification steps were performed under dim green light, the chromatographic separation was carried out in a laboratory refrigerator (Unichromat 1500, UniEquip) at 6 °C. A Toyopearl DEAE 650 S column (110 ml, h 22 cm, ø 2.5 cm) was equilibrated to a conductivity of ~ 4.2 mS/cm using buffer Cb0 and Cb100. Before loading the protein mixture (50 ml, Chla concentration varied from 300-600 µM) onto the column, it was set to the same conductivity as the pre-equilibrated column for optimal binding. Washing at constant salt concentration for 2.5 column volumes (CV) at a flow rate of 2 ml/min was followed by gradient elution by instantly raising the conductivity (in 0.1 CV) to 5 mS/cm and slightly increasing it to 6.5 mS/cm for 3 CV at 2 ml/min. This resulted in elution of the protein at ca 6 mS/cm. The PS II fractions were centrifuged in Vivaspin 20 concentrators (100 kDa cutoff, Sartorius) at 4 °C with 3000 rpm to a volume of 1-10 ml for manual sample uploading with loop injection. The sample was

set to a conductivity of ~ 4 mS/cm and then loaded onto a second Toyopearl DEAE 650 S column (55 ml, h 22cm, ø 1.8 cm) which was pre-equilibrated to this conductivity. After washing with 2 CV at this constant salt concentration with a flow rate of 2 ml/min, the gradient part was run with 2 ml/min. A purification step of 1 CV with a conductivity of ~ 4.7 mS/cm was followed by performing a second step with a conductivity of 6.5 mS/cm for 2 CV resulting in an elution of PSII at a conductivity of ~ 6 mS/cm. As a third purification step a stronger anion exchange column, a prepacked MonoQ HR 10/100 column (1 CV 8 ml, h 10 cm, ø 1 cm) was introduced as a further purification step. The PSII fraction was loaded onto the column and washed at a conductivity of 9 mS/cm for 7 CV, using buffer A and B. A linear gradient to a conductivity of 35 mS/cm over 5 CV resulted in an elution of PSII at a conductivity of 22 mS/cm. High salt concentration was removed by washing the PSII fraction with a buffer containing 20 mM MES pH 6, 10 mM CaCl₂ and 0.013 % (w/w) C₁₂E₈ and the Chla concentration was adjusted to 2 mM for subsequent crystallization steps. Detection of the fractions was carried out with single wavelength detector at 280 nm using UNICORN 5.11 software (Amersham Biosciences). Peak identification was followed with a multiwavelength (200-750 nm) PDA detector 2800 (Knauer) using the ClarityChrom software (Clarity™) for evaluation.

2.2.5 Chlorophyll a concentration measurements

PSII incorporates 35 Chlorophyll *a* molecules per monomer which allows for determination of concentration by absorption measurements at 674 nm or 663 nm, and control at 750 nm (UV-VIS recording spectrophotometer, Shimadzu). PSII solutions were diluted in buffer Cb0 (1:1000), absorption measured at 674 nm, extinction coefficient ($\epsilon_{(674\text{nm})} = 69100 \text{ M}^{-1} \text{ cm}^{-1}$) or diluted in 80 % acetone (1:1000), absorption measured at 663 nm, extinction coefficient ($\epsilon_{(663\text{nm})} = 74000 \text{ M}^{-1} \text{ cm}^{-1}$). Recorded absorption was multiplied with path length of the cuvette (1 cm) and the extinction coefficient to determine the concentration of Chla. The protein concentration in g/l of dPSII can be calculated by dividing the obtained Chla concentration by 70 and multiplying it with the molarity of dPSIIcc (750,000 g/mol).

2.2.6 Crystallization of dPSIIcc for SR XRD measurements

To find an appropriate crystallization condition, crystallization screens were performed at a crystallization robot (Honeybee 963, Digilab) in 96 sitting drop well plates, utilizing 0.2 μ l PSII solution per drop and 200 μ l reservoir volume. PSII solutions were set to a Chla concentration of 1 mM and 2 mM and mixed 1:1 with the precipitation agent. Plates were covered with crystal clear sealing tape.

The dPSIIcc solution of 2 mM Chla (~ 21 mg/ml protein) was mixed 1:1 with the crystallization reagent (0.1 M TRIS pH 7.5, 0.1 M $(\text{NH}_4)_2\text{SO}_4$, 15-17 % (w/v) PEG 5000 MME). Crystals of dPSIIcc were obtained with the sitting drop method (MRC Maxi 48-well crystallization plate, Swissci) or the microbatch method (96 well Imp@ct plate, Greiner) after 1-2 days at 20 °C and further growth occurred within a few days. Crystals remained stable in the crystallization condition for a period of one to two weeks at RT.

2.2.7 Size exclusion chromatography

To differentiate between the monomeric and the dimeric PSII fractions size exclusion chromatography was performed. PSII samples (0.13 mM Chla, 300 μ l) were run on a Superose 6 column (\varnothing 10mm, h 30cm, GE Healthcare). Buffers Cb0/Cb100 were run at a constant salt concentration of 25 mM MgSO_4 and a flow rate of 0.3 ml/min. The protein peaks were detected at a wavelength of 280 nm. Retention times of standard runs of monomeric and dimeric PSIIcc were used to identify the results.

2.2.8 Oxygen evolution measurements

Oxygen evolution measurements of PSII solutions were carried out with a Bachofer Clark electrode. The oxygen activity number is a dimension that allows clarifying whether the PSII is enzymatically functioning or intact. For the measurements samples were excited with a xenon flash lamp with a flash frequency of 1 Hz. Samples were diluted in buffer MCM to a final concentration of 20-50 μ M Chla. The artificial electron acceptors $\text{K}_3[\text{Fe}(\text{CN})_6]$ was added with a final concentration of 2 mM and p-benzoquinone with a final concentration of 200 μ M. The calibration of the

electrode was done by using air-saturated and nitrogen saturated water at atmospheric pressure.

2.2.9 Mass spectrometry

Matrix-assisted laser desorption/ionization time-of-flight mass spectrometry (MALDI-TOF MS) was performed with an Ultraflex II Spectrometer (Bruker Daltonics, Bremen, Germany) equipped with a 200 Hz solid-state Smart beamTM laser. The mass spectrometer was operated in the positive linear mode to analyze the PSII subunit composition in the range of m/z 3,000-30,000. Data were analyzed using FlexAnalysis® software provided with the instrument. For sample preparation 2 μ l of PSII solution and redissolved crystals (1-4 mM Chla) were diluted 1:10 or 1:30 with 33 % (v/v) acetonitrile and 0.1 % trifluoroacetic acid. Each sample was mixed 1:1 with a saturated solution of sinapinic acid dissolved in 33 % (v/v) acetonitrile and 0.1 % trifluoroacetic acid resulting in a PSII sample containing ca 140 pmol Chla and 1 μ l was spotted onto a stainless steel target using the dried-droplet technique. MALDI-TOF MS measurements were performed by Dr. Chris Weise (FU Berlin).

2.2.10 Blue native polyacrylamide gel electrophoresis

In order to determine the oligomerization state or impurities of proteins solutions Blue native polyacrylamide gel electrophoresis (BN-PAGE) was performed. 4-13 % acrylamide gradient gels cover the range from 10 kDa to 3 MDa (dimeric PSII 0.75 MDa, monomeric PSII 0.35 MDa, ATP synthase 0.5 MDa). All solutions were prepared with autoclaved Millipore distilled water. Chemicals for the acrylamide gel were obtained from Roth. BN-PAGE was performed in an electrophoresis chamber (LKB, Bromma) which was precooled with water to 4 °C using a thermostat. The separation gel (14 x 14 cm) was handmade using a 5 % acrylamide solution and a 12 % acrylamide solution for the gradient part and a sample gel at 3.5 % polyacrylamide solution for the sample part of the gel using the protocol of (136). To avoid protein aggregation during electrophoresis samples were adjusted to a low ionic strength with buffer Cb0. For separation samples were mixed in a 1:3 ratio to 50 μ l volume (0.2 mM, 12.5 μ l protein sample) using a solubilization buffer (50 mM NaCl, 50 mM

Imidazol, 1 mM EDTA, 2 mM ϵ -Amino-n-capronsäure; pH 7.0) and at the same time adjusted to a Chl *a* concentration of 0.06 mM. Samples were then mixed with 5 μ l glycerol (50 % (w/w)) and prior to application in the gel pockets mixed with 1.25 μ l Coomassie G-250 (5 % (v/v) in 750 mM ϵ -aminocaproic acid). Protein standards have been treated the same way as the samples. The run was started with a voltage of \sim 100 V. After the samples passed the stacking gel (the upper loading part with 3.5 % polyacrylamide concentration) the current was set to 15 mA. After the dye front has reached one third of the gel, the cathode buffer B was exchanged with a lower concentrated cathode buffer B/10. After the run was ended the gel was destained with 10 % acetic acid and photographed.

2.2.11 High pressure freezing

PSII crystals were drawn into thin walled polyimide tubes and high pressure frozen at 210 MPa and 77 K using a Baltec HPM 010 instrument (137), (138). Polyimide tubes (GoodFellow GmbH, catalogue No. IM307014 and IM307015) had an inner diameter (ID) of 0.155 mm, outer diameter (OD) of 0.193 mm with a wall thickness of 0.019 mm and an ID of 0.166 mm, OD of 0.196 mm with a wall thickness of 0.015 mm, respectively. Sample handling after high pressure freezing (HPF) was carried out at cryogenic temperatures below 140 K and under green light. The polyimide tubes with the PSII crystals inside in their frozen growth solution were mounted on hollow steel pins (Dispomed Witt oHG, catalogue No. 10092) with an OD of 0.6 mm using home built polyimide clamps. HPF was conducted by Dr. Anja Burkhardt and Dr. Martin Warmer (DESY, Hamburg).

2.2.12 X-ray diffraction data collection

SR XRD measurements were carried out at beamlines 14.1, 14.2 and 14.3 operated by the Joint Berlin MX-Laboratory and the Helmholtz-Zentrum Berlin (HZB) (139) at the BESSY II electron storage ring, Berlin-Adlershof, Germany. Beamline 14.3 equipped with a humidity controller device HC1b (140), allowing RT-measurements at controlled dehydration levels. Beamline 14.2 was equipped with a cryostream and Rayonix 225 mm CCD detector. Beamline 14.1 was equipped with an automated

robot sample delivery system and a Pilatus detector (139). The final dataset of dPSIIcc with 2.44 Å resolution was collected at the Deutsches Elektronen Synchrotron (DESY) at Petra III, beamline P11 equipped with a Pilatus 6 M detector (Dectris, Baden, Switzerland). The dataset was collected from a dPSIIcc crystal with 250 x 100 x 100 μm^3 size using a 100 μm diameter beam with a total dose of 2.8×10^{14} photons (3.6×10^{10} photons per \AA^2) at 10.37 keV photon energy (1.19 Å). Data were integrated and scaled to 2.44 Å maximum resolution with XDS (141). The structure was solved with molecular replacement using Phaser (142) taking two separate PSII monomers of the 1.9 Å resolution structure, PDB code 3ARC (25), as search model. Fitting of the model to the density was done using iterative cycles of hand building in COOT (143) and an automated refinement in phenix.refine (144). The protein model quality was confirmed with MolProbity (145). 96 percent of backbone torsion angles were in favoured regions of the Ramachandran plot. The position and presence of each ligand was confirmed by generating an omit map after three macrocycles of refinement in phenix.refine in absence from the model. Restraints for Chl_a and Pheo were automatically generated by the Grade server v1.001 (Global Phasing Ltd, Cambridge, UK). Heme geometry was taken from the atomic resolution structure in the PDB 3FMU and restraints generated in eLBOW (146). The cytochrome c-550 (PsbV) heme was modeled as covalently bound to Cys 37 and Cys 40 of the subunit. Geometry of the WOC was taken from the highest resolution structure of dPSIIcc PDB 3ARC and restraints generated in eLBOW. All other ligand restraints were taken from the CCP4 (147) monomer library. Data processing and model building of the obtained data sets was done by Dr. Martin Bommer in the group of Prof. H. Dobbek (HU Berlin, Germany).

2.2.13 Critical Micelle Concentration measurements

The effect of PEG 5000 MME on the micelle formation of C₁₂E₈ and β DM was exploited by measuring the fluorescence enhancement of the dye 8-anilino-naphthalene-1-sulfonate (ANS) as described in ref (148). Measurements were conducted using a Horiba Jobin Yvon FluoroMax-2 spectrometer. Measurements were conducted by D.DiFiore in cooperation with Frank Müh (Johannes Kepler Universität Linz).

2.2.14 XFEL diffraction data collection and processing

Fs X-ray diffraction measurements were carried out at the Coherent X-ray Imaging (CXI) chamber at the LCLS at SLAC National Accelerator Laboratory (Stanford, CA, USA). The CXI instrument was operated at energies of 7-9 keV and pulse duration of < 50 fs with a frequency of 120 Hz and an average intensity of $3-6 \times 10^{11}$ photons/pulse. The dose varied between $50-300 \times 10^6$ Gy. Beam focusing to 1.5 μm FWHM at the interaction region was accomplished using Kirkpatrick-Beaz mirrors (149). Diffraction was measured using the Cornell-SLAC pixel array detector of the CXI endstation (150) providing a pixel size of $110 \times 110 \mu\text{m}^2$ with a total of 2.3 million pixels. The program RADDPOSE (151) was used to convert the flux numbers into the deposited energy dose. Diffraction data were processed using a new software suite (cctbx.xfel) built on Bragg spot picking (spotfinder) and autoindexing (labelit) (152, 153) and uses pixel summation methods for the integration of Bragg spot intensities (154). The PSII structures were solved by the molecular replacement method using Phaser (155), taking the 2.9 Å resolution structure as a search model (23) (PDB codes 3BZ1, 3BZ2) including ligands, but excluding the Mn_4CaO_5 cluster. Refinement of the data was performed with phenix.refine (144, 156, 157). Truncated electron density maps of PSII SR data (PDB code 3BZ1) were generated the same way as LCLS data but without B-factor sharpening. Data processing and model building of the obtained data sets as well as software development was done by Marc Messerschmidt (SLAC National Accelerator Laboratory), J. Hattne, Nathaniel Echols, Richard J. Gildea, Ralf W. Grosse-Kunstleve, Petrus H. Zwart, Paul D. Adams and Nicholas K. Sauter (Lawrence Berkeley National Laboratory).

2.2.15 X-ray emission spectroscopy

Theoretical background

XES is a powerful method to study the local chemistry in metalloproteins and can be used to identify the charge state of metal ions of the WOC. It explores the occupied electron levels and provides information about the electronic structure, charge and spin densities, and the nature of ligands. The basic event that occurs during XES (Figure 2-1) is that absorption of photons of an incident X-ray beam excite 1s core

electrons (K shell) of a molecule and ejects them into the continuum. The generated electron hole is instantly refilled by a higher energy level electron. The energy difference between the two energy levels is released in form of emission of X-rays. The valence band electron to 1s transitions provide the $K\beta_{2,5}$ and $K\beta''$ emission spectra, the refilling of the 1s core holes by 3p electrons provides the $K\beta_{1,3}$ and $K\beta'$ spectra and the 2p to 1s transitions provide the $K\alpha_1$ and $K\alpha_2$ emission spectra (Figure 2-2). The spectral shape in the $K\beta_{2,5}$ region is sensitive to the protonation of ligands and allows distinguishing between ligands that differ only slightly in atomic number, for example C, N and O. In the later presented studies the $K\beta_{1,3}$ and $K\beta'$ lines result from the number of unpaired 3d electrons and provide oxidation and spin state information. The $K\beta_{2,5}$ and $K\beta''$ lines probe 2s/2p ligand to 1s metal cross-over transitions and generate information about the ligand environment. Manganese model systems as Mn(II)O, Mn(IV)O₂ and Mn₂(III,IV)terpyridine with respective oxidation states of interest provide information about the energy shifts and corresponding oxidation states of Mn. A shift to higher energies in the $K\beta_{1,3}$ spectra corresponds to a reduced state of Mn in Mn₄CaO₅-cluster .

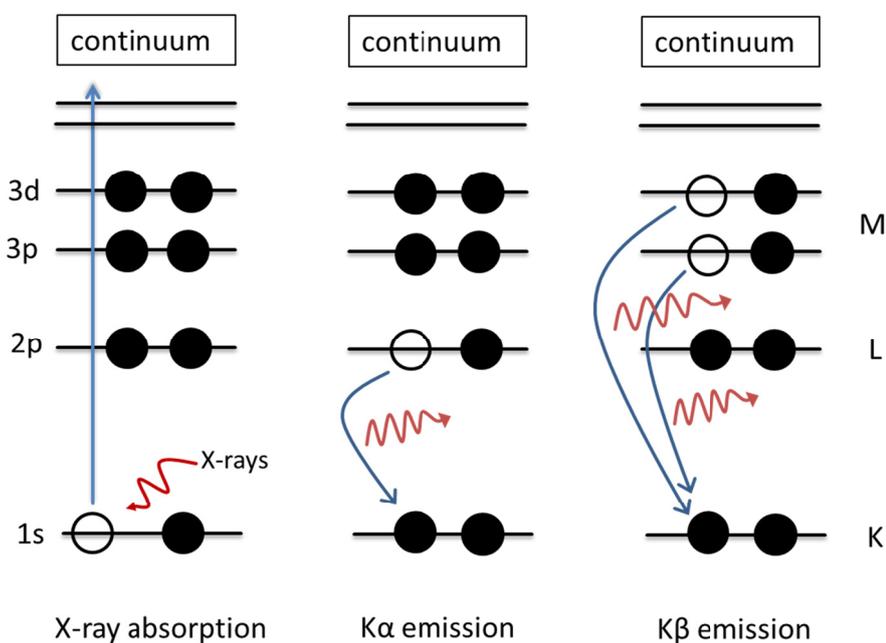


Figure 2-1 Schematic illustration of X-ray emission events

This simplified scheme shows on the left side the X-ray absorption by a 1s core electron of the K shell which is ejected into the continuum. The refilling of the electron hole by an L-shell electron produces K α X-ray emission, the refilling by an M-shell electron produces K β X-ray emission.

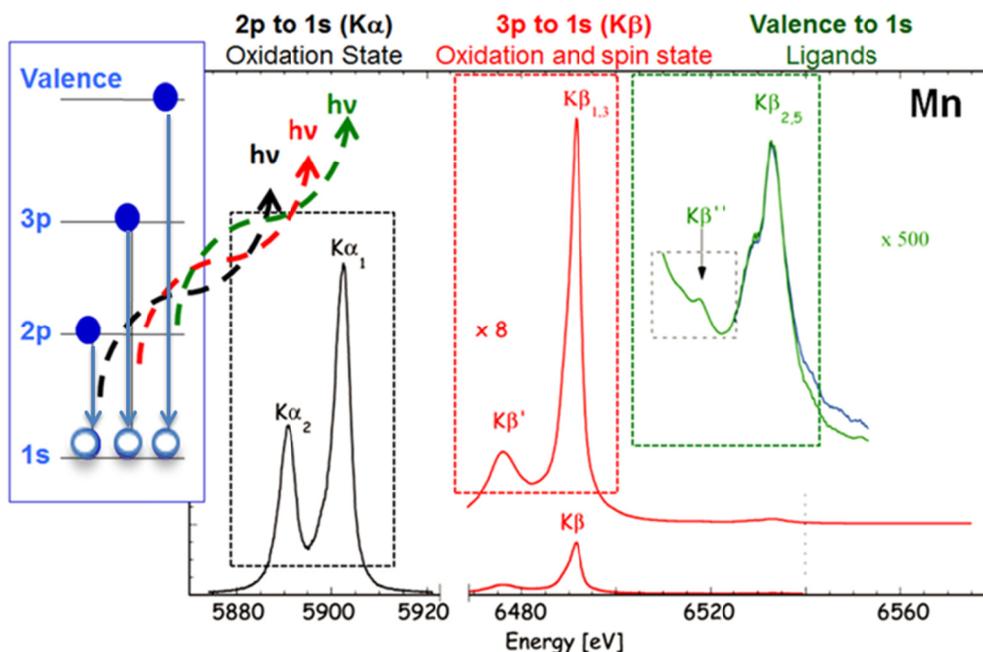


Figure 2-2 X-ray emission spectra of manganese

Left side) Scheme of electron transitions of occupied electron states (a valence state electron, a 3p electron or a 2p electron) refilling a 1s electron hole. Right side) Respective energy differences ($h\nu$) are emitted in form of X-rays. The corresponding intensities and energies for manganese are presented in the emission spectra. Figure provided by Dr. Jan Kern.

2.2.16 XES / XFEL diffraction data collection and processing

Fs XES data were simultaneously measured with fs XRD data, at CXI, LCLS. XES data were recorded at excitation energy of 7 keV, which is close to the Mn-edge of 6.54 keV. XRD was measured at 7 keV and at 9.5 keV excitation energies. The images used for the S_1 and S_2 data sets were mostly collected at 9.5 keV. The custom-built energy-dispersive XES spectrometer, based on the von Hamos geometry (158), was used to obtain high resolution data in a shot-by-shot mode. The crystal analyzer array was at a distance of 500 mm away from the interaction point. The spectrometer is composed of an array of 16 cylindrically bent Si-440 crystal analyzers at a Bragg angle range equivalent to 6474.6-6499.4 eV. The signals were recorded at a Cornell-SLAC Pixel Array Detector located below the interaction region. The setup was calibrated using $Mn^{II}Cl_2$ and Mn^{III} terpyridine. This calibration allowed for the direct comparison of CXI and SR data.

For data processing the PSII S₁ X-ray emission crystal spectra were initially screened for crystalline diffraction. 19,260 XES detector images had a high probability of simultaneous XRD. For the S₂ crystal spectrum the diffraction images were manually inspected for Bragg spots yielding a total of 362 crystal hits at incident energy of 7 keV. Only the XES detector images for the 362 crystal hits were included in the S₂ spectrum. For the S₁ PSII solution spectrum all 375,848 images were included in the processing, which is equivalent to ca 52 min of data collection at 120 Hz. The images were all initially treated with dark current subtraction and corrected for common mode offset. Single-pixel histograms were constructed for the recorded pixels and Gaussian curves were fitted to the zero and one photon peaks of the histograms. This enabled dark and gain corrections and centering of the zero photon peaks at zero analog-to-digital units. The final 1D spectra were obtained by integrating the signal in the non-dispersive direction. The average sample volume that was probed by the X-ray beam was estimated to be 17 μm³. This results in a total volume of 0.3 nl for the S₁ single crystal spectrum probed by the X-rays (ca 20,000 shots). The Mn concentration in the PSII crystals is ca 7 mM, thus the total amount of Mn for this spectrum is ca 2 x 10⁻¹² mol. The corresponding values for the amount of Mn in the S₁ “indexed crystals” and the S₂ single crystal spectra are ca 1.4 x 10⁻¹³ and ca 4 x 10⁻¹⁴ mol, respectively. For the PSII solution with a Mn concentration of 1 mM the spectrum was obtained from ca 375,000 individual shots which is equivalent to a Mn amount of ca 6.3 x 10⁻¹² mol. Design and tests of the XES spectrometer setup were done by Roberto Alonso-Mori (SLAC National Accelerator Laboratory), Jan Kern, Rosalie Tran, Benedikt Lassalle-Kaiser, Sheraz Gul and Junko Yano (Lawrence Berkeley National Laboratory), Tsu-Chien Weng and Dimosthenis Sokaras (SSRL, SLAC National Accelerator Laboratory).

3 Purification and crystallization of dPSIIcc using C₁₂E₈

Introduction

A wide variety of detergent molecules is available today and is frequently used for membrane protein solubilization and crystallization (116, 117). Almost exclusively used for purification and crystallization of PSII is the mild, non-ionic detergent β DM. This detergent has a maltoside-headgroup, which is structurally similar to DGDG with a digalactosyl-headgroup, an endogenous lipid of PSII (Figure 3-1 A and B). The lipid has a diacylglycerol tail, β DM has one hydrophobic alkyl chain. The detergent β DM is incorporated into the dPSIIcc structure during the purification procedure of the protein. In the dPSIIcc crystal structure at 2.9 Å resolution (23) which was solely purified and crystallized with β DM, 7 detergent molecules per monomer have been found. In the 1.9 Å resolution structure of dPSIIcc 7 β DM and additional 8 HTG molecules have been found per monomer. The detergent molecules are mostly found at the monomer-monomer interface of PSII where they established ionic interactions with surrounding amino acids. There the detergent molecules lead to a modification of the native state and might induce a structural destabilization of the protein and the dimeric form. Discussions are ongoing, whether the PSII dimer/monomer ratio is influenced by the use of the detergent β DM and high concentrations induce the dimeric form of PSII (30). Whether the abstraction of lipids from monomeric PSII results in dimerization (31), or if the dimerization is only induced by the use of high concentrations of β DM (> 1 %) as postulated by Pagliano et al. for plant PSII (*Pisum sativum*) (27). In the cyanobacterial 2.9 Å resolution structure of dPSIIcc (23), 25 integral lipid molecules per PSIIcc monomer were reported. These lipids have important roles in the PSII structure and the functioning of the protein and are termed new cofactors (78, 159), (Chapter 1.3.6 Integral lipids, page 23). In order to stabilize the native dPSIIcc and to find out if more lipids can be retained in the structure when using a structurally different detergent, this study was started. Several detergent molecules have already been tested for PSII extraction yield and activity. First tests with octaethyleneglycolmonododecylether (C₁₂E₈) showed high PSII oxygen evolution activity after extraction from the thylakoid membrane and the extraction yield was comparable to that of β DM. These results and the difference of the overall

structure of $C_{12}E_8$ (Figure 3-1 C) as compared to native lipid molecules made it a suitable molecule for further studies.

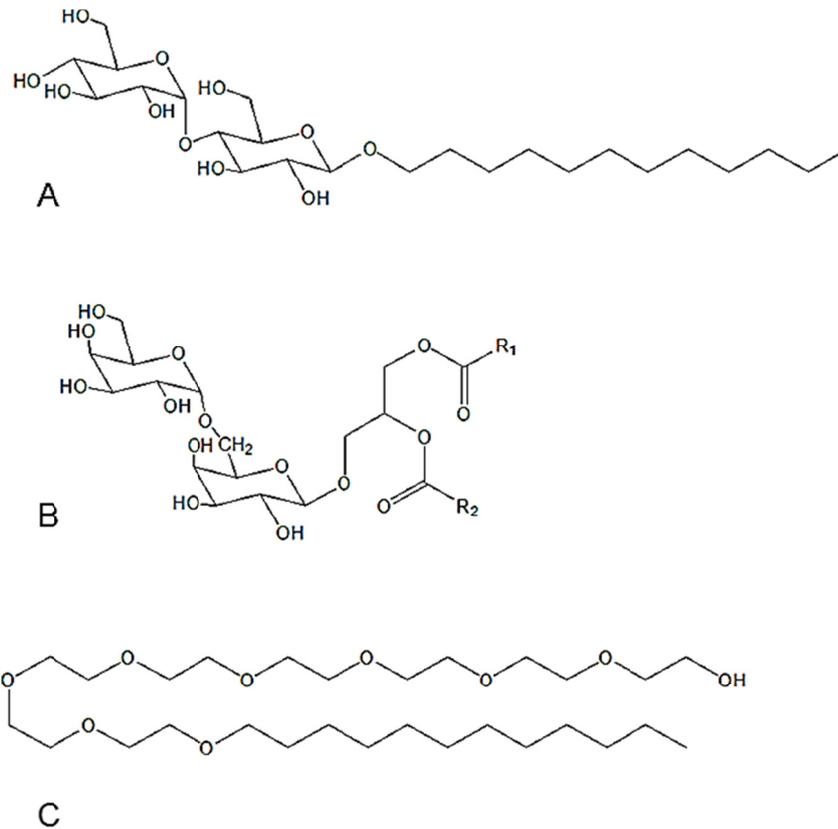


Figure 3-1 Structural comparison of detergent molecules and a PSII lipid

A) detergent *n*-Dodecyl- β -D-maltoside (β DM), B) integral lipid Digalactosyldiacylglycerol (DGDG), R_1 and R_2 represent fatty acid chains, C) detergent Octaethyleneglycolmonododecylether ($C_{12}E_8$)

3.1 Purification procedure for PSIIcc with $C_{12}E_8$

To obtain PSII protein material, cyanobacteria of the thermophilic strain *T. elongatus* have been cultivated in a photobioreactor as described before (120). The extraction as described when using the detergent β DM and all subsequent steps had to be changed and adapted to the detergent $C_{12}E_8$. Thylakoid protein extraction with 1-1.2 % (w/w) $C_{12}E_8$ and 5 min incubation time resulted all in a similar Chla extraction yield of ca 200-600 μ M Chla. Longer incubation times did not give better results for $C_{12}E_8$ (this is in accordance with β DM extractions). Subsequent thylakoid membrane

extractions have been performed with 1.2 % (w/w) C₁₂E₈ and 5 min incubation time. For the chromatographic purification of dPSIIcc with the detergent β DM a successful protocol is known (120). Based on this knowledge it was possible to establish a purification protocol for PSII with the detergent C₁₂E₈. First experiments were carried out to yield PSII in the same way as the known protocol, but this did not result in the same defined peak separation. A newly established purification procedure included two anion exchange columns and one stronger quaternary amino (MonoQ) anion exchange column. The first column (Figure 3-2), using Toyopearl DEAE (diethylaminoethyl) 650 S as a matrix, separates the large amount of phycobiliproteins, and PSI from crude PSII. Subsequently, PSII fractions have been further purified with a second Toyopearl DEAE 650 S matrix column (Figure 3-3) to result in a separation of residual amounts of phycobiliproteins and residual monomeric PSI and ATP synthase from the dPSIIcc peak. The ATP synthase was detected with MALDI-MS (Figure 3-6) and is one of the impurities that can prevent dPSIIcc from crystallizing. This contamination was absent after the second purification steps in most cases, but due to variations of the protein extracts the ATP synthase was retained after the second column in some cases. Alternatively, a stronger anion exchange material (prepacked MonoQ column) has been chosen for a third purification step (Figure 3-4), which resulted in a separation of the ATP synthase as checked with MALDI-MS (Figure 3-8). For all separation procedures no mPSII peak was detected. For the β DM purification protocol, PSII was obtained in almost equal amounts of mPSII and dPSII with a ratio of (0.7 ± 0.3) (120). This leads to the assumption that only minor amounts of mPSII are obtained when using the detergent C₁₂E₈ and thus the dPSIIcc complexes are stabilized by the use of the detergent C₁₂E₈.

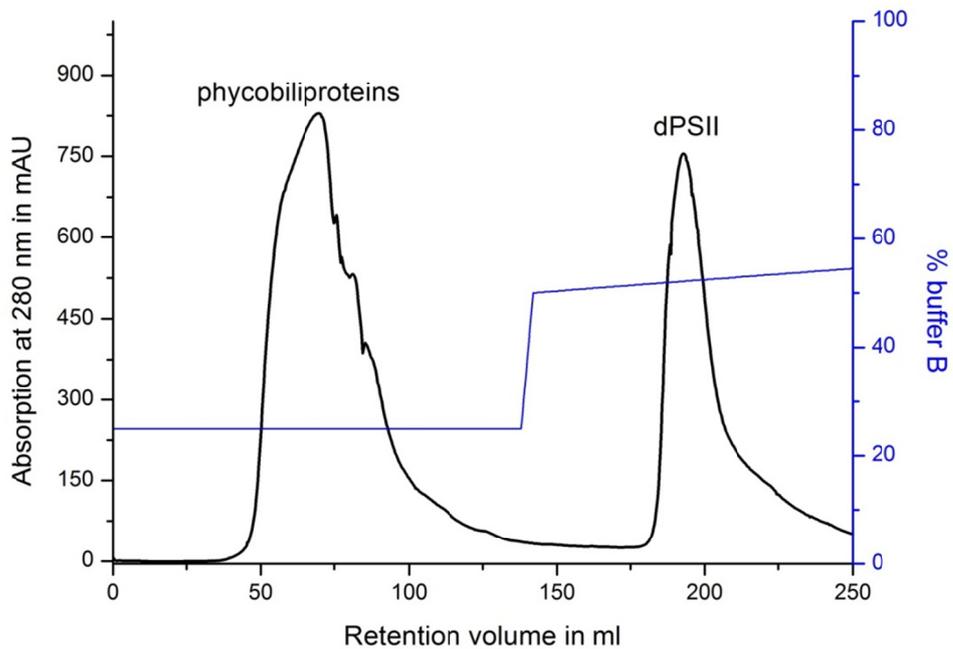


Figure 3-2 First anion exchange column

First Toyopearl Sepharose DEAE column showing that PSII elutes in a single peak. Contaminants as phycobiliproteins and a large fraction of PSI (elutes after PSII and is not shown here) are separated.

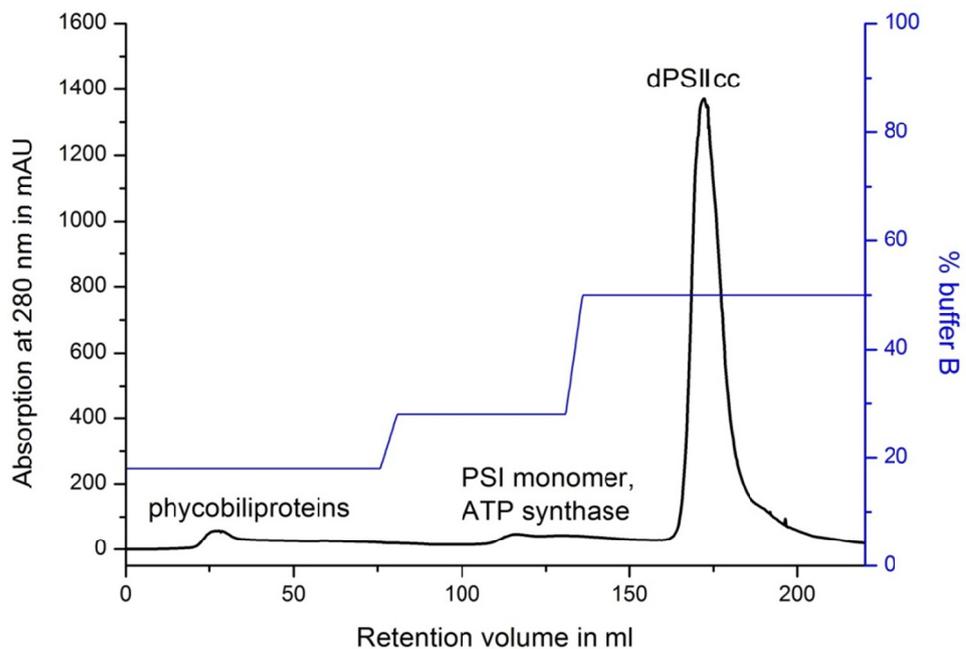


Figure 3-3 Second anion exchange column

Second purification step with a Toyopearl Sepharose DEAE column, obtaining the PSIIcc (no splitting into mPSIIcc and dPSIIcc was obtained). The small peaks ahead of the PSIIcc represent residual phycobiliproteins, ATP synthase and PSI monomer.

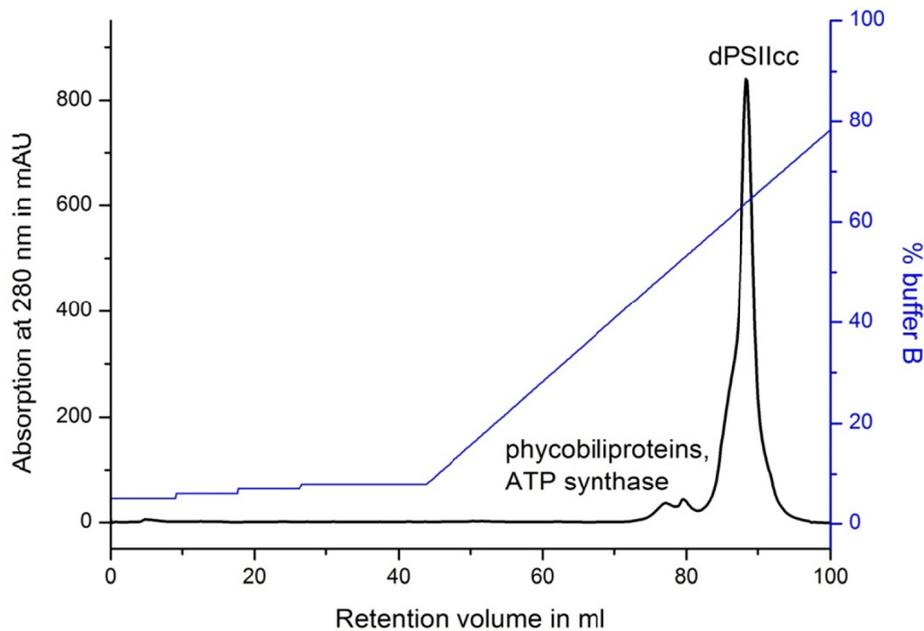


Figure 3-4 Third strong anion exchange column

Third purification with a stronger anion exchange column, resulting in separation from minor impurities as phycobilisomes and ATP synthase.

3.2 Characterization of dPSIIcc

3.2.1 Oxygen evolution activity

To examine the oxygen evolution capacity of PSII samples, oxygen evolution measurements per single flash were performed at different steps of the PSII purification protocol. The results provide information about the purity and the activity of the PSII samples. The obtained number of Chla ($\frac{1}{4} \text{O}_2 \times \text{flash}^{-1}$), has to be corrected due to various factors, like double hits (two photons are absorbed by the same photochemical center) and misses (charge separation, but no S-state transition) (160). Further instrumentation errors during calibration and concentration determination of the sample add up to an error of about 15 % for this method. The activity of the PSII samples was measured before the chromatographic purification using the crude extract, after each chromatographic step and of dissolved PSII crystals (Table 3-1). The oxygen evolution activity of the crude extract before chromatographic purification was in the range of 59-140 Chla ($\frac{1}{4} \text{O}_2 \times \text{flash}^{-1}$). The

value stepwise improved after the first chromatography column to 38-44 Chla ($\frac{1}{4}$ O₂ x flash)⁻¹, 31-45 Chla ($\frac{1}{4}$ O₂ x flash)⁻¹ after the second and 28-31 Chla ($\frac{1}{4}$ O₂ x flash)⁻¹ after the third column. Dissolved crystals show a value of 49 Chla ($\frac{1}{4}$ O₂ x flash)⁻¹. This higher value as compared to purified PSII solution is considered to be either the result of measurements with PSII crystals that have been longer stored at RT, which can significantly reduce the activity, or the preparation dependent variability of PSII samples. All values of purified material are indeed in good match with the theoretical value of 35 Chla ($\frac{1}{4}$ O₂ x flash)⁻¹ when the 15 % error is considered. For values that are below the theoretical value of 35 Chls/RC a higher error of up to 25 % has to be accounted for.

Sample	Single flash Chla ($\frac{1}{4}$ O₂ flash)⁻¹
Crude extract	59 – 140
dPSIIcc after 1. chromatography	38 – 44
dPSIIcc after 2. chromatography	31 – 45
dPSIIcc after 3. chromatography	28 – 31
dissolved dPSIIcc crystals	49

Table 3-1 Table Oxygen evolution activity of PSII samples

Oxygen evolution activity obtained after single flash excitation, given as the number Chla ($\frac{1}{4}$ O₂ flash)⁻¹ of dPSIIcc at different steps of the purification procedure and from dissolved dPSIIcc crystals. (For each purification step the range of 10 independent measurements and the value for a small amount of dissolved crystals is presented).

3.2.2 Size exclusion chromatography

Information about the oligomerization state of a PSII sample can be obtained by size exclusion chromatography. Samples of dPSc (750 kDa) and mPSIIcc (350 kDa) (161), as purified according to the protocols in references (120) and (24), were used

as standards. The retention volume was determined to be 13.04 ml for the dPSIIcc and 14.39 ml for the mPSIIcc standard solution. The PSII fraction that has been obtained after the third chromatographic purification step with a DEAE MonoQ column was used here and resulted in a retention volume of 13.10 ml. This result is consistent with the retention time of the dPSII standard and allows an assignment to the dPSIIcc. The size exclusion chromatograms that have been run on a superose 6 column are shown in Figure 3-5 A.

3.2.3 Blue Native polyacrylamide gel electrophoresis

For further investigation of the purity and the oligomerization state of the protein samples, blue native polyacrylamide gel electrophoresis (BN-PAGE) was performed. This method retains the native state of the protein complex and does not split it into its subunits. In this way a determination between mPSIIcc and dPSIIcc and impurities of the samples can be made. The BN-PAGE of PSIIcc after purification as compared to mPSIIcc and dPSIIcc standards is presented in Figure 3-5 B. The C₁₂E₈-PSIIcc lane shows a dominant band of dPSIIcc as compared to the dPSIIc standard. A faint band in the height of the mPSIIcc standard band can be seen. This might be a slight contamination of dPSIIcc fraction with mPSIIcc retained after purification or may also be induced by the BN-PAGE system.

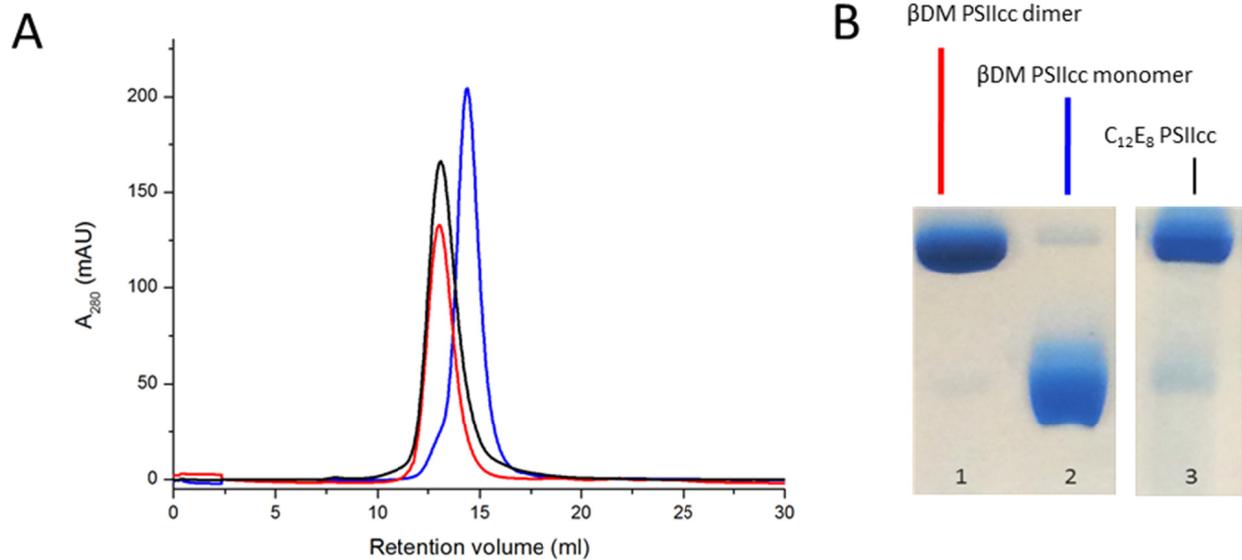


Figure 3-5 Size exclusion chromatography and BN-PAGE of β DM-PSIIcc standards and PSII samples

A) Size exclusion chromatography of PSII standards and PSII samples. The retention volume for standards of dPSIIcc is 13.04 ml (red) and for mPSIIcc 14.39 ml (blue). The C₁₂E₈-PSIIcc sample shows a retention volume of 13.10 ml and can be assigned to dPSIIcc. B) The BN-PAGE comparing β DM-dPSIIcc (red), β DM mPSIIcc (blue) with C₁₂E₈-PSIIcc.

3.2.4 Mass Spectrometry

The protein subunit composition and purity was investigated with Matrix-assisted laser desorption/ionization time-of-flight mass spectrometry (MALDI-MS). For the low molecular weight subunits (< 30 kDa) the precision of the mass determination together with the available sequence data allows the assignment of protein subunits present in the sample. For larger protein subunits (> 30 kDa) the accuracy is no longer given, due to unfavorable flight behavior in the time-of-flight analyzer and only broad peaks are obtained that can no longer be clearly assigned. Further the purity of the protein sample can be monitored. One contamination of PSII samples is the ATP-synthase, which shows a prominent peak at 8235 Da (subunit c of the ATP-synthase) (162). For all measurements a dPSIIcc sample purified with β DM was used as a standard and comparison (Figure 3-6). MALDI-MS spectra of dPSIIcc solution after the first chromatographic step (Figure 3-7), after the third chromatographic purification step (Figure 3-8) and after crystallization (Figure 3-9) are shown. All samples show an identical MALDI-MS subunit spectrum, thus they have an identical

subunit composition. Differences of peak intensities are caused by small variations of the crystallization quality of the sinalpinic acid matrix, which influences the ionization of the proteins. Note that the intensities are given in arbitrary units, which is no physical variable, so they strongly depend on measurement parameters, like detector sensitivity. In this way comparable intensity scales do not relate to comparable concentrations of the measured samples and are only a qualitative analysis. Masses for the subunits PsbE, PsbF, PsbH, PsbI, PsbJ, PsbK, PsbL, PsbM, PsbO, PsbT, PsbU, PsbV, PsbX, PsbY, PsbZ and ycf12 were detected in all samples. The masses of the larger protein subunits D1, D2, CP43 and CP47 could not be determined due to their unfavorable flight behavior. The mass peak of the subunit c from ATP-synthase was detected in dPSIIcc samples after the first purification step. After the third chromatographic purification step the ATP-synthase was no longer found. The MS spectrum of dissolved dPSIIcc crystals presents the completeness of the subunit composition and the absence of contamination with the c-subunit of the ATP-synthase. A table of the calculated and experimentally determined masses of the small subunits is summarized in Table 3-2.

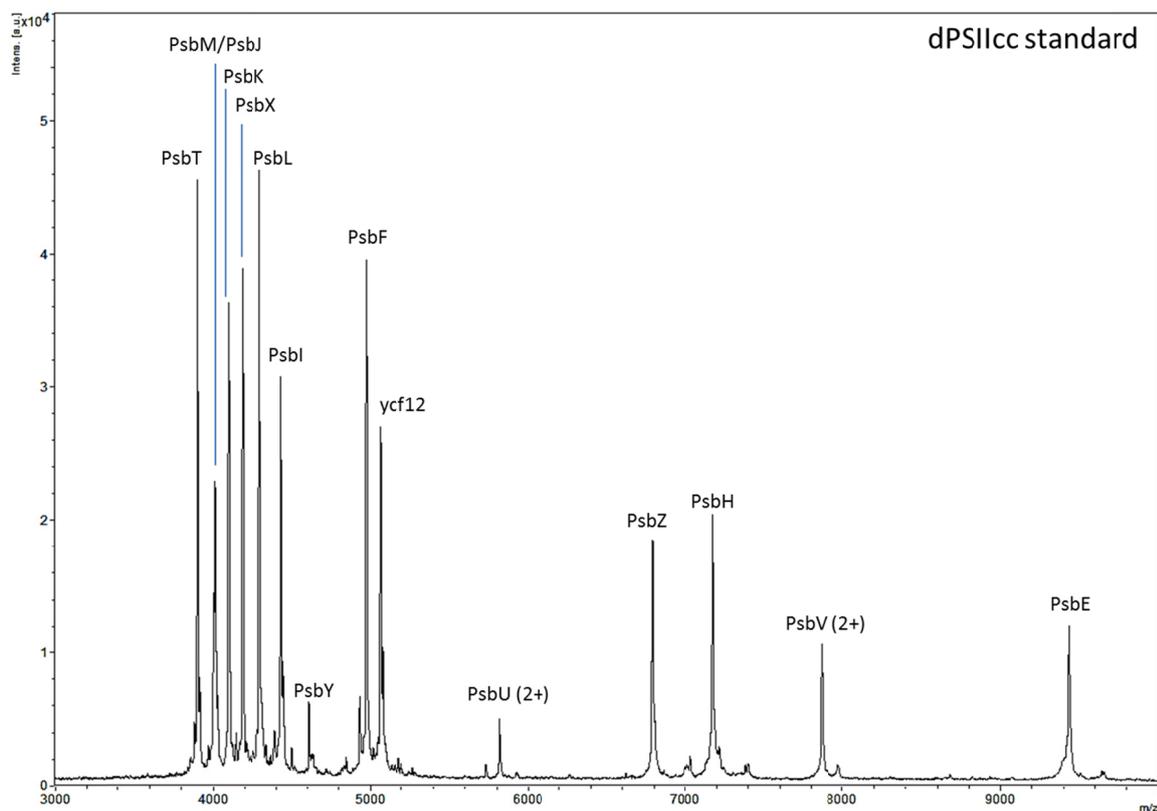


Figure 3-6 MALDI-MS spectra of standard dPSIIcc

Mass spectra obtained from β DM-dPSIIcc solution showing the PSII subunits in the m/z range of 3000-10000 as labelled.

Purification and crystallization of dPSIIcc using C₁₂E₈

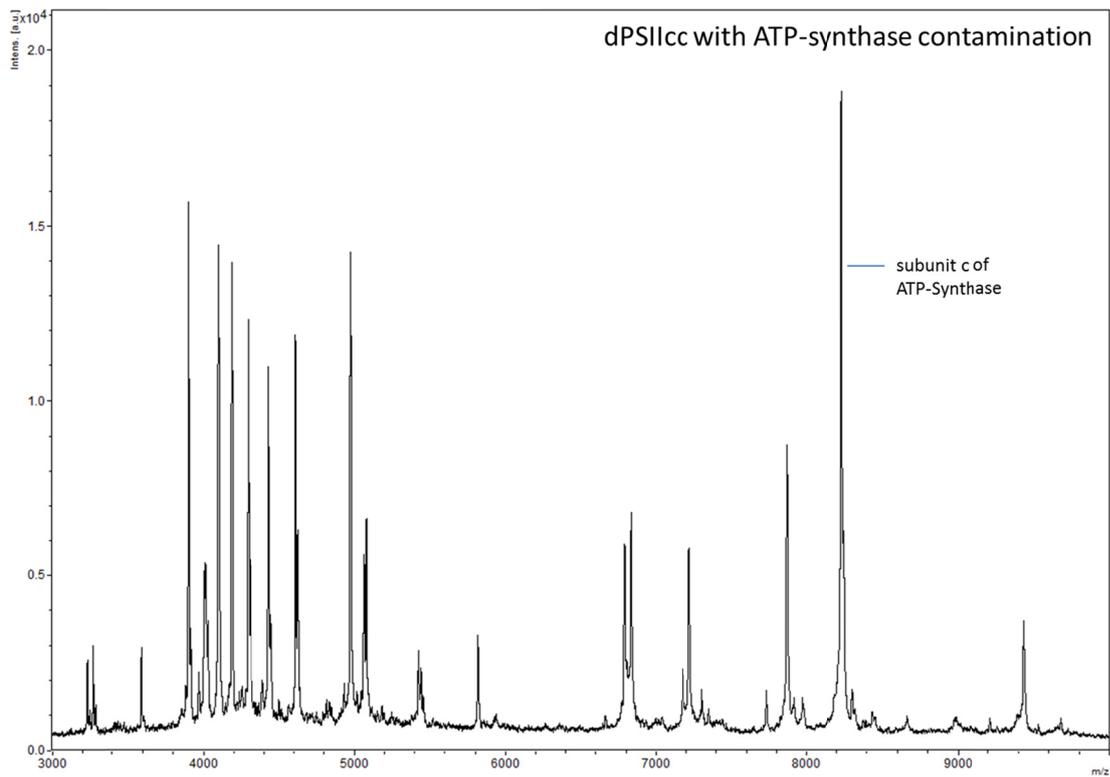


Figure 3-7 MALDI-MS spectra of dPSIIcc with ATP-Synthase contamination

Mass spectra obtained from C₁₂E₈-dPSIIcc after the first chromatographic purification step. Contamination of PSII solution with subunit c of the ATP-Synthase can be seen at 8235 m/z as labelled.

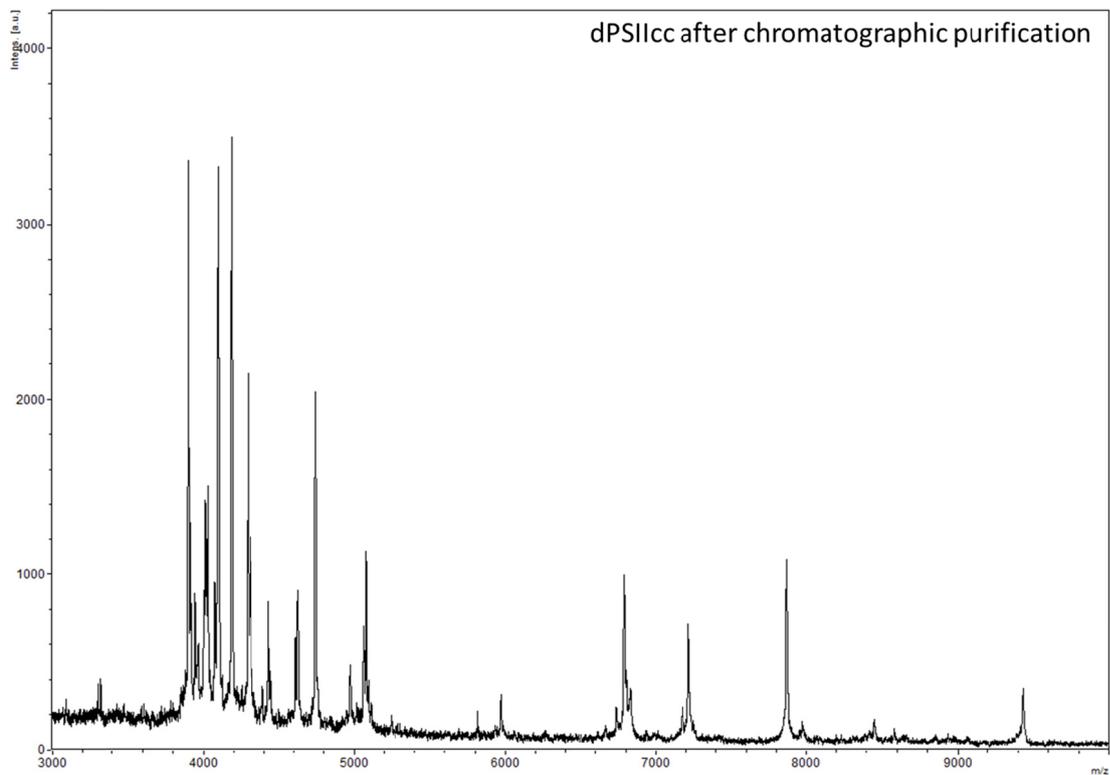


Figure 3-8 MALDI-MS spectra of dPSIIcc after chromatographic purification

Mass spectra of C₁₂E₈-dPSIIcc solution after the third purification step using a strong anion exchange column. The ATP-synthase peak at 8235 m/z is not found.

Purification and crystallization of dPSIIcc using C₁₂E₈

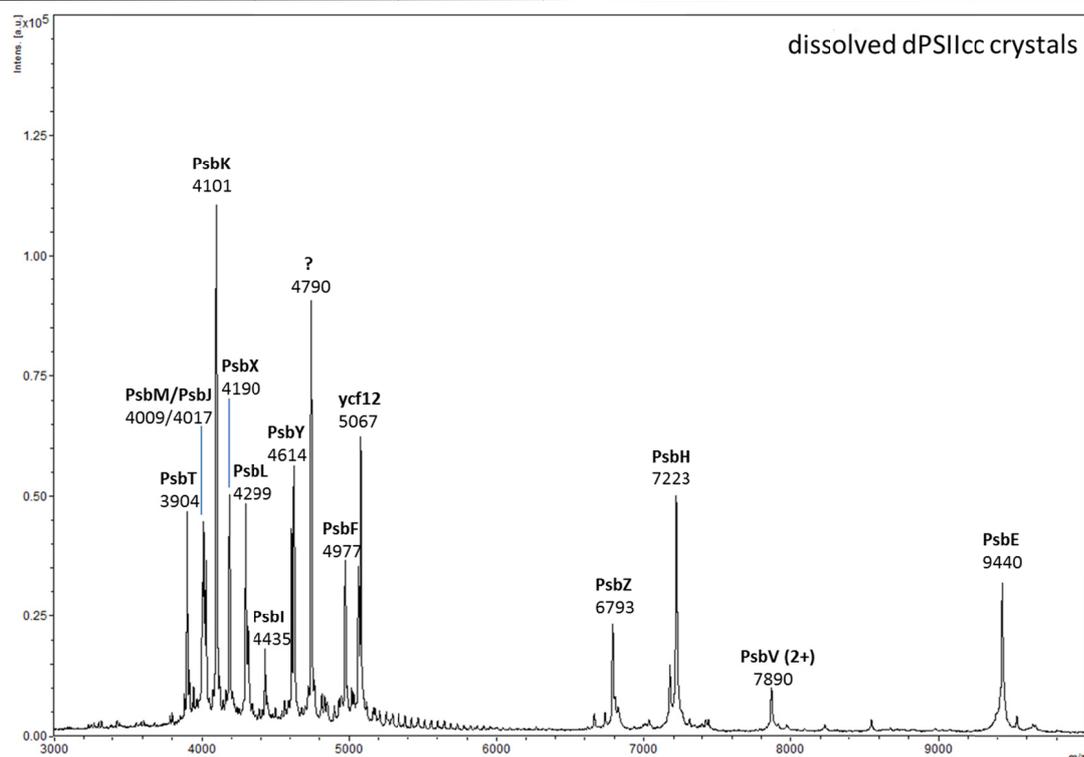


Figure 3-9 MALDI-MS spectra of dPSIIcc crystals

Mass spectra of dissolved C₁₂E₈-dPSIIcc crystals showing the PSII subunits in the m/z range of 3000-10000 as labelled.

Subunit	cyanobase gene number	calculated masses unprocessed form [M+H] ⁺ in Da	experimental determined mass in m/z [M+H] ⁺ ± σ
PsbT	tsr1531	3875.8	3906±4
PsbM	tsl2052	3980.7	4011±2
PsbJ	tsr1544	4105.9	4017±2
PsbK	tsl0176	5027.1	4103±4
PsbX	tsr2013	5233.4	4192±4
PsbL	tsr1543	4298.1	4301±4
PsbI	tsr1074	4406.3	4437±4
PsbY	tsl0836	4773.9	4617±4
PsbF	tsr1542	5066	4981±5
ycf12	tsr1242	5038.2	5068±2
PsbZ	tsr1967	6765.2	6798±5
PsbH	tsl1386	7355	7227±5
PsbE	tsr1541	9573.9	9446±6
PsbV	tll1285	15018	15752±11
PsbU	tll2409	18028	11649±8
PsbO	tll0444	29607.6	26830±30

Table 3-2 MALDI-MS masses of PSIIcc

MALDI-MS masses obtained in the linear mode and assigned to dPSIIcc subunits. The calculated masses are given as average mass for [M+H]⁺ from the sequence of the full length precursor protein.

3.3 Crystallization of dPSIIcc

When purified protein solution of dPSIIcc was obtained, a variety of crystallization screens were tried using different protein preparations and Chla concentrations. The protein was adjusted to an initial Chla concentration of 1 or 2 mM and each crystallization condition had a volume of 0.2 µl dPSIIcc solution using the sitting drop vapor diffusion method in MRC 96 x 2 well plates (Swissci, Neuheim, Switzerland). The screening was done with a crystallization robot (Honeybee, digilab) using the following crystallization screen: ProPlex Screen HT-96, PEG/Ion Screen, Natrix, MembFac (Hampton Research), ProPlex, PACT*premier*TM, JCSG-*plus*, MIDASTM, Structure Screen 1+2, MemGold (Molecular Dimensions), MbClass Suite, MbClassII Suite (Qiagen) and JBScreen Membrane (Jena Bioscience). Screens have been checked immediately after the screening, 1-2 days afterwards and again after one week. The crystallization plates were stored at dark and RT. A great variation of phase separation, drop formation, precipitation and red crystalline formations was obtained initially. Conditions with different salts (0.2 M Na₂HPO₄ or K₂HPO₄) and 20 % (w/v) PEG 3350 led to formation of crystals, but crystals were not well shaped and further optimization did not yield large enough crystals for XRD. Other crystal hits were found for 0.025 M HEPES pH 7.5, 0.2 M NaCl and 0.1 M HEPES pH 7.5, 0.1 M NaCl both with 12 % PEG 4000 as precipitation agent. Variation of the buffer system of the PSII solution was tested for 0.1-0.025 M HEPES pH 7.5, 0.1-0.025 M PIPES pH 7.0, with salts (0.025-0.1 M NaCl or MgCl₂) and variation of PEG 4000 (12-14 % PEG 4000). No fine-tuning of the screening conditions was successful in gaining well shaped crystals with desired dimensions (ca 200-500 µm for longest dimension). As the PSII purification procedure was further optimized, further green crystal hits have been found for the conditions 0.1 M sodium citrate pH 5.5, 15 % PEG 6000 and 0.1 M TRIS pH 7.5, 0.2 M (NH₄)₂SO₄, 20 % PEG 5000 mono methylether (MME) of the ProPlex crystal screen. During optimization of both conditions the second turned out to be most promising while resulting in higher reproducibility and thus extensive fine-tuning was only performed with the latter condition. Exchanging the buffer system to 0.1 M PIPES pH 7 or MES pH 6 did not give better results or hardly any crystals at all. Using NaCl instead of the salt (NH₄)₂SO₄ did neither improve crystal yield nor quality. Finally green crystals with sufficient size (ca 200 - 300 µm for the longest dimension) and trapezoid shape (Figure 3-10) were reproducibly obtained when

using 0.1 M TRIS pH 7.5, 0.1 M (NH₄)₂SO₄, 15-18 % PEG 5000 MME as crystallization agent. Crystals of dPSIIcc were obtained using microbatch 96 well Imp@ct plates (Greiner Bio-one, Frickenhausen, Germany) with dPSIIcc solution of 2 mM Chla in (0.02 M MES pH 6, 0.01 M CaCl₂ and 0.013 % C₁₂E₈) mixed 1:1 with the crystallization agent. Crystals appeared after 1 h – 2 days at RT and grew further in size (max 400 μm) within a few days.

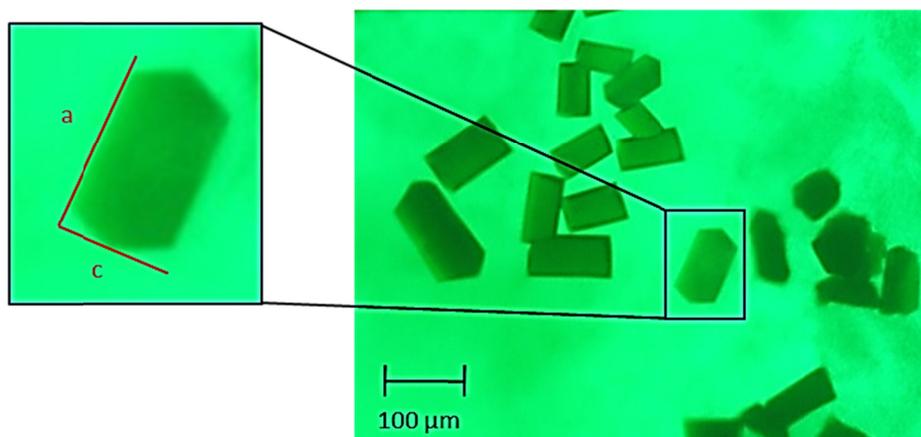


Figure 3-10 dPSIIcc crystals

Light microscopy image of green C₁₂E₈-dPSIIcc crystals under green illumination. The inset shows one crystal to indicate the orientation of the unit cell axes labelled in red.

3.4 SR XRD measurements of dPSIIcc crystals

Diffraction data of dPSIIcc crystals were initially measured with crystals at RT and with high pressure frozen (HPF) crystals. RT XRD data were collected with crystals in their crystallization solution (0.1 M TRIS pH 7.5, 0.1 M (NH₄)₂SO₄, 15-18 % PEG 5000 MME) using the HC1c humidity controller (140) at beamline 14.3 of the BESSY. The crystals yielded diffraction to 6 Å resolution and belonged to the orthorhombic space group P2₁2₁2₁ with unit cell sizes of $a = 141.0 \pm 3.1$ Å, $b = 232.0 \pm 0.9$ Å, $c = 309.9 \pm 5.6$ Å, which is the average and standard deviation of 20 crystals from the same crystal batch. HPF dPSIIcc crystals have been frozen at 210 MPa without cryogenic protection in their crystallization solution and were measured at 100 K (137) at beamline P11 of the DESY. Those crystals diffracted to 6 Å as well and had P2₁2₁2₁ symmetry with unit cell sizes of $a = 140.0 \pm 1.7$ Å, $b = 230.9 \pm 2.4$ Å, $c = 320.3$

± 5.5 Å, which is the average and standard deviation of six crystals of the same batch. The method of HPF was found to be compatible with the C₁₂E₈-dPSIIcc crystals but did not help to improve their resolution and resulted in a XRD dataset of only 8 Å resolution. The variability in the lengths of the axes might occur within one crystal, which could explain the low resolution of all these crystals. Testing of several cryogenic protectives such as 30-35 % sucrose, 30-35 % glycerol and 20-30 % PEG 400 for routine 100 K XRD measurements did not yield better diffraction than 6 Å or gave no diffraction at all. When crystals were transferred to a high concentration of PEG 5000 MME, which was found sufficient to prevent ice formation, the resolution improved dramatically. The stepwise increase (5 % steps, 5-10 min) to a final buffer containing 40-50 % (w/v) PEG 5000 MME in 0.1 M TRIS pH 7.5, 0.1 M (NH₄)₂SO₄ gave routinely 2.5 - 3.5 Å resolution. Beyond this resolution spots were no longer distinguishable and formed streaks extending to at least 2 Å resolution. The P2₁2₁2₁ symmetry was again maintained, but the unit cell dimensions were much smaller than for RT and HPF measured PSII crystals. Unit cell sizes of $a = 116.4 \pm 0.4$ Å, $b = 218.4 \pm 0.9$ Å, $c = 300.7 \pm 2.6$ Å, which is the average and standard deviation of 10 crystals from two batches, were obtained. Thus the unit cell volume was reduced by 25 % compared to RT and HPF crystals. The transfer of the PSII crystals to a high concentration of PEG 5000 MME (PEG treatment) resulted in generally more stable cell lengths compared to the RT/ HPF PSII crystals. The *a*-axis was the most stable with almost no change from crystal to crystal and the *c*-axis was the least stable. Note that streaks in the diffraction pattern images occurred along the *b*-axis. It was questioned why the dramatic improvement was obtained. When this protocol was tested on βDM-dPSIIcc crystals no improvement of diffraction quality was observed. In order to understand this observation, CMC-measurements with C₁₂E₈ and βDM and the possible effect of PEG 5000 MME have been performed (Chapter 3.7 CMC measurements, page 91).

The final data set of a PEG treated C₁₂E₈-dPSIIcc crystal was recorded at DESY with a resolution of 2.44 Å (Table 3-3) (PDB entry 4PJ0). The structure was solved by molecular replacement using the structure of *T. vulcanus* dPSIIcc (25) as a search model. All data processing, model building and refinement was done by Dr. Martin Bommer in the group of Prof Holger Dobbek, HU Berlin.

Data collection of dPSIIcc	
Wavelength (Å)	1.196
Resolution range (Å)	49.12 - 2.44 (2.52 - 2.44)
Space group	<i>P</i> 2 ₁ 2 ₁ 2 ₁
Unit cell	<i>a</i> = 116.4 Å, <i>b</i> = 218.9 Å, <i>c</i> = 302.2 Å $\alpha = \beta = \gamma = 90^\circ$
Total reflections	1700160 (103808)
Unique reflections	282213 (25467)
Multiplicity	6.0 (4.1)
Completeness (%)	98.4 (89.5)
Mean <i>I</i> / σ (<i>I</i>)	14.72 (1.93)
Wilson <i>B</i> -factor (Å ²)	39.05
R _{meas}	0.103 (0.798)
Refinement	
R _{work}	0.218 (0.313)
R _{free}	0.253 (0.363)
Number of atoms	50251
macromolecules	41425
ligands	8522
water molecules	304
Protein residues	5332
RMS(bonds) (Å)	0.006
RMS(angles) (°)	0.95
Ramachandran favored (%)	96
Ramachandran outliers (%)	0.37
Clashscore	5.43
Average <i>B</i> -factor (Å ²)	44.3
Protein	44.3
Ligands	44.6
Solvent	36.4

Table 3-3 Data collection statistics and refinement statistics

Numbers in parentheses refer to the highest resolution shell. Table provided by Dr. M. Bommer.

3.5 Structure of C₁₂E₈-dPSIIcc

The structure of C₁₂E₈-dPSIIcc exhibits all 20 protein subunits as already presented earlier (Figure 1-7, page 17), but additionally presents the subunit PsbY for the first time with full occupancy in the electron density map in both monomers (Figure 3-11).

The two PSIIcc monomers are rotated by 1.5° away from the membrane normal when compared to the structure from βDM-dPSIIcc. This is believed to be a result of the new crystal packing or the extraction of the detergent C₁₂E₈.

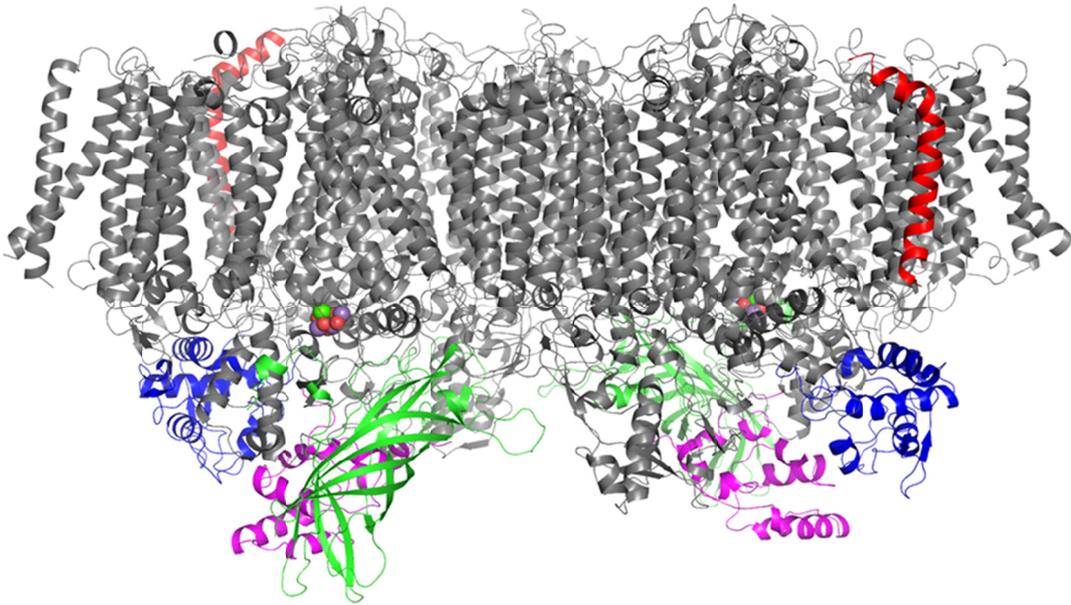


Figure 3-11 dPSIIcc structure at 2.44 Å resolution

Side view of the dPSIIcc crystal structure at 2.44 Å resolution, view along the membrane plane with the cytoplasmic side above and the luminal side below. All membrane intrinsic protein subunits are shown in cartoon mode in grey except for PsbY which is highlighted in red. The extrinsic protein subunits PsbV (blue), PsbU (pink) and PsbO (green) shown in cartoon mode at luminal side, Mn-cluster as green and red spheres for orientation.

3.5.1 Cofactors

Each monomer of the dPSIIcc exhibits the following cofactor composition: 35 Chl_a molecules, eleven β-Car molecules, two Pheo_a, two hemes (cyt b559 and cyt c550), a non-heme iron (Fe²⁺) with an associated bicarbonate ion, two PQ molecules (Q_A and Q_B) (no electron density was found at the Q_C binding site, as found before (23), 19 integral lipids and the WOC with two chloride ions close to the WOC (Figure 3-12).

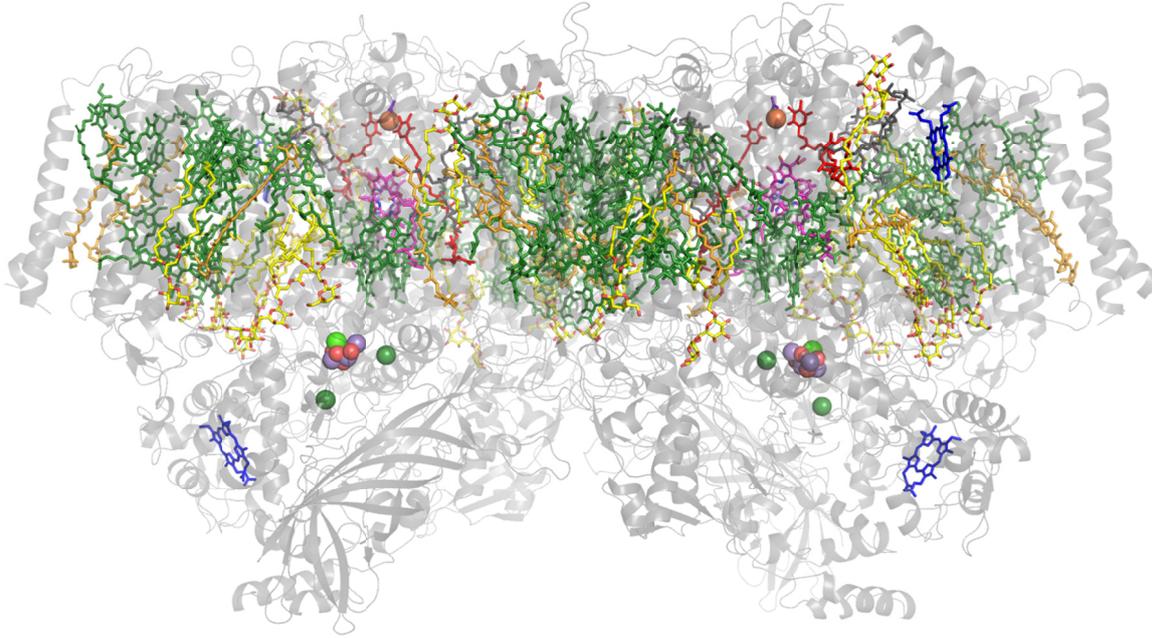


Figure 3-12 Cofactors in dPSIIcc at 2.44 Å resolution

The cofactors in dPSIIcc are shown from the cytoplasmic side. All protein subunits are presented in cartoon mode in transparent grey. Cofactors are shown in stick mode as follows: chlorophyll a (green), β -carotene (orange), plastoquinone (red), heme (blue), pheophytin a (pink), lipid (yellow, oxygen red), iron (orange sphere with associated bicarbonate (black, hardly visible)), chloride (dark green sphere), WOC with Mn (purple sphere), Ca (light green sphere), oxygen (red sphere).

3.5.2 Manganese cluster and Ca²⁺ and Cl⁻ binding sites

The catalytic OEC at the luminal side of dPSIIcc is presented in Figure 3-13 A. At the resolution of 2.44 Å it was not possible to determine distinct electron density for the oxygen atoms of the Mn₄CaO₅-cluster. Therefore the rigid-body Mn₄CaO₅-cluster of the PDB entry 3ARC was fitted into the experimental mFo-DFc omit map at 4 σ level in absence of the Mn₄Ca-cluster. The van-der-Waals radii for all Mn and Ca atoms are shown. The three additional Ca²⁺ binding sites (Figure 1-16, page 35) have not been revealed, questioning whether they are indeed only a result of crystal treatment with Ca²⁺ containing buffers (10 mM CaCl₂ (25)) and crystallization solutions and do not have functional importance as already suggested earlier (163). We do not have any CaCl₂ in our PEG-treatment buffer. Further density of the mFo-DFc map at 2.5 σ level was found for Cl-1 and Cl-2 in the vicinity of the Mn₄Ca-cluster, but no Cl-1B binding site was found and no third Cl-3 binding site was revealed (Figure 1-15, page 34). Close to Mn4 electron density for two water

molecules (W1 and W2) was found. Previously identified W3 and W4 (25) coordinated to Ca were not found. Given the lower resolution here, the observation of less water molecules was expected. A further 304 water molecules have been identified within the van-der-Waals surface of dPSIIcc (Figure 3-13 B).

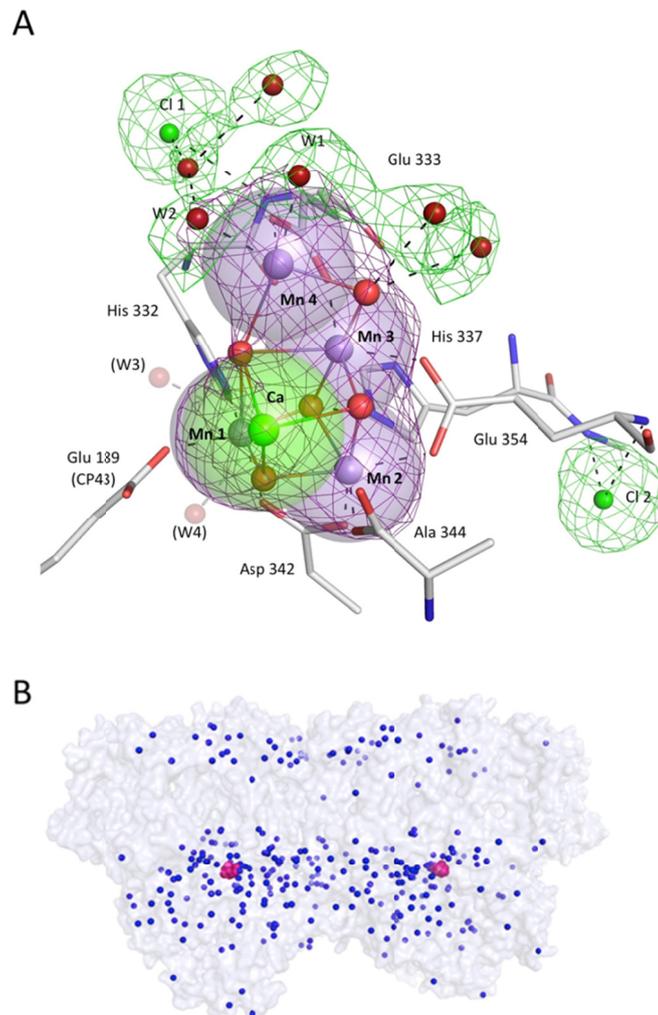


Figure 3-13 Mn₄Ca-cluster and detected water molecules

A) Electron density of the Mn₄Ca-cluster, waters and chloride. The core of the figure shows the rigid-body fitted Mn₄CaO₅-cluster of PDB entry 3ARC (25) with the experimental 4σ mFo-DFc simulated annealing omit map (purple mesh) generated in absence of the Mn₄CaO₅-cluster. Transparent spheres give van der Waals radii for Mn and Ca ions. Distinct electron density for oxygen atoms (red dots in the cluster) was not observed. Coordinating amino acid residues of subunit D1 or CP43 (if indicated), water molecules and chloride ions with corresponding electron density of the 2.5σ mFo-DFc map is shown as green mesh around the Mn₄Ca-cluster. B) Positions of the 304 water molecules identified in the present study are shown within the van-der-Waals surface of dPSIIcc. The Mn₄Ca-cluster is shown in pink. Figure provided by Dr. M. Bommer.

3.5.3 Lipids and detergent content

The integral lipids (excluding the periphery and interface region lipids) found in the previous structure of β DM-dPSIIcc at 2.9 Å resolution (23) and confirmed in the β DM/HTG-dPSIIcc at 1.9 Å resolution (25) were all found in the here obtained C₁₂E₈-dPSIIcc at 2.44 Å resolution. These are 4 DGDG, 5 PG, 4 MGDG and 1 SQDG, summing up to 14 integral lipids per PSII monomer (Table 3-4). Four PG molecules and one MGDG that have been identified in β DM/HTG-dPSIIcc were confirmed in C₁₂E₈-dPSIIcc. They were initially identified as four MGDG and one DGDG in β DM-dPSIIcc at 2.9 Å resolution, probably due to a wrong assignment of the lower resolution structure. One PG found in the Q_B cavity in β DM-dPSIIcc was neither found in β DM/HTG-dPSIIcc nor in C₁₂E₈-dPSIIcc. The fatty acid tails of the lipids found in the Q_B cavity were only partially resolved which indicates high flexibility. At the monomer-monomer interface only two lipids have been clearly identified here. Of the before two SQDG molecules one has been assigned to a MGDG due to the absence of a sulfate group (as present in SQDG) in the electron density map at 2.44 Å resolution. All other elongated electron density which could originate from PEG, detergent or partially observed lipids was modeled as individual alky chains and labelled unknown ligand (UNL) (abbreviation c in Table 3-4). In the interface region either very mobile lipids in β DM-dPSIIcc or detergent molecules/UNLs in the other dPSIIcc structures have been modeled, which suggests that the composition of lipids is poorly defined in all current high resolution structures at this region. At the surface of dPSIIcc or the peripheral region only one SQDG was retained when compared to the before modeled lipids. SQDG 213 which was discussed to be important for dimer formation is present at 2.44 Å and labelled SQD 668 (Figure 3-14). Additionally, two new MGDG molecules were modelled at the PSII dimer-dimer interface on the surface of the subunits CP43 and CP47. These two lipids mediate direct contacts between C₁₂E₈-dPSIIcc within the crystal along the crystallographic *a*-axis (Figure 3-14, Figure 3-16). Altogether the here modeled integral and surface area lipids are 7 MGDG, 4 DGDG, 3 SQDG and 5 PG molecules summing up to 19 lipids per PSII monomer (Table 3-5, page 83). With these results the identity and relative stability of integral lipids of dPSIIcc to extraction can be stated through their β DM-independent observation in C₁₂E₈-dPSIIcc crystals.

Lipid name	position in PSII	β DM-dPSIIcc, 2.9 Å	β DM/HTG-dPSIIcc, 1.9 Å	C ₁₂ E ₈ -dPSIIcc, 2.44 Å
DGDG	integral	DGD 489	DGD 657	DGD 657
DGDG	integral	DGD 208	DGD 663	DGD 663
PG	integral	LMG 531	LHG 664	LHG 664
MGDG	integral	LMG 533	LMG 669	LMG 669
PG	integral	LMG 373	LHG 694	LHG 694
PG	integral	LMG 360	LHG 702	LHG 702
MGDG	integral	DGD 370	LMG 751	LMG 751
SQDG	Q _B cavity	SQD 372	SQD 659	SQD 659
DGDG	Q _B cavity	DGD 490	DGD 660	DGD 660
DGDG	Q _B cavity	DGD 491	DGD 661	DGD 661
MGDG	Q _B cavity	LMG 359	LMG 692	LMG 692
PG	Q _B cavity	LHG 371	LHG 714	LHG 714
MGDG	Q _B cavity	LMG 492	LMG 729	LMG 729
PG	Q _B cavity	LMG 218	LHG 772	LHG 772
	Q _B cavity	LHG 374	2 x c	c
SQDG/MGDG	monomer interface	SQD 532	SQD 667	LMG 667
SQDG	monomer interface	SQD 213	SQD 668	SQD 668
	monomer interface	LMG 217	b	c
	monomer interface	DGD 375	b	c
	monomer interface	LMG 534	b	---
	monomer interface	LMG 220	c	---
DGDG	peripheral	DGD 362	(DGD 755)	---
SQDG	peripheral	SQD 224	SQD 768	SQD 768
MGDG	peripheral	LMG 493	LMG 776	c
MGDG	peripheral	---	LMG 784	---
SQDG	peripheral	SQD 361	2 x c	c
MGDG	dimer interface	---	---	LMG 785
MGDG	dimer interface	---	b	LMG 789

Table 3-4 Lipid positions in the β DM-dPSIIcc, β DM/HTG-dPSIIcc and C₁₂E₈-dPSIIcc

Lipids and their corresponding positions in dPSIIcc per monomer of β DM-dPSIIcc (PDB entry 3BZ1/3BZ2) and β DM/HTG-dPSIIcc (PDB entry 3ARC) and the present study (right side/ PDB entry 4PJ0). The upper part (integral/Q_B cavity) presents the integral lipids, the lower part the interface or surface lipids. The color code corresponds to the same lipid group respectively. The ligand abbreviations differ in the PDB entries (DGDG= DGD, PG= LHG, MGDG=LMG, SQDG= SQD). DGD 755 was uncertain and later removed again. Further abbreviations: b: modeled as detergent molecule, c: a single alkyl chain labeled as unknown ligand (UNL) was modeled, ---: no density was found.

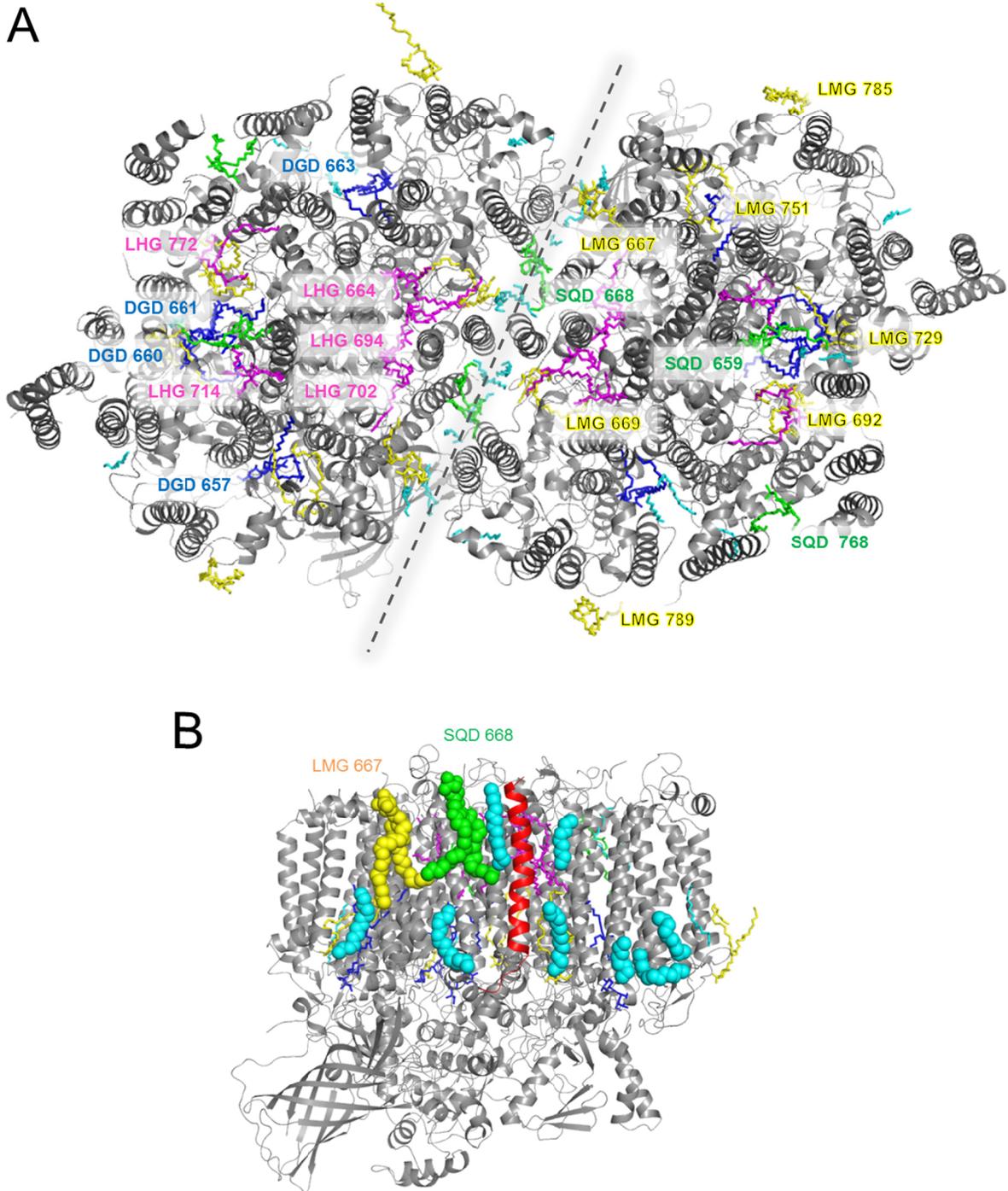


Figure 3-14 Integral lipids of dPSIIcc at 2.44 Å resolution

Lipids in the dPSIIcc according to the 2.44 Å resolution structure A) View from the cytoplasmic side onto the dPSIIcc. Protein subunits are shown in cartoon mode in grey, lipids and unknown ligands (UNL) in stick mode, MGDG (yellow), DGDG (dark blue), PG (pink), SQDG (green) and UNL (cyan). The monomer-monomer (m-m) interface is highlighted by a dashed line. For clarity DGDG and PG are labelled only on left monomer and MGDG and SQDG only on right monomer, but all lipids appear twice in the dPSIIcc and can be found when applying a C2 rotation. B) view along the membrane plane onto the lipids at the PSII m-m interface with SQDG (green), MGDG (yellow) and UNL (cyan) in sphere mode with subunit PsbM highlighted in red. For comparison of specific lipid positions with lipids in the 2.9 Å and 1.9 Å resolution dPSIIcc crystal structures see Table 3-4.

But what has happened to the detergent positions that have been found in the PSII structure before? Therefore the detergent and UNL positions of the highest resolution structure of β DM/HTG-dPSIIcc were compared to the C₁₂E₈-dPSIIcc structure. Most of the detergents β DM and HTG in β DM/HTG-dPSIIcc now feature long elongated density. This density might belong to the detergent C₁₂E₈, but unlike β DM it does not feature a carbohydrate head group and could not be assigned in the crystal structure. At the position of the PSII dimers bridging lipid MGDG (LMG 789) a HTG (744 or 789) was positioned in the respective positions on both sides of the dPSIIcc of the 1.9 Å resolution structure. So, of the 13 membrane-intrinsic detergent molecules (additional 2 HTG molecules have been found at the extrinsic region of PSII) of the β DM/HTG-dPSIIcc, 5 have been modeled as UNL, 2 as MGDG and 3 times no density was found. Comparing the positions of the 19 UNLs in the β DM/HTG-dPSIIcc structure, 9 UNLs were found, 3 times residual density and 7 times no density was found. This is well in line with the expectation, because in the obtained lower resolution of the 2.44 Å dPSIIcc structure the weakest ligands are no longer visible as compared to the 1.9 Å resolution dPSIIcc structure. If the UNLs belong to flexible lipids or the detergent C₁₂E₈ (for the 2.44 Å resolution structure) is not specifiable. To investigate the detergent positions of C₁₂E₈ in PSII, the purification and crystallization procedure needs to be carried out for example with Seleno-C₁₂E₈, which is detectable in the electron density map.

Lipids	2.44 Å
MGDG	7
DGDG	4
SQDG	3
PG	5
Unknown alky chains	29 in total
Detergents	-

Table 3-5 Lipids and UNLs of the 2.44 Å resolution dPSIIcc crystal structure

*Content of lipids within dPSIIcc per monomer and unknown alky chains (UNLs), derived from the dPSIIcc crystal structure of *T. elongatus* at 2.44 Å resolution. Detergent molecules could not be identified. UNLs could either belong to detergent, lipids or PEG.*

3.6 Crystal packing

Packing of dPSIIcc in the unit cell is presented in Figure 3-15. Along the *b*-axis as well as along the *c*-axis protein-protein contacts are provided by membrane extrinsic subunits PsbV and PsbU and between PsbO and the membrane intrinsic subunit PsbZ. The dPSIIcc form long rod-like structures with two PSII dimers providing protein-protein contacts at their respective cytosolic surfaces, which are arranged in a zigzag fashion (as presented in the right inset in Figure 3-16, page 85). This crystal arrangement is a common feature of untreated C₁₂E₈-dPSIIcc crystals, βDM-dPSIIcc crystals and C₁₂E₈-dPSIIcc after PEG treatment. Only the latter PEG-treated crystals present a completely new crystal packing along the *a*-axis. Initially type II C₁₂E₈-dPSIIcc crystals were formed, where detergent belts are retained, representing the same packing as in βDM-dPSIIcc (Figure 3-16, left side). The space between the single dPSIIcc is expected to be occupied by βDM hemimicelles precluding a closer protein arrangement; the same is the case for the detergent C₁₂E₈ before PEG treatment. As well as the aqueous solvent these detergent belts are commonly not observed with X-ray diffraction, except for single detergent molecules that are bound to the protein surfaces. A technique which can provide information about the detergent belt association around a membrane protein was provided by Berthaud et al. using small-angle X-ray scattering (121). After PEG treatment (dehydration, detergent removal) of C₁₂E₈-dPSIIcc crystals these were transformed to type I crystals where detergent belts are removed and proteins are arranged much closer as layers with direct contact between protein interfaces (Figure 3-16, right side). The in-crystal-rearrangement was not observed for βDM-dPSIIcc and is the first time such a transformation has been observed for dPSIIcc crystals, to our knowledge.

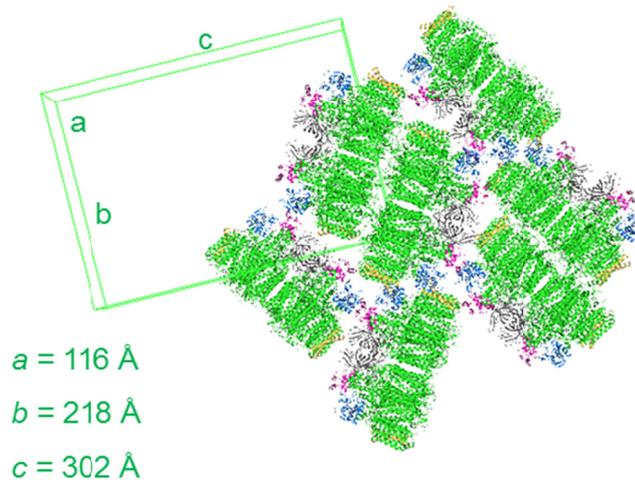


Figure 3-15 Crystal packing in the dPSIIcc unit cell

The packing of $C_{12}E_8$ -dPSIIcc (PDB 4PJ0) in the unit cell along the c-axis is shown. For clarity only seven dPSIIcc are shown exemplary in cartoon mode in green. Membrane extrinsic subunits PsbV (blue) and PsbU (pink), as well as PsbO (grey) and intrinsic subunit PsbZ (yellow) provide protein-protein contacts between adjacent proteins. Unit cell lengths are given in \AA .

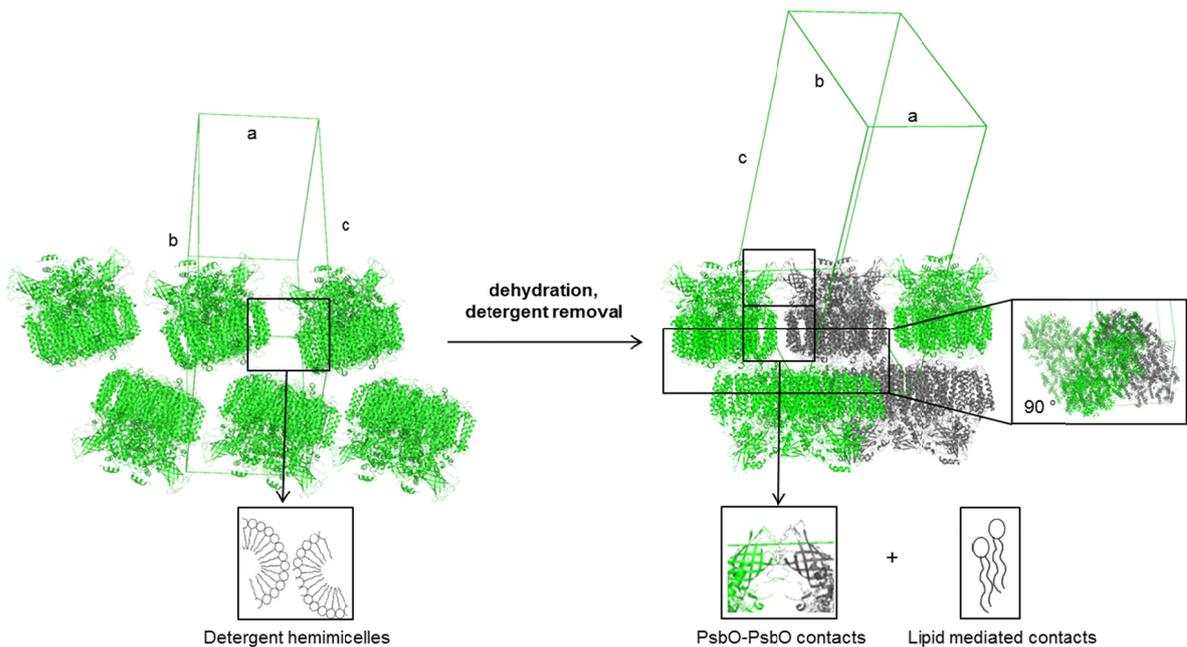


Figure 3-16 Protein rearrangement within $C_{12}E_8$ -dPSIIcc crystals

Left side) Type II crystal packing within β DM-dPSIIcc (PDB 2AXT) or within dPSIIcc as crystallized with $C_{12}E_8$. Three repeats of dPSIIcc along the crystallographic a-axis in 128 \AA (PDB 2AXT) or 140 \AA (HPF $C_{12}E_8$ -dPSIIcc crystals) intervals are shown. No direct protein-protein contacts are observed, hemimicelles are expected to occupy most of the space between proteins as shown in the inset. Right side) Type I crystal packing within $C_{12}E_8$ -dPSIIcc (PDB 4PJ0) crystals after dehydration and detergent removal. Repeats of dPSIIcc along the crystallographic a-axis in 116 \AA intervals are shown. Space between proteins is reduced and allows for direct protein (PsbO-PsbO) and lipid (2 MGDGs) mediated contacts. The right inset shows 90° rotated PSII dimers interlock in a zigzag manner with a multitude of protein interactions along their cytoplasmic surfaces.

The new crystal contacts that have been established after transformation are presented in detail in Figure 3-17. Shown are three repeats of dPSIIcc with 116.4 Å spacing along the crystallographic *a*-axis, with view from the cytoplasmic side onto the membrane plane of dPSIIcc. The crystal contacts are mediated by hydrogen bonds of two MGDG lipids (LMG 785 and LMG 789) with amino acid residues of subunits CP43 and CP47 and with Chl*a* 612. As the four MGDG lipid molecules per dPSIIcc interface were not added at any stage of the purification and crystallization protocol a specific interaction with at least one PSIIcc dimer is assumed. The second contact area is provided by residues Ser 139 and Thr 138 of two adjacent subunits PsbO, which are located in the so called cyano loop (164). The PsbO-PsbO interactions occur at a non-crystallographic pseudo-twofold axis. The cyano loop is exclusively found in cyanobacteria, the sequence is absent in PsbO of plants and green algae. The latter instead form supercomplexes with light-harvesting complexes which prohibit the formation of rows of PSII dimers (165).

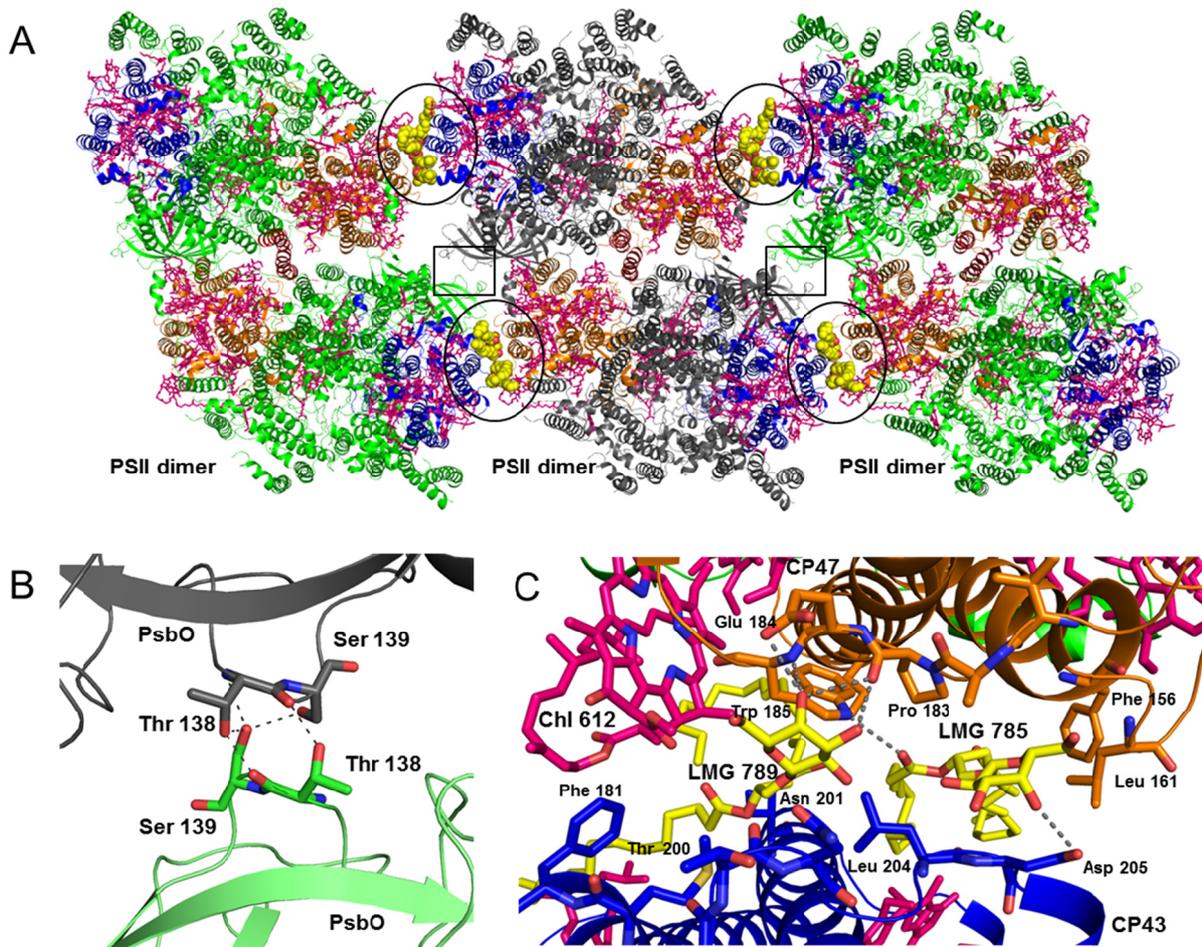


Figure 3-17 Crystal contacts in type I dPSIIcc crystals

A) Shown is a model from the cytoplasmic side onto a row of dPSIIcc with three repeats. Subunits in alternating color green and grey. PsbO subunits (small boxes, as enlarged in B) and two MGDGs (encircled, as enlarged in C) and subunits CP43 (blue) and CP47 (orange) and Chls pink. B) dimer-dimer contacts mediated between two PsbO residues (Ser 139 and Thr 138) located in the cyano loop. C) View from the stromal side, dimer-dimer interaction provided by two lipids MGDG (LMG 785 and 789) and a chlorophyll (Chl a 612) between subunits CP43 and CP47 of two adjacent dimers. Potential hydrogen bonds within a distance of 4 Å are shown as dashed lines.

The thylakoid membranes are tightly packed arrays built by lipids and up to 70 % protein (166). In these dense environments a certain extent of order seems inevitable to allow for an efficient electron transfer via plastoquinone as explored by simulations (167). As found by freeze-fracture electron microscopy (EM) studies of *Synechococcus*, dPSIIcc are arranged in 100-120 Å intervals forming long dPSII rows throughout the membrane (18). In another study on partially solubilized membranes of the mesophilic cyanobacterium *Synechocystis* PCC6803 (17) arrays arranged of several single rows of PSII dimers with 122 Å intervals have been found.

The perfect match of these rows of PSII dimers as presented in the EM studies in (17) and along the crystallographic *a*-axis of C₁₂E₈-dPSIIcc after PEG treatment is shown in Figure 3-18. Thus the arrangement of C₁₂E₈-dPSIIcc within the crystal reflects the *in vivo* situation of the cyanobacterial thylakoid membrane. It is suggested that upon detergent removal the dPSIIcc are arranged in an energetically favored form towards that found in the thylakoid membrane. Calculations by the PISA (Protein Interfaces, Surfaces and Assemblies) server (168), conducted by Dr. Martin Bommer, calculated a dimer-dimer contact area of 1395 Å² and predicted a free energy of formation of -9.6 kcal/mol. For the monomer-monomer contact -35.4 kcal/mol and a contact area of 2121.8 Å² have been derived, as well as -3.4 kcal/mol and a contact area of 677.9 Å² for the PsbV/U and PsbO/Z interaction which is not physiological relevant, but obtained due to crystal packing. The rather weak dimer-dimer interactions could imply to be an artefact of high protein concentration or only occur due to three dimensional crystal packing, but a similar situation exists in the thylakoid membranes where orientation is restricted to the membrane plane and the protein concentration can vary from 30-70 %. A further reason for a certain degree of flexibility of the PSII dimer interactions would be needed for D1 turnover during PSII repair. The presented first high resolution model of such superstructures can serve as a basis for theoretical analysis of EET in the thylakoid membrane (169). The physiological role of these rows and arrays is not yet fully understood (170). The EET between the PSII inner antennae proteins CP43 and CP47 and the transfer to the RC occurs in the picosecond timescale (65) which is two orders of magnitude slower than the primary ET in the RC (171). Thus an efficient EET has to be facilitated by a certain degree of order which could indeed be the row like array arrangements. In order to explain the physiological relevance of the formation of arrays and rows, also the photochemical efficiency of dPSIIcc has to be considered. Caffarri et al. calculated the photochemical efficiency of EET for plant PSII to be 89 % if both monomers have an open RC (172). An open RC means that both, the electron donor P_{D1} and the electron acceptor pheophytin within PSII are participating in charge separation (173). If one RC is closed, the other open RC can still participate in EET. The photochemical efficiency was then calculated to be 78 % through the connection of two PSII monomers. Compared to this, two separate PSII monomers, with one being unable to perform photosynthesis and one with 89 % efficiency, result in 45 % efficiency each. Thus the connection into PSII dimers can raise the light harvesting

efficiency by about 70 % (172). In cyanobacteria the rows of PSII dimers (Figure 3-18) allow the connection with four more RCs which will increase the efficiency further. An overlay of the crystalline membrane arrays of PSII dimers of the cyanobacterium *Synechocystis* PCC6803 as found by Folea et al. (17) and the single rows of the X-ray structure of dPSIIcc (PDB code 4PJ0) is presented in Figure 3-19. The resulting superstructure arrays may be connected via attached mobile phycobilisomes *in vivo* to connect even more RC with each other as the small PSII subunits at each side (PsbD, PsbF, PsbK, PsbZ) of the RC complexes do not contain pigments that could transfer excitation energy. This is further considered to prevent energy spill-over from PSII to PSI complexes (17), or may be a consequence of temperature and high or low light acclimation. The third type of crystal contact is provided at the cytoplasmic side of dPSIIcc (Figure 3-16, right side) which has recently been shown by crosslinking studies of protein subunit residues K277 (CP47), K457 (CP43), K35 (PsbI), K23 (D2) to the phycobilisome core ApcE protein to be the site of phycobilisome attachment (17).

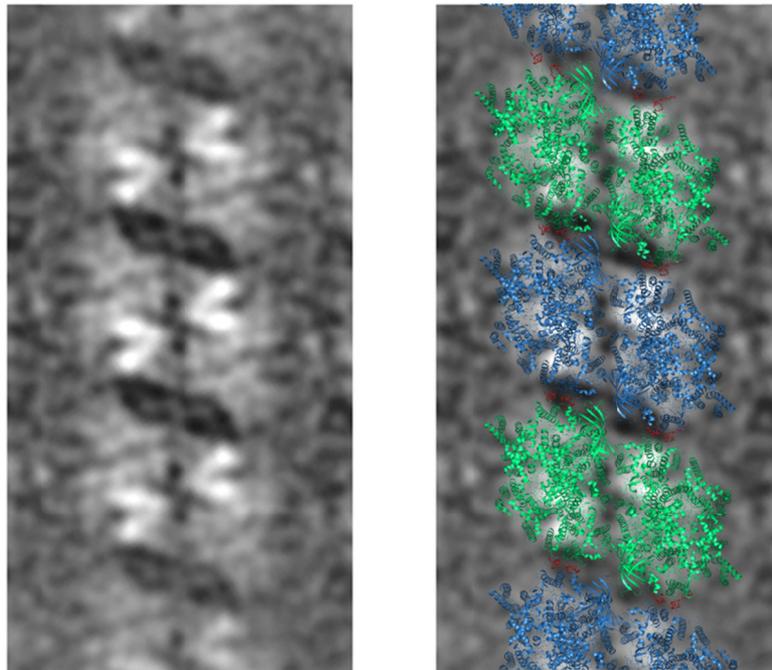


Figure 3-18 Overlay of the X-ray structure of dPSIIcc and electron micrographs of PSII dimers in the thylakoid membrane

Left side) EM image by M. Folea et al. (17) (background EM picture provided by Prof. E. Boekema with the permission to reproduce) of partly solubilized membrane fragments. Shown is a vertical row of PSII dimers from the luminal side. Right side) Overlay of the X-ray structure of dPSIIcc (alternating in blue/ green) and the EM image. Bridging MGDG lipids (red), the EM image was scaled to 11.6 nm dimer repeat (before 12.2 nm).

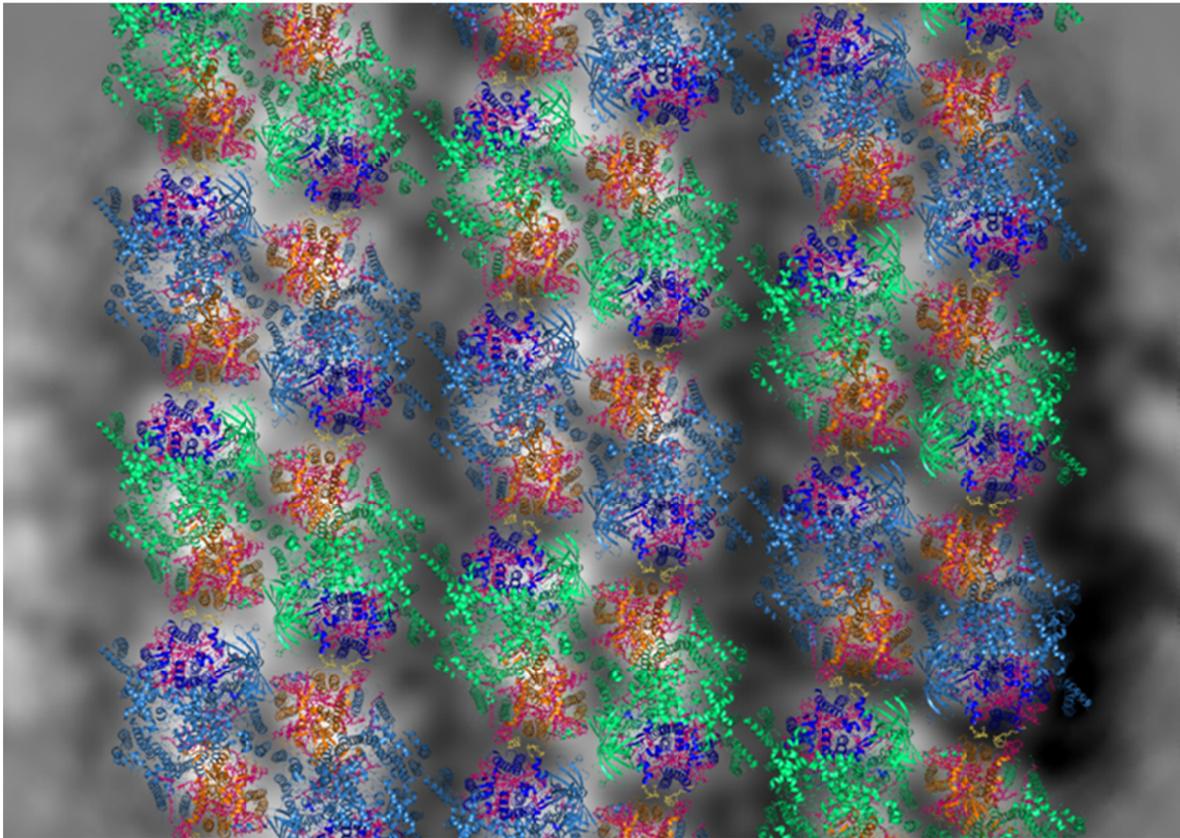


Figure 3-19 Overlay of the X-ray structure of dPSIIcc and electron micrographs of crystalline membrane arrays of PSII dimers

The EM image by Folea et al (17) (background EM picture provided by Prof. E. Boekema with the permission to reproduce) of partly solubilized membrane fragments of shows crystalline 2D arrays (grey background). The overlay of the X-ray structure of dPSIIcc (alternating in blue/ green) is shown from the luminal side with light harvesting subunits CP47 (orange) and CP43 (dark blue) and chlorophyll molecules in stick mode (pink). The EM image was scaled to 11.6 nm dimer repeat (before 12.2 nm).

The crystal packing was derived with a post crystallization dehydration which is a common method to improve the crystal quality (154, 174, 175) and has been employed with a different procedure by Umena et al. (25) for dPSIIcc from *T. elongatus* to result in 1.9 Å resolution. The detergent combination of HTG/ βDM together with the dehydration procedure and a reduction of water content resulted in a more compact crystal packing resulting in a 10 % reduction of the unit cell size. No evidence for a detergent extraction was reported. The dehydration procedure with the C₁₂E₈-dPSIIcc crystals allowed for an extraction of water as well as detergent from the dPSIIcc crystals and resulted in the type I crystal packing. Both procedures were not successful with βDM-dPSIIcc crystals of *T. elongatus*. In particular the crystallographic *a*-axis, which is determined by the packing of protein with detergent

hemimicelles, never decreased below 126 Å for βDM-dPSIIcc crystals (23) compared to 122 Å reported for βDM/HTG-dPSIIcc crystals (25) and 116 Å for C₁₂E₈-dPSIIcc. This suggests that the detergent belt manipulation is a key step towards crystal transformation.

3.7 CMC measurements

In order to estimate the detergent belt manipulation the effect of PEG 5000 MME on the CMC was studied. It was suggested that PEG 5000 MME does not only contribute to the dehydration of the crystals but further stimulates the extraction of the detergent C₁₂E₈. This effect was not observed when using the detergent βDM. In order to provide an experimental proof, the effect of PEG 5000 MME on the CMC of both detergents was determined. In a simplified picture, the CMC may be considered as the equilibrium constant of micelle formation. The equilibrium exists between m detergent molecule (D) monomers and a detergent micelle consisting of m detergent molecules ($m D \leftrightarrow D_m$). Figure 3-20 shows the plot of the $\ln(\text{CMC}/\text{CMC}_0)$ as a function of the PEG 5000 MME concentration. CMC_0 is the CMC of the detergent in absence of PEG 5000 MME. The quantity of $\ln(\text{CMC}/\text{CMC}_0)$ is interpreted as the change of Gibbs free energy of micelle formation due to PEG 5000 MME. Assuming that PEG 5000 MME does not interact in a significant way with the micelles, the change of the Gibbs free energy should be the stabilization of the detergent monomers in solution. As can be seen in Figure 3-20, the effect of PEG 5000 MME is larger for C₁₂E₈ than for βDM. That means that C₁₂E₈ monomers are more stabilized by PEG 5000 MME than βDM monomers. The stabilization of monomers should shift the equilibrium of micelle formation to the left, thereby increasing the CMC. Further it should shift the type II crystal form to the formation of type I crystals with the concomitant release of an unknown amount of detergent molecules into the mother liquor. It is thus considered that by stabilization of, in particular the detergent C₁₂E₈ in solution, PEG 5000 MME contributes to the extraction from the crystals and thereby contributes to the transformation of the crystals. Additional to this result it is assumed that the slim molecule C₁₂E₈ contributes to the needed molecular flexibility to leave the type II crystal. In contrast to this βDM exhibits a bulky and hydrogen bond forming

maltoside headgroup (Figure 3-1). CMC measurements were conducted by D. DiFiore and data interpretation by Dr. F. Müh.

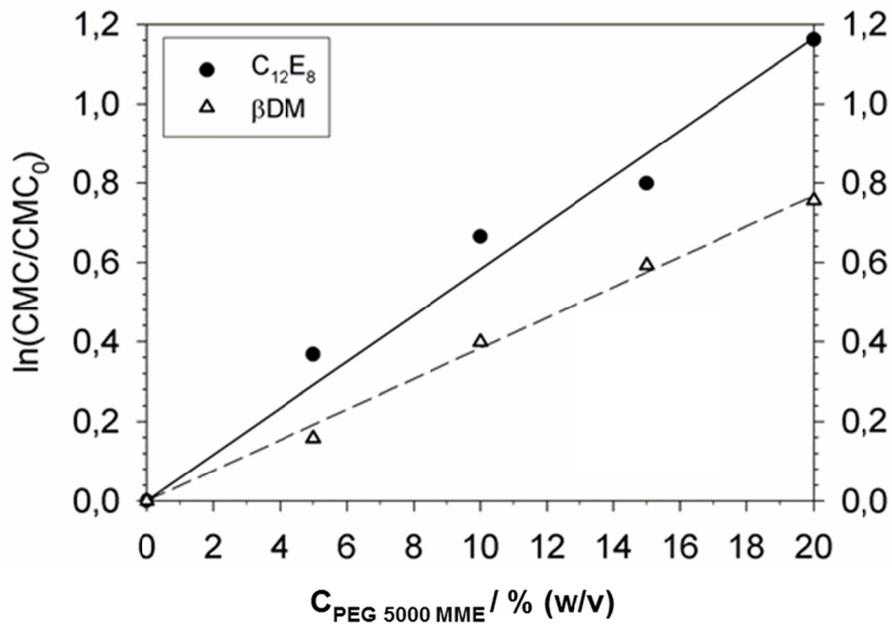


Figure 3-20 Influence of PEG 5000 MME on the CMC of the detergents $C_{12}E_8$ and βDM

The plot shows the quantity of micelles $\ln(\text{CMC}/\text{CMC}_0)$, which is proportional to the change in Gibbs free energy of the micelle formation due to PEG 5000 MME. CMC_0 is the CMC at zero PEG 5000 MME concentration. Measurements were conducted for βDM and $C_{12}E_8$ in the same buffer as used for crystallization of the dPSIIcc (0.1 M Tris (pH 7.5), 0.1 M $(\text{NH}_4)_2\text{SO}_4$). Figure provided by Dr. Frank Müh.

3.8 Summary

Here the successful purification and crystallization of dPSIIcc for the first time exclusively using the detergent C₁₂E₈ is presented. The C₁₂E₈-dPSIIcc solution showed high oxygen evolution activity and sufficient purity to routinely gain dPSIIcc crystals of 200-400 μm size. The observation of only dPSIIcc and no mPSIIcc peak as obtained when using the detergent βDM suggests a stabilization of the dimeric form by the detergent C₁₂E₈. Whereas the before found integral lipids were all retained with the different detergent, lipids in the interface or peripheral regions seem highly flexible and unspecific, their visualization depending on the resolution and purification procedure. The detergent C₁₂E₈ was likely incorporated in the complex as elongated density was found, but due to the lack of a prominent headgroup not distinguishable from either PEG or flexible lipids in the electron density map. A completely new crystal packing of dPSIIcc is presented. Until now dPSIIcc crystals always packed as type II crystals with protein surrounding detergent micelles. Besides the cryoprotection properties of PEG 5000 MME when using it for 100 K SR measurements, also a drastic post crystallization treatment was introduced. This was corresponding to a dehydration procedure, but additional to the reduction of the water content in the crystal, the detergent content was reduced. The reduction of C₁₂E₈ is believed to be induced by the high (40-50 %) PEG 5000 MME which was found to stabilize detergent monomers in solution, thereby shifting the equilibrium from a type II crystal form to a type I crystal form. The new packing of dPSIIcc within the crystal further resembles that of an *in vivo* arrangement in the thylakoid membrane as found in EM studies of thylakoid membrane fragments. For the first time a detailed structural model is presented which can give valuable basis for EET studies. The stabilizing subunit of PSII dimers is found at the PsbO cyano loop which is exclusively found in cyanobacteria and absent in plants. This is concomitant with a different arrangement of plant PSII as they lack phycobiliproteins, but have light harvesting complexes that allow for a completely different organization in the membrane. The dPSIIcc are further connected via 4 MGDG lipid molecules per dimer-dimer interface at the subunits CP43/CP47 and a specific binding site to at least one of the dimers is suggested. Concomitant with the new packing a dramatic improvement of resolution from 6 Å to 2.44 Å was obtained, gaining a dataset of dPSIIcc with all 20 subunits, including the low occupancy subunit PsbY that has been

lacking at least partly in all PSII structures before. This is believed to be a further effect of C₁₂E₈ stabilizing the whole dPSIIcc. Thus the purification and crystallization protocol for dPSIIcc using the detergent C₁₂E₈ represent a new way to gain dPSIIcc crystals with good resolution and may be used for future dPSIIcc crystal studies.

4 Serial femtosecond X-ray diffraction and X-ray emission spectroscopy of dPSIIcc microcrystals

Introduction

The most prominent method for structure determination of PSII crystals was so far X-ray crystallography at SR sources. When starting this study, the best diffraction data set obtained for dPSIIcc from *T. elongatus* crystals using SR was at 2.9 Å resolution (23). For the SR XRD measurements the dPSIIcc crystal sizes ranged from 300-600 µm in length. While collecting a full diffraction dataset, the crystal was mounted with a loop and immediately cooled to cryogenic temperatures (100-150 K), then shifted several times during measurement to decrease radiation damage and rotated around its axis to gain a complete data set. The destructive impact that SR has on a PSII crystal is reduced by cryo-cooling, thus freezing it, but radiation damage, which severely destroys parts of the protein within the crystal during data collection is never completely eliminated (Figure 1-20, page 46). The radiation damage limits the resolution of the crystal and changes the precise conformation of radiation sensitive parts of the protein most of all the Mn-cluster (Chapter 1.4.2, page 42). This is nevertheless the method of choice when unraveling the overall protein structure, but limitations are present when structural details with high radiation sensitivity are to be unraveled. With the development of X-ray free electron lasers (XFEL), which are the next generation of X-ray sources, a new opportunity was provided. The impact such an electron laser could have on biomolecular imaging was described already in the year 2000 by Neutze et al. (134). An XFEL provides pulses in the fs-range (<100 fs) which is by three orders of magnitude faster than SR. These ultrafast pulses enable to collect diffraction data before the onset of radiation damage of the crystal even without cryo-cooling, making it possible to collect data at RT. The brilliance or brightness (photons per area) of the light pulses delivered by an XFEL is more than twelve orders of magnitude higher than X-rays delivered by third generation synchrotrons. This enables to do measurements with microcrystals of only a few µm sizes. Around 10^{12} photons are delivered per light pulse and the beam can further be focused down to 1-2 µm². Each microcrystal is immediately destroyed in this high energetic beam, thus a constant delivery of new microcrystals is necessary to gain a

complete dataset. In 2011, at the Linac Coherent Light Source (LCLS) with the Coherent X-ray Imaging (CXI) endstation (176), the first XFEL operating in the hard X-ray regime (177) producing 5-400 fs X-ray pulses with up to 10^{12} photons per pulse and energies of 6-10 keV with a repetition rate of 120 Hz, became accessible for this project. As a major goal of photosynthetic research remains the urge to unravel the catalytic S-cycle of the oxidation of water to molecular oxygen. This task needs a method that is able to catch the proteins molecular arrangement in each oxidation state and the dynamic process of molecular rearrangement. The water oxidation takes place at the OEC, the Mn_4O_5Ca -cluster, embedded in the subunit D1 of PSII (Chapter 1.3.7, page 28). The OEC cycles through 5 steps of the S-cycle (S_i states, $i= 0-4$), each step is triggered by a photon ($\lambda= 674nm$) and results in the release of electrons and protons and the change of bond distances of the cluster (Chapter 1.3.8, page 29). It is of wide interest to capture the S_4 state, in this state it is believed that O-O bond formation takes place. In 2011, an improved SR X-ray structure of this cluster presented for the first time the oxygen atoms of the cluster and the μ -oxo-bonds linking the four manganese atoms and one calcium at a resolution of 1.9 Å (25). This was a big step towards understanding of the water oxidation process, as it also unraveled possible substrate water molecules and amino acid ligands close to the OEC (Figure 1-12, page 29). A severe problem that persists with SR XRD measurements even though the resolution gets better, is the radiation damage that reduces the Mn_4O_5Ca -cluster to still 25 % for the latest 1.9 Å resolution dPSIIcc crystal structure from *T. vulcanus*. The SR-induced reduction leads to the formation of Mn(II) from higher oxidation states of Mn(III) and Mn(IV) from the OEC, as revealed by non-reducing EXAFS and XAS studies (129, 131). Concurrently with this reduction the manganese-manganese distances increase and surrounding amino acids, ligands and the cluster itself rearrange. A new method that keeps the OEC in an undamaged state was needed. The feasibility of XRD at an XFEL with the “probe-before-destroy” method was successfully demonstrated for PSI nanocrystals by Chapman et al. (135). As the crystals are destroyed once hit by the high energetic X-ray laser beam, the prerequisite for this method are highly diffracting microcrystals that are constantly delivered to the interaction region by a special designed injector setup to collect a full dataset. Additionally XES, a method that has been frequently used for the study of metalloproteins, coordination complexes and inorganic catalytic centers at SR sources should be applied. This method probes the occupied electron

levels and provides information about the charge and spin states as well as the ligand environment of redox-active metal sites (Chapter 2.2.15, page 58). So far, the limitation of SR based XES measurements, to understand catalytic pathways in biological systems, is the use of cryo-trapped methods. SR XES at RT, at the functional condition of many biological systems, results in severe radiation damage. Cryo-cooling of the samples on the other hand provides frozen states and thus does not allow probing the electronic structural changes at a wide range of time scales as it does not offer the functional ambient condition. XFELs provide a way to overcome the limitations of SR based XES as it allows studying the dynamics of the electronic structure in the fs time frame. Fs XRD together with fs XES with the method of serial femtosecond crystallography (SFX) should provide undamaged snapshots of water oxidation during the S-cycle (Figure 1-13, page 30).

4.1 Experimental setup for serial femtosecond crystallography

As the intense pulses destroy the sample once hit, a fast and constant delivery of crystals is needed for SFX. A special designed sample injector which is described in the following accomplishes the experimental setup for the SFX measurements (Figure 4-1). Previous SFX experiments used a gas dynamic virtual nozzle (GDVN) that injects a microjet into vacuum by using a gas sheath to focus the flow (178). This GDVN is a successful tool in SFX experiments, but has a high flow rate, consuming the sample with a rate of 10–50 $\mu\text{l}/\text{min}$. In between the 120 Hz shots is a 8.3 ms delay time wasting the continuously passing sample. The consumption rate should be reduced by using a microjet similar in diameter, but with a lower flow rate, as this would consume less protein sample. For comparison at a flow rate of 10 $\mu\text{l}/\text{min}$, 1.4 nl of unused sample is wasted, whereas at a flow rate of 0.2 $\mu\text{l}/\text{min}$ only 0.028 nl is wasted. An alternative to the GDVN injector was provided by the use of an electrospray microjet. A sufficiently high electric field forms an electrospray by overcoming the surface tension and focusing the surface of a liquid into a microjet. Then shortly after, the microjet breaks apart into highly charged droplets (179). The potential use of electrospray voltage-assisted microjets for SFX has not been tested before, due to concerns regarding the high divergence of the droplet stream and the putative impact of the electric field on the protein microcrystals in the small charged

droplets. In our sample delivery system we use a principle utilized in electrospinning (180) in which the length of the microjet is extended and stabilized by addition of glycerol and PEG instead of creating separate crystal droplets of an electro spray. This keeps the microcrystals in a focused liquid jet as long as necessary to ensure interaction with the X-ray beam before possible disturbing effects due to droplet formation occur. The length of the microjet was controlled by varying the flow rate and the applied electric field downstream of the sample delivery capillary (180). SFX at CXI is performed inside a vacuum chamber at a pressure of < 0.01 Pa to minimize background scattering from air, thus stable operating parameters below atmospheric pressure had to be established to generate the electrospun microjet. Crystal suspensions in glycerol/water (25-40 % (w/v)) mixtures showed excellent stability below 0.01 Pa. The addition of glycerol further contributes the positive effect that crystal settling is reduced. It minimizes settling of the crystal suspension in the capillaries during acquisition and during storage in the reservoir prior to measurement. Further it decreases the formation of crystal aggregates and clogging of the capillaries. For the initial studies the protein thermolysin was used as a model system for capillary and flow rate tests. For this test a 100 μ l aliquot of thermolysin crystals in a buffer consisting of 30 % glycerol (w/v), 10 % PEG 2000 (w/v), 0.1 M MES pH 6.5 and 5 mM CaCl_2 was filtered through an 8 μ m Nucleopore membrane into a microcentrifuge tube. The tube was loaded into a pressurized cell, which established the fluid transfer into the SFX vacuum chamber via a silica capillary (114 cm long, 50 μ m inner diameter and 150 μ m outer diameter). The tube further provided the electrical contact between the sample and a platinum electrode (Figure 4-1). A potential of +2.5 kV was applied to the platinum electrode and a potential of -0.2 kV to the counter electrode which was positioned ca 5-8 mm away from the capillary exit. This achieved electric fields between 3400-5400 V/cm. The pressure was adjusted by varying the N_2 backing pressure applied to the solution and tuned to 0.17 μ l/min. SFX XRD data of thermolysin microcrystals (ca 14 000 single shot diffraction patterns) resulted in diffraction beyond 4 \AA resolution and showed that the electrospun injector system has no observable impact on the microcrystal condition. Thus, the electrospun microjet provided an opportunity for SFX to deliver small sample volumes of ≥ 25 μ l at low flow rates of 0.14–3.1 μ l/min. The additional compatibility to the experimental setup required for pump-probe and XES experiments made it suitable for the studies of dPSIIcc microcrystals. The injector

system was designed and established by the group of Mike Bogan at SLAC, Stanford (181).

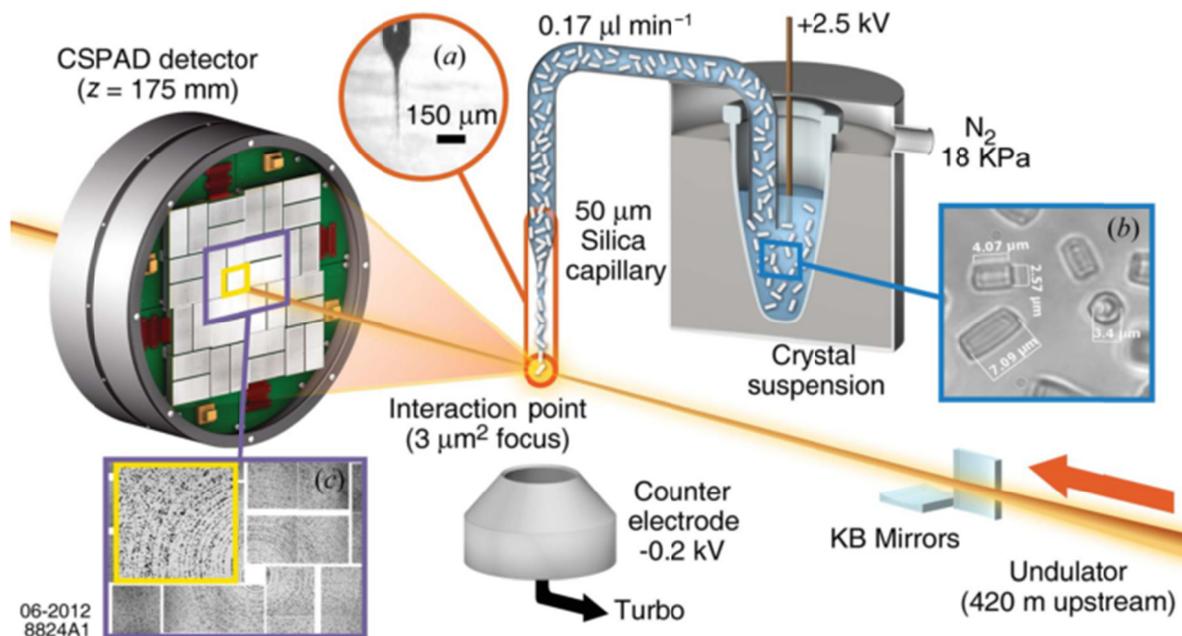


Figure 4-1 Setup of the nanoflow electrospun injector used for SFX at the CXI endstation

Schematic setup of microcrystal delivery to the interaction point by an electrospun microjet as seen in (a) of a thermolysin crystal suspension shown in (b) (microscopy image, sizes as indicated). It jets at 0.17 $\mu\text{l}/\text{min}$ via a silica capillary under 18 kPa N_2 pressure to the interaction point, where the crystals are hit by the X-ray beam. Single shot diffraction of individual crystals is collected by a Cornell-SLAC Pixel Array Detector (CSPAD). A schematic powder pattern from LCLS shots is shown in (c). Purple and yellow squares refer to the parts of the CSPAD shown in the enlarged powder pattern. Taken from (181), reproduced with permission of the International Union of Crystallography <http://journals.iucr.org>.

4.2 Preparation of dPSIicc microcrystals

The setup of the electrospun microjet, as described in Chapter 4.1, with the capillary tubes inner diameter ranging from 50-100 μm , needs a constant crystal delivery of high quality microcrystals at sufficient concentrations. The capillary inner diameter did not allow the use of crystals bigger than 50 μm to guarantee a constant flow without clogging of the capillary. Crystal size has a direct effect on the intensity of the peaks in the diffraction patterns as the scattering power is proportional to the crystal volume in the beam. A small crystal usually gives fainter diffraction than a bigger one due to dose-limited exposure times. Crystal size further has an important impact on the diffraction quality or more precise the mosaicity, which is a quantity for the long-range

disorder of a crystal. It was postulated by Hunter et al. (135) that for large crystals misalignments of molecules can spread in different domains, whereas for small crystals the increased surface area in contrast to the volume can lead to a reduced number of crystal contacts and cause misalignment of a larger percentage of molecules. Nevertheless, the mosaicity of nanocrystals remains unknown until now, but studies using XFEL sources are hoped to unravel the relationship between crystal size and mosaicity (182). Serial nanocrystallography studies have been made for the large membrane protein PSI (36 protein subunits, 381 cofactors and 1 MDa molecular mass) by Hunter et al. (182). This study showed that it was possible to obtain powder diffraction patterns from 100 nm³ crystals at SR beamlines, which was the prerequisite for the intended measurements at an XFEL source. PSI crystals, as well as PSII crystals, have high solvent content (78 % for PSI (182) and 57-66 % for PSII (25)) which results in a low number of crystal contacts. Both have large unit cell volumes, resulting in fewer proteins per unit cell and subsequently less proteins in one crystal. This leads to weaker diffraction as compared to proteins with small unit cells. These first studies demonstrated that serial nanocrystallography is possible for membrane proteins with large unit cells and high solvent content. PSI nanocrystals (200 nm – 2 μm) were later measured at an XFEL by Chapman et al. resulting in a data set with 8.5 Å resolution (135).

Crystallization

The PSII solution has been obtained from cyanobacterial *T. elongatus* with the purification protocol, using the detergent βDM, as described before in reference (120). A batch crystallization protocol was available that leads to dPSIIcc with an average size of 300-600 μm, as needed for SR XRD measurements. Changing this protocol in order to gain microcrystals of unique size and diffraction properties was intended. Initial experiments included tests of different Chla concentrations (0.3 - 4 mM) and PEG concentrations (a broader range around 10 % was tested) in a microbatch approach to find a condition for maximum nucleation. The best condition was found for 0.74 mM Chla (corresponding to 7.4 mg/ml dPSIIcc) in a buffer containing 0.1 M PIPES pH 7.0, 5 mM CaCl₂ and 0.03 % βDM mixed 1:1 with 10.4 % (w/v) PEG 2000 in the same buffer in a batch approach. Other setups yielded no crystals, precipitated material or oddly shaped crystals such as fern-like shaped crystals. The starting volumes ranged from 0.5 - 3 ml. Crystal formation started within

2 - 3 hours and microcrystals of various sizes ranging from less than 10 μm to more than 200 μm have been obtained at 4 $^{\circ}\text{C}$ overnight. It was important to obtain as many microcrystals of unique size as possible out of one setup, but the time of nucleation and growth was limited as the microcrystals in the crystallization solution grow further in size with time. Thus, to avoid the continuous growth of microcrystals, growth had to be stopped in a controlled way. In order to achieve this, the setups were transferred to Eppendorf cups, centrifuged and subsequently the supernatant protein solution was removed and exchanged with a buffer containing 0.1 M MES (pH 6.5), 5 mM CaCl_2 , 0.015 % β -DM, and a slightly higher precipitant concentration (10 % (w/v) PEG2000) than in the crystallization condition to avoid resolubilization of the microcrystals.

Size separation

A centrifugation step was necessary to avoid loss of very small and light microcrystals in the supernatant region. Still, the possible impact of centrifugation on the crystal quality was questioned. After centrifugation microcrystals were resuspended in a small volume and united. As it was absolutely important to remove crystals bigger than the inner diameter of the capillary, crystals had to be further sorted. Initially, crystals have been pushed through a mesh filter (Nucleopore track etch membranes, Whatman) with a pore size of ca 8 μm , for size separation. This did not result in the best crystal yield as they occasionally got stuck on the membrane and further this procedure using pressure to push them through the mesh pores was believed to harm the very fragile microcrystals. Thus, in an improvement step, a milder way was used by introducing a glycerol gradient ranging from 0 - 40 % glycerol (w/v) in buffer containing 0.1 M PIPES pH 7.0, 5 mM CaCl_2 , 0.03 % β DM and 10.5 % (w/v) PEG 2000 (Figure 4-2). The gradient used 200-300 μl volumes pipetted in layers on top of each other. After application of crystals and their subsequent settling (overnight), every layer was checked with a light microscope for crystal size distribution. This allowed obtaining microcrystals with < 50 μm as desired for the experimental setup. The gradient provided a way for size separation making use of the different velocity of the sinking crystals. To avoid the broad size distribution of the dPSIIcc crystals from the beginning, improvement of different crystallization setups was tried by making use of a broad interface of the crystallizing solution and the air in order to induce quick nucleation at the interface. The setup with pipetted lines of the mixed crystallizing solution on glass plates resulted in an increased amount of crystal

nucleation, but subsequent handling of the crystals using this setup turned out to be impractical. Thus, in the next batch approach a direct interface between the crystallization solution (0.74 mM Chl_a (or 7.4 mg/ml dPSIIcc) in 0.1 M PIPES pH 7.0, 5 mM CaCl₂ and 0.03 % β DM) and the precipitation solution (0.1 M PIPES pH 7.0, 5 mM CaCl₂, 0.03 % β DM and 10.5 % (w/v) PEG 2000) was established. In culture tubes these two were carefully pipetted in two layers, with the precipitation solution being the bottom one. Once crystal had formed at the interface they slowly sank down in the precipitation solution and were subsequently stopped from growing overnight.

After mild centrifugation the combined setups were transferred stepwise from the harvesting buffer to a final buffer containing 0.1 M MES pH 6.5, 5 mM CaCl₂, 0.015 % β DM, 10 % PEG 2000 (w/v) and 30 % glycerol (w/v). The buffer with only 10 % PEG 2000 and no glycerol did not electro spray in vacuum, due to freezing at the nozzle exit of the capillary. Thus, 30 % glycerol was added as a cryo-protectant to eliminate freezing and help forming a stable microjet. This combination further contributed to a lower flow rate operation and reduced the settling of crystals during the experiments.

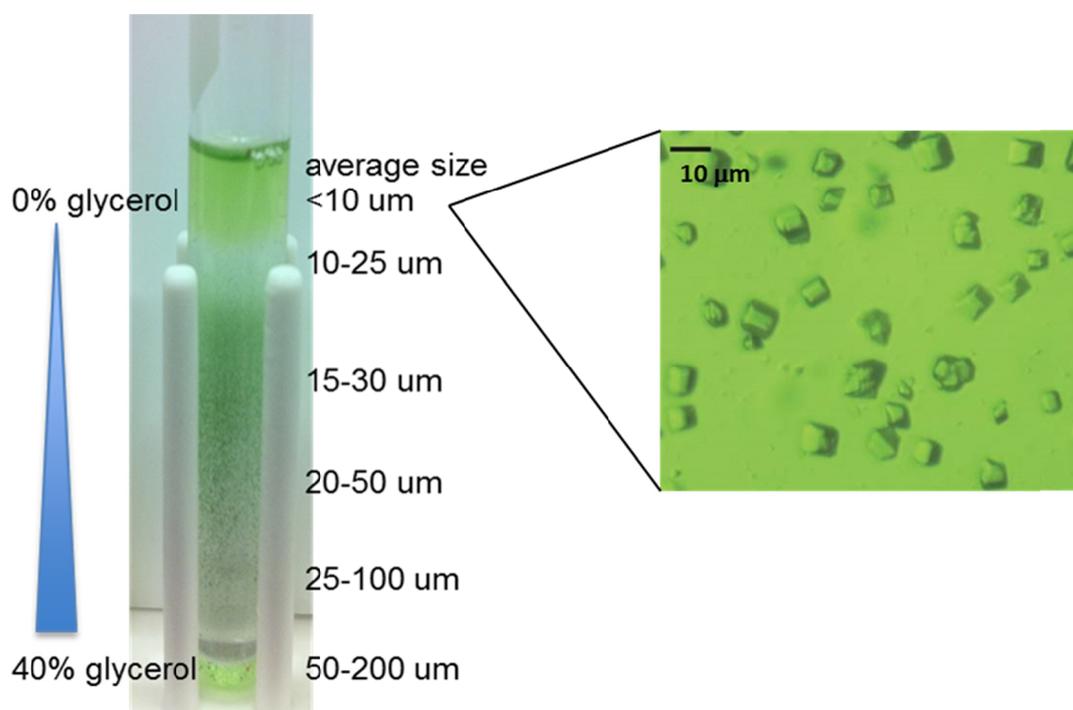


Figure 4-2 Glycerol gradient for size separation of dPSIIcc microcrystals

Microcrystals of uniform size ranges as obtained with a glycerol gradient. An example for the average size distribution is shown on the left side of the figure (light microscope image with green filter). The black bar indicates 10 μ m.

4.3 Room temperature femtosecond X-ray diffraction of dPSIIcc microcrystals

With the experimental setup and the microcrystal protocol as described before, it was accomplished to perform first fs XRD measurements of dPSIIcc at RT at the CXI instrument of LCLS, using the single-shot approach. The PSII microcrystals (Figure 4-3 a) were injected into the interaction region via a $< 10 \mu\text{m}$ liquid microjet exiting a silica capillary (100 μm inner diameter) using a potential of 2.1-2.5 kV between capillary exit and counter electrode (7 mm away). The crystal suspension flowed with 2.5-3.2 $\mu\text{l}/\text{min}$ and an applied back pressure of 15-20 psi. The X-rays hit the crystals 50-100 μm away from the capillary exit, exposing the crystal suspension to vacuum for fractions of a second. A single shot diffraction pattern of a dPSIIcc microcrystal (Figure 4-3 b) exhibits Bragg spots up to 5.4 \AA resolution (Figure 4-3 c). The Bragg spots are remarkably sharp and small, spreading only over a few pixels. A probable reasons for this is a combination of low crystal mosaicity and a pixel-array detector that provides an extremely narrow point-spread function (150) in combination with the fact that only still images and no rotation images are measured in the fs XRD experiments. The dose limit for conventional cryo-cooled (100-150 K) XRD studies of protein crystals at SR sources is around $2\text{-}3 \times 10^7$ Gy (Henderson limit (125)/ Garman limit (126)), previous SR studies of PSII crystals used doses below this value between 1×10^6 and 1×10^7 Gy, which corresponds to 5 - 40 absorbed photons per unit cell. For comparison, the flux at CXI is located between 3 and 5×10^{11} photons per shot at 9 keV and a beam focus of 1.5 μm ($\pm 30\%$) full width at half maximum at the interaction region with the use of Kirkpatrick-Beaz mirrors (149). Here the applied dose was around 2×10^8 Gy, which corresponds to about 1,440 absorbed photons per unit cell, being one order of magnitude higher than the Henderson/ Garman limit and ca. two orders of magnitude higher than the dose applied in SR based PSII XRD experiments. The measurements, additionally carried out at RT, could only be conducted in this way, as X-ray pulses below 50 fs outrun X-ray damage and the Coulomb explosion (134, 183). (The Coulomb explosion is the effect of chemical bond breakage during the pulse and the complete vaporization of the sample as the temperature rises to over 500, 000 K (184).) The effect of pulse length on diffraction intensity at LCLS was studied by Barty et al., using PSI nanocrystals (184). For pulses longer than 70 fs molecular disorder was observed, but it was still possible to

collect interpretable diffraction data. This implies that most of the diffraction signal is produced in the beginning of the pulse and the later disorder only increases the background (184). Further specific radiation damage and concomitant temperature dependence resulting from radical migration are no limiting issue for fs XRD.

Data were obtained in ca 4.45 h corresponding to almost 2 million shots. A strong fluctuation of diffraction intensities was observed, due to several factors such as the microcrystal quality and their orientation, the size of the hit crystal volume and variations of the beam intensity due to the nature of the LCLS X-ray pulses. All shots were initially screened for crystal diffraction and yielded in a total of 113,632 diffraction patterns which corresponds to 5.7 % of all shots. A hit was classified as a diffraction pattern when 16 or more strong Bragg spots were obtained. A portion of 7,269 individual diffraction patterns corresponding to 0.4 % of all shots have been successfully indexed and used for the dataset. This resulted in a final dataset (PDB code 4FBY) with 98 % completeness and a resolution of 6.5 Å (82 % completeness in the highest resolution shell). Thus the experiment provided the first fs XFEL XRD data of dPSIIcc microcrystals at RT with 6.5 Å resolution in its dark adapted state S_1 and showed that the probe-before-destroy approach by the use of intense fs pulses coupled with SFX was successful. For data collection and refinement statistics see Table 4-1.

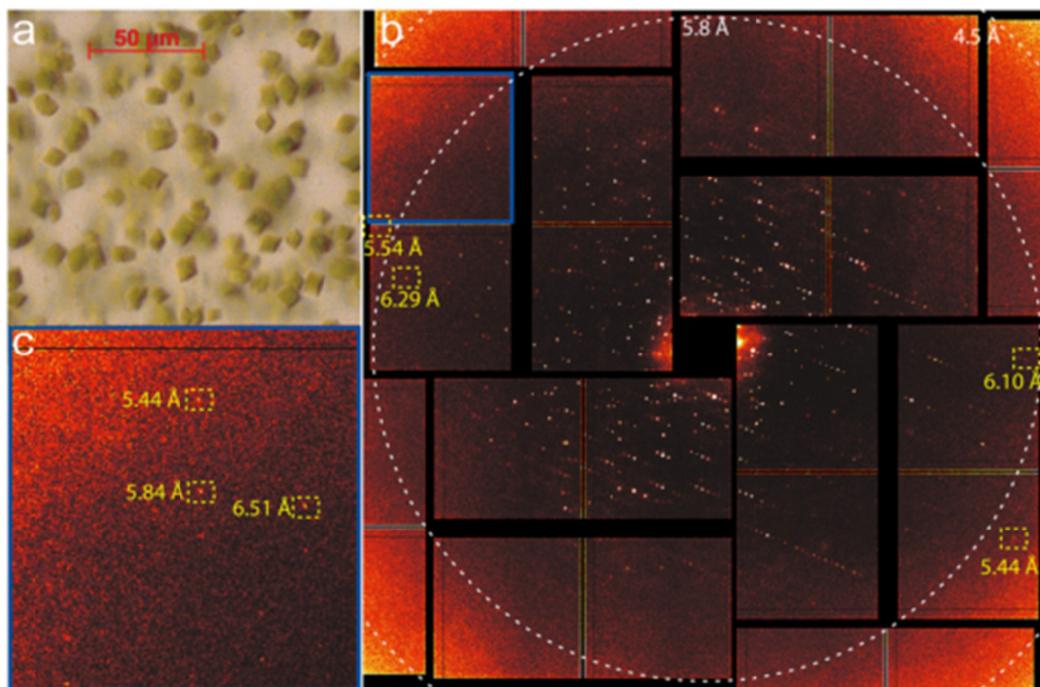


Figure 4-3 dPSIIcc microcrystals with XRD pattern

a) Light microscope image of dPSIIcc microcrystals used for XRD measurements (average size 10 μm , red bar indicates 50 μm). b) XRD pattern of dPSIIcc collected at CXI, with < 50 fs pulse duration and a flux of 3.4×10^{11} photons/pulse at 9 keV. Encircled Bragg spots with resolutions are given in \AA . Resolution at the edge of the selected area is indicated by a white dashed circle. (The background was removed by subtraction of the average image of 1052 misses before and after recording crystal diffraction). c) Enlargement of the blue box of the diffraction pattern in b, showing the highest resolution spots that have been obtained. Figure taken from (185), copyright 2012, National Academy of Sciences, USA.

Serial femtosecond X-ray diffraction and X-ray emission spectroscopy of dPSIIcc microcrystals

Resolution range (Å)	85.89–6.56 (6.79–6.56)
Space group	P2 ₁ 2 ₁ 2 ₁
Unit cell	130.8 (±3.3) 227.8 (±2.7) 308.6 (±3.8)
	90 90 90
Total reflections	873,209
Unique reflections	17,962 (1,446)
Multiplicity	26 (2.8)
Completeness (%)	98.1 (81.8)
Mean I/sigma (I)	16.9 (4.8)
R _{work}	0.366 (0.447)
R _{free}	0.385 (0.448)
Number of atoms	50,232
Macromolecules	41,052
Ligands	9,180
Protein residues	5,270
rms (bonds, Å)	0.007
rms (angles, °)	1.48
Ramachandran favored (%)	87
Ramachandran outliers (%)	2.2
Clashscore	37.1
Average B-factor	150.2
Macromolecules	148.4

Numbers in parentheses refer to highest resolution shell except for unit cell, where standard deviation for a, b, c are given in parentheses.

Table 4-1 Data collection and refinement statistics

Taken from (185), copyright 2012, National Academy of Sciences, USA.

The dPSIIcc microcrystals belong to the space group P2₁2₁2₁ and contain 4 dimers per unit cell, with cell constants $a = 130.78 \text{ \AA}$, $b = 227.76 \text{ \AA}$, $c = 308.63 \text{ \AA}$. Unit cell dimensions showed standard deviations of 2.5 % for the a -axis and 1 % for the b - and c -axes. They are comparable within 1-2 % with SR XRD data of dPSIIcc at 2.9 Å resolution (23), but differ from dehydrated dPSIIcc crystals at 1.9 Å resolution (25) that show a c -axis contraction of 20 Å (ca 7 % deviation). The obtained dataset was computed (as described in Chapter 2.2.14, page 58), and shows the electron density map of PSII in its dark stable state S₁ (Figure 4-4). The electron density map of dPSIIcc at 6.5 Å resolution, is isomorphous to the 2.9 Å resolution map of dPSIIcc published earlier (23). A view of the entire map ($2mF_0 - DF_C$), contoured at 1σ level is shown in Figure 4-4 a (blue mesh), all 36 TMHs per monomer are present as visualized in cartoon mode in yellow. Only TMH PsbY shows weaker density than the other 11 small intrinsic TMHs. This subunit is absent in the structures of dPSIIcc at 3.5 Å (132) and 1.9 Å (25) resolution and is claimed to be weakly bound to the complex. The large extrinsic features at the luminal side of the complex correspond

in part to the luminal protrusions of subunits D1, D2, CP43 and CP47 and to the three extrinsic subunits PsbO, PsbU and PsbV. At the position of the Mn-cluster at the luminal side of subunit D1 a positive peak in the refined omit map (mFo-DFc, at 3σ level, as green mesh in Figure 4-4 b) was observed. The Mn and Ca atoms were omitted from the phasing model, which means that the observed electron density can be taken as an experimental evidence for the presence of the Mn-cluster. The resolution did not allow for a more detailed structural picture of the Mn-cluster, but the observed electron density as compared to SR-based XRD of dPSIIcc excludes a dislocation of the Mn-cluster. The nonheme Fe is located at the acceptor side between the Q_A and Q_B site of subunits D2 and D1, respectively. A difference peak was found in the mFo-DFc map at this position, when Fe was omitted from the initial phasing model and confirms the presence of the nonheme iron in the dPSIIcc XRD data obtained at CXI (Figure 4-4 c). It was further possible to identify electron density for the Chls bound to the subunits D1, D2, CP43 and CP47. After omitting the electron density of the Chls at the expected locations, positive density was obtained in the difference map corresponding to the Chla molecules (Figure 4-4 d shows two RC Chls). However, at this resolution it was not possible to reveal the flexible phytol chains of the Chls. For direct comparison of SR and LCLS XRD data of dPSIIcc, the 2.9 Å resolution map was truncated to 6.5 Å resolution (Figure 4-5 a, b). This allowed stating that within the obtained resolution very similar TMH orientations and structures of all expected subunits and cofactors are obtained in the two maps and no deviations in the more flexible extrinsic luminal region were visible. Slight differences may be due to different data processing of the LCLS data, which uses the partial reflections contrary to SR data, as well as the lower signal produced by microcrystals at 6.5 Å, which leads to a low signal-to-noise levels at the resolution. Thus, although only a limited number of surface residues are engaged in the crystal contacts no differences in loop flexibility were found when comparing RT and cryogenic XRD data. Further the cofactor integrity was retained and no dislocation of the Mn-cluster was found despite the intense fs pulses of the LCLS. A direct comparison of the electron density of the Mn-cluster is given for both structures in Figure 4-5 c, d.

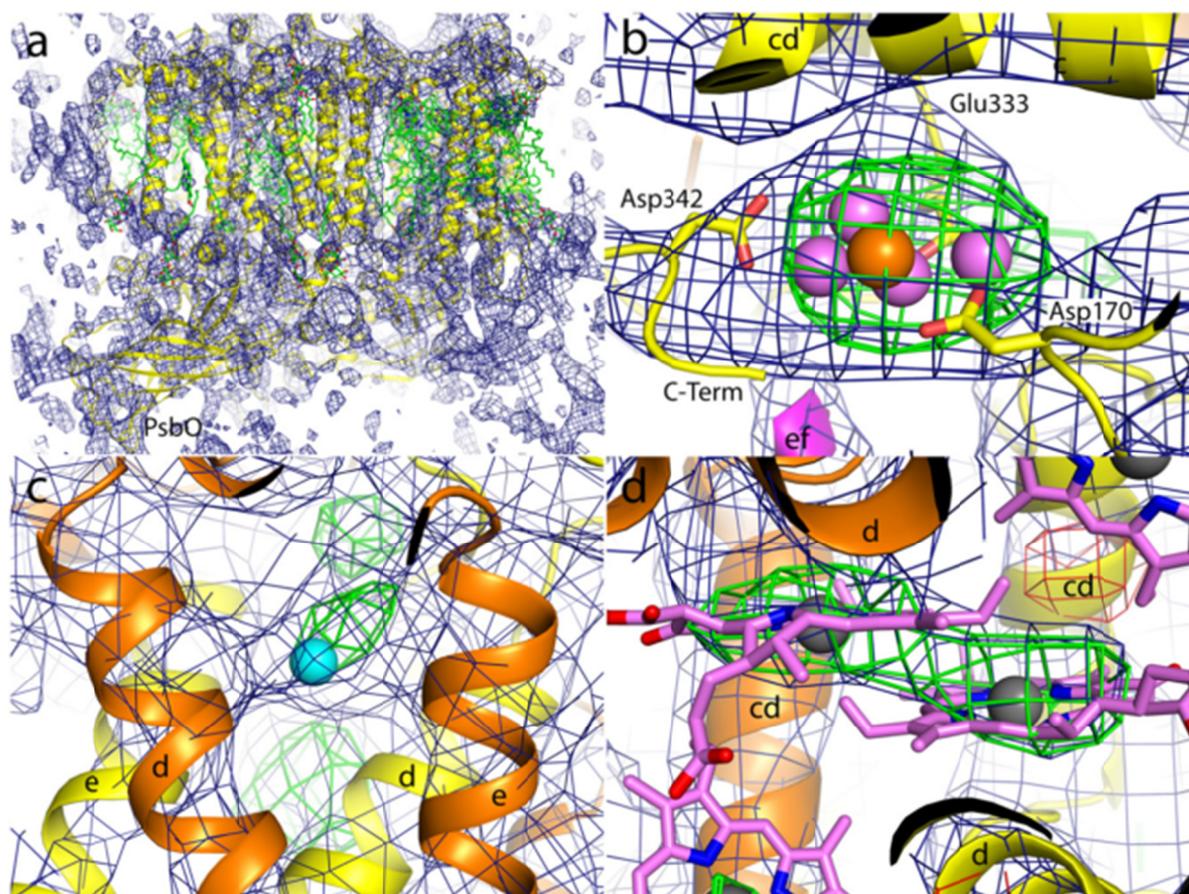


Figure 4-4 Electron density maps of dPSIIcc microcrystals from fs XRD at CXI

The $2mF_0-DF_C$ map shows electron density in blue mesh, the mF_0-DF_C omit map as green mesh (positive electron density) and red mesh (negative electron density). a) Electron density map of dPSIIcc at 6.5 Å resolution, 1 σ level. View along the membrane plane, cytoplasmic on top and luminal side on the bottom. One monomer of dPSII is shown in cartoon mode (yellow), cofactors in stick mode (green). For orientation subunit PsbO at the luminal side is labelled. b) Region around the OEC contoured at 1 σ , omit map at $\pm 3 \sigma$. Subunits in cartoon mode, D1 (yellow), CP43 (magenta), helices as indicated and three direct ligands to the OEC (Asp170, Asp342, Glu333) as labelled. The located Mn (purple) and Ca (orange) superimposed from 2.9 Å resolution dPSIIcc. c) Electron density at the nonheme Fe (cyan sphere), subunits D1 (yellow) and D2 (orange) with helices labelled. Map contoured at 1 σ , omit maps at 2.5 σ . d) Region around the two central Chls of the RC, subunits D1 (yellow) and D2 (orange) with helices labelled. Chls in stick mode (purple) with central Mg²⁺ ions as grey spheres, electron density map contoured at 0.8 σ level, omit maps at $\pm 2.5 \sigma$. Figure taken from (185), copyright 2012, National Academy of Sciences, USA.

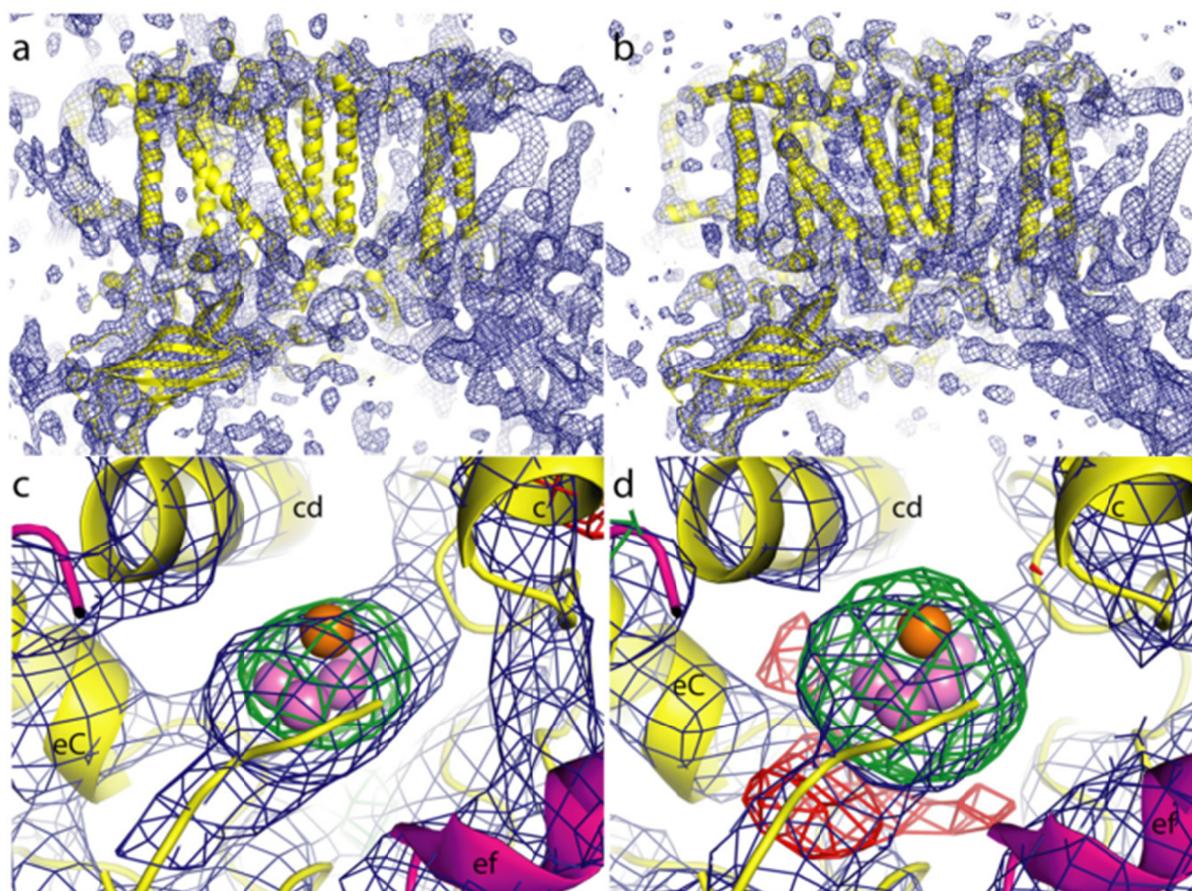


Figure 4-5 Comparison of electron density of dPSIIcc obtained from fs XRD and SR XRD

Electron density (blue mesh) of a) the CXI data of dPSIIcc at 6.5 Å resolution is compared with b) the SR data of dPSIIcc at 2.9 Å resolution truncated to 6.5 Å resolution. One monomer of dPSIIcc is shown in cartoon mode (yellow), view along the membrane plane $2mF_o-DF_c$ contoured at 1σ level. Electron density in the region of the Mn_4Ca -cluster: c) CXI data and b) the truncated SR data. Protein shown in cartoon mode, D1 (yellow), CP43 (magenta) with helices labelled. Mn as purple spheres and Ca as orange sphere with $2mF_o-DF_c$ contoured at 1σ level (blue mesh) and the omit map mF_o-DF_c at $\pm 3 \sigma$ with positive electron density (green mesh) and negative electron density (red mesh). Figure taken from (185), copyright 2012, National Academy of Sciences, USA.

4.4 Simultaneous fs XRD and XES measurements of dPSIIcc microcrystals

After it was accomplished to measure first fs XRD of dPSIIcc microcrystals at RT without radiation damage, the next step was to combine XRD with the complementary method of XES and conduct both measurements simultaneously. XES can provide information on the oxidation states of the Mn_4Ca -cluster, not accessible by XRD data alone. In addition, data from the dark and the S_2 state were collected. For this approach, dPSIIcc microcrystals equilibrated in the dark stable

Serial femtosecond X-ray diffraction and X-ray emission spectroscopy of dPSIIcc microcrystals

state S_1 , were excited to the S_2 state using a visible laser pump (at $\lambda = 527$ nm) and simultaneously XES and XRD data were collected. XES data were recorded at excitation energy of 7 keV. This energy was chosen, due to the higher cross section for the Mn transition when exciting close to the Mn absorption edge. Besides this effect, no differences were found between XES spectra either collected at 7 keV or 9.5 keV. XRD was measured either at 7 keV or at 9.5 keV excitation energies and no difference in diffraction quality was observed between these two. The schematic setup is shown and described in Figure 4-6.

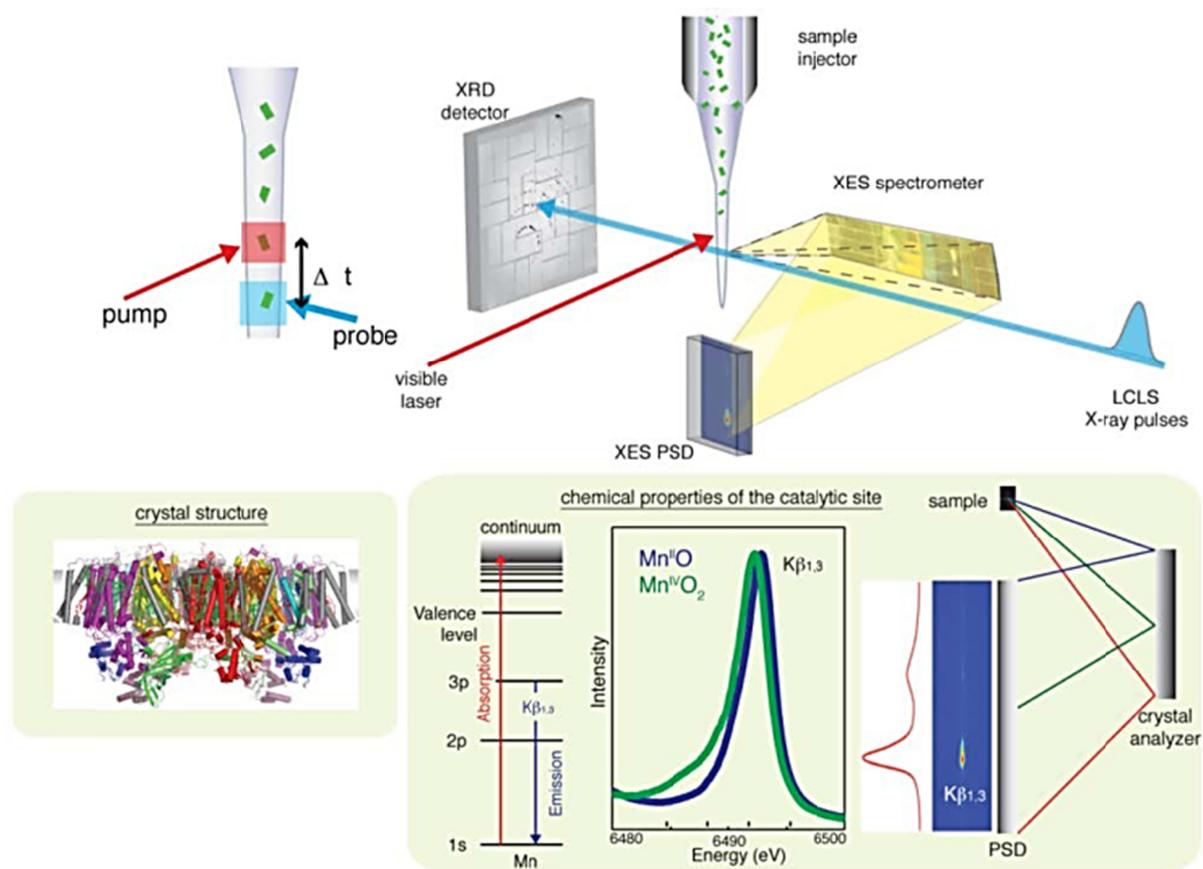


Figure 4-6 Setup of simultaneous XRD and XES with the pump-probe illumination

The sample injector focuses the crystal suspension into an electric field focused microjet that gets pumped by the visible laser (advancement to S_2 state) and probed by the X-ray laser. XRD data are collected by the XRD detector; XES data from the same crystal are collected ca 90° to the beam via a multicrystal XES spectrometer and a position sensitive detector (PSD). A Nd-YLF laser (527 nm) illuminates the microcrystals. At the left side the timing protocol is shown, consisting of the fixed time of flight Δt between the optical laser pump (red) and the X-ray laser probe (blue). The complementary methods XRD (bottom left), providing the crystal structure, and XES (bottom right) providing chemical properties of the catalytic site are shown. The energy level diagram for XES, the Mn^{II} and Mn^{IV} oxide $K\beta_{1,3}$ spectra and a scheme of the energy dispersive spectrometer are shown. Figure taken from (186), reprinted with permission from AAAS.

Fs XRD measurements of microcrystals were performed as described in Chapter 4.3, XES data (Mn $K\beta_{1,3}$ spectra) were collected simultaneous from the same sample with an energy dispersive spectrometer at approximately 90° to the beam direction with a small Cornell-SLAC Pixel Array Detector. The improved procedure for dPSIIcc microcrystals (Chapter 4.2) allowed collection of XRD data in the dark adapted S_1 state with diffraction spots up to 4.1 \AA and a diffraction data set was processed to 5.7 \AA resolution (Figure 4-7). For this data set 5 hours of run time and nearly 2,2 million X-ray shots with 90,000 potential hits (16 or more Bragg peaks) were collected, out of these 4,663 were indexed and integrated to result in the final dataset. Compared to the first data set at 6.5 \AA resolution the new dataset at 5.7 \AA resolution showed a more detailed map and allowed a better tracing of the TMHs and the loop regions at the membrane extrinsic area of the complex. The density of the Mn-cluster is similar to the density obtained from SR data but is slightly more compact, but no further structural details can be discussed at this resolution. The $K\beta_{1,3}$ X-ray emission spectra collected simultaneous with XRD are shown in Figure 4-8 A, page 114. The spectra consist of ca 20,000 averaged shots, recorded at 7 keV and identified as crystal hits from the XRD data. Additional to dPSIIcc crystals, dPSIIcc solution in the dark state S_1 has been collected (8.9 mM Chl, 1 mM Mn, 375,000 individual shots). Both spectra match very well, which implies that the WOC is in the same high-valent state with $\text{Mn}_2^{\text{III}}\text{Mn}_2^{\text{IV}}$ in crystals and solution and the crystallization process did not change the native PSII S_1 state (Figure 4-8 B). The shape and energies of the spectra were compared with SR dPSIIcc solution data that have been collected at 8 K and RT. The RT SR spectrum shows a completely damaged (photo-reduced) PSII, with all manganese atoms reduced to Mn^{II} . The $K\beta_{1,3}$ peak is shifted to higher energy identical to the spectrum peak of MnCl_2 in aqueous solution that contains only Mn^{II} (Figure 4-8 C). In contrast an undamaged SR spectrum from an intact PSII S_1 state was collected at 8 K. The results verify that the fs X-ray pulses, under the presented conditions, can be used to collect X-ray emission spectra of the intact Mn_4Ca -cluster at RT. Thus, the XES data demonstrate that the fs XRD data have been obtained in the S_1 state with a completely undamaged Mn-cluster ($\text{Mn}_2^{\text{III}}\text{Mn}_2^{\text{IV}}$). This result was the prerequisite for the S state advancement of PSII in a controlled manner. The crystals were illuminated to advance the S state using a Nd:YLF laser at 527 nm and 150 ns pulse duration, with a delay time between the optical laser and the X-ray laser

of 0.4-0.5 s. The output of the fiber was set to 10 $\mu\text{J}/\text{pulse}$. The advancement of the S states was tested with an illumination setup, which was coupled to a membrane inlet mass spectrometer (MIMS) using H_2^{18}O -labeled water (96, 100, 187). This setup allowed analyzing the labeled O_2 production as a function of the number of flashes, and implied that a high S_2 population was achieved after one flash. With the same illumination setup at CXI, 380,000 shots were collected within 53 min. Out of these, 4300 indexable diffraction patterns were obtained. The final S_2 state dPSIIcc dataset resulted from 1850 diffraction patterns with a final resolution of 5.9 Å. The XES data of the S_2 state were collected in parallel with the XRD data from 362 illuminated microcrystals with incident energy of 7 keV. The fewer number of crystals recorded, resulted in a lower signal to noise (S/N) ratio of the XES S_2 state spectrum, but corresponds well with the S_1 state spectrum. The expected shift in the X-ray emission spectra between S_1 and S_2 of ca 60 meV (188) cannot be resolved in the present data and a better S/N ratio is required for the detection of this shift. However, the measurement demonstrated that the XES for the illuminated sample (S_2 state) differs from the damaged spectrum and the illumination setup or the X-ray laser did not photo-reduce the Mn_4CaO_5 -cluster. No significant differences have been revealed when comparing the XRD electron density maps of the S_1 and S_2 states. On the one hand it proves that the illumination protocol did not lead to changes of the crystal quality, on the other hand it can be stated that no large structural changes occur between the dark and the first illuminated state. Nevertheless, the 5.9 Å resolution did not allow to detect small structural changes during the S_1 to S_2 transition (changes in carboxylate and backbone vibration frequencies) as observed with infrared spectroscopy (189, 190).

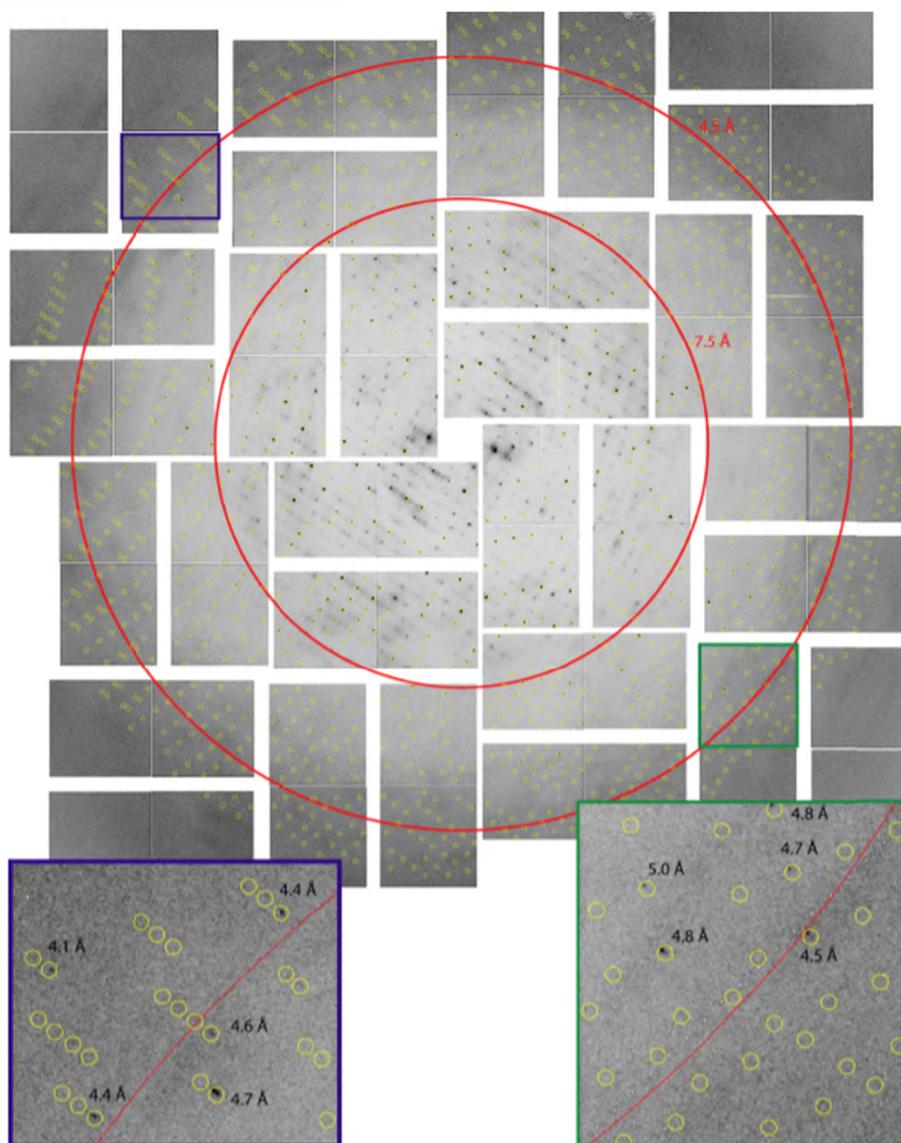


Figure 4-7 Diffraction image of dPSIIcc microcrystals

Best diffraction spots up to 4.1 Å resolution, the resolution shells indicated as red rings. Two enlarged views, upper left (blue frame) and lower right (green frame) are shown with predicted spot positions in yellow and resolution of selected spots as indicated. Taken from (191), reprinted with permission from AAAS.

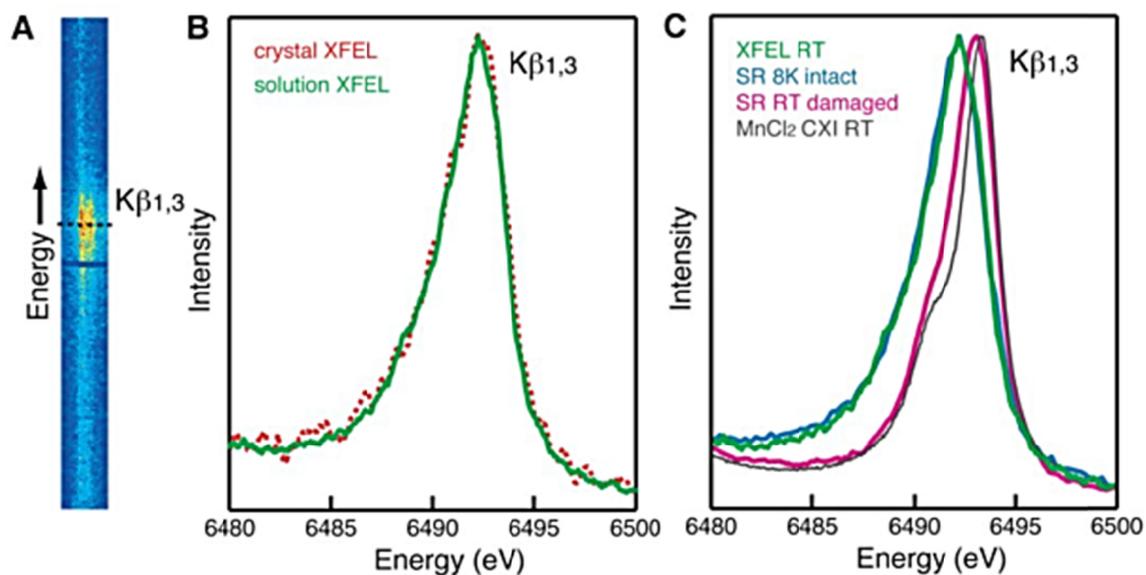


Figure 4-8 X-ray emission spectra of dPSIIcc

A) The 2D $K\beta_{1,3}$ X-ray emission spectra of dPSIIcc microcrystals recorded at the CXI endstation, integration along the horizontal axis results in B) X-ray emission spectra of PSII microcrystals (red) and PSII solution (green) in the S_1 state. C) Comparison of X-ray emission spectra of PSII solutions with intact S_1 state with the XFEL at RT (green) and with low dose SR at 8K (blue) and damaged PSII using SR at RT (pink). The spectrum of $MnCl_2$ (grey) collected at RT at the CXI endstation shows a spectrum with a peak position similar to the peak position found for the photodamaged Mn^{II} of PSII. Taken from (186), reprinted with permission from AAAS.

4.5 Summary

The method of serial fs XRD and simultaneous XES using an XFEL in the probe-before-destroy approach was established for dPSIIcc microcrystals. The ultra-bright and ultra-short X-ray pulses allowed collecting XRD data of the intact Mn_4CaO_5 -cluster without radiation damage at RT. A new delivery system using an electrospun microjet allowed transportation of microcrystals to the interaction region and measurement with lower flow rate, thus reduced sample consumption as compared to earlier SFX setups. A protocol for dPSIIcc microcrystals was established and stepwise improved. Milder handling of the fragile microcrystal during preparation and delivery to the interaction point of the measurements gained XRD datasets of the dark adapted PSII S_1 state at an improved resolution of 5.7 Å resolution (first dataset at 6.5 Å resolution). The XFEL PSII electron density map can be compared to the SR PSII electron density map truncated to the same resolutions. A negative impact of highly brilliant X-ray pulses of the XFEL on the crystal integrity could be excluded as no dislocation of TMHs, cofactors or the Mn_4CaO_5 cluster was obtained. A further control of the undamaged PSII structure was provided with simultaneous XES measurements. Comparison of XFEL XES of PSII with measurements of MnCl_2 solutions containing Mn^{II} , as well as photo damaged SR PSII XES spectra allowed stating that the intact Mn_4CaO_5 -cluster was obtained for all measurements conducted with dPSIIcc microcrystals. Additionally X-ray emission spectra of the intact S_1 state have been collected. An optical illumination pump-probe setup, designed to advance the microcrystals to the higher S states was successfully introduced. Thus, X-ray emission spectra of PSII microcrystals have further been recorded for the first illuminated S_2 state. Differences between the S_1 to the S_2 state have not been observed due to the low S/N ratio, but major differences of the local geometry can be excluded, as well as formation of Mn^{II} . The XRD PSII dataset of the S_2 state was successfully obtained in a completely intact state with a resolution of 5.9 Å. The here presented work is a first crucial step towards the unravelling of the catalytic S-state cycle.

5 Outlook

Even though improvement of dPSIIcc microcrystal resolution has been made after each beamtime at LCLS, the highest resolution diffraction peaks of LCLS XRD of PSII microcrystals were obtained at a limited resolution when compared to SR XRD of crystals of sizes around 300-600 μm . Effects of the used photon energy, the beam intensity or the experimental geometry could be excluded. One thus has to state that PSII microcrystal (10-50 μm) diffraction at an XFEL is lower when compared to PSII crystals >300 μm at a SR source. Several factors can be discussed for reduction in diffraction quality (PSII homogeneity, crystal size, setup, delivery process). One important factor may be the flexibility of proteins within the crystal lattice when RT measurements are conducted in a liquid jet in comparison to cryo-cooled, frozen SR measurements where the protein flexibility is reduced. One possibility of improvement in resolution is provided with dehydration of PSII crystals, reducing this flexibility. A dehydration procedure also led to the highly improved dPSIIcc structure at 1.9 \AA resolution (25). However, a key step of the dehydration procedure is believed to be conducted by introduction of a second detergent molecule that destabilizes the detergent belts and allows for a tighter packing not possible for PSII co-crystallized with the detergent βDM . As described in Chapter 3, the detergent C_{12}E_8 allowed for a drastic dehydration and the possibility to extract the detergent from the crystals concomitant with a jump in resolution. These crystals might provide an improvement of PSII diffraction quality in the microcrystal size region for future experiments at LCLS. A microcrystallization protocol is under development and the required setup will be adjusted for measurements of dehydrated microcrystals. Furthermore studies are ongoing to advance PSII microcrystals to the higher S states (S_3 and S_4). This, in combination with higher diffracting crystals will give the ultimate insight into the mystery of oxidative water splitting at the catalytic site of PSII.

Figures and Tables

Figures

Figure 1-1 The light absorbing pigments of cyanobacteria	3
Figure 1-2 Model of a tricylindrical hemidiscoidal phycobilisome	3
Figure 1-3 The light absorbing pigments of cyanobacteria	4
Figure 1-4 Schematic side view of a thylakoid membrane with incorporated integral membrane protein complexes of the photosynthetic electron transport chain	6
Figure 1-5 Cyanobacterial PSII arrangement in the thylakoid membrane and PSII double dimers.....	8
Figure 1-6 Z-Scheme of the oxygenic photosynthetic light reactions	11
Figure 1-7 The protein subunit composition of dPSIIcc.....	17
Figure 1-8 Arrangement of the redox-active cofactors of the PSII reaction center	21
Figure 1-9 Integral lipids of dPSIIcc at 2.9 Å resolution	25
Figure 1-10 Structure of integral lipids of PSII.....	26
Figure 1-11 Detergent molecules found in dPSIIcc structures	26
Figure 1-12 WOC and OEC as derived from 1.9 Å resolution crystal structure of dPSIIcc....	29
Figure 1-13 S-Cycle of water oxidation	30
Figure 1-14 Possible pathways for O-O bond formation	32
Figure 1-15 Comparison of Cl ⁻ binding sites in the vicinity of the Mn ₄ CaO ₅ -cluster.....	34
Figure 1-16 Additional Ca ²⁺ and Cl ⁻ binding sites in dPSIIcc.....	35
Figure 1-17 Schematic crystallization phase diagram.....	38
Figure 1-18 Crystal types of membrane proteins	40
Figure 1-19 Primary X-ray interaction processes with atoms of crystals and solvent	44
Figure 1-20 Increasing Mn(II) content in PSII caused by radiation damage	46
Figure 2-1 Schematic illustration of X-ray emission events.....	59
Figure 2-2 X-ray emission spectra of manganese.....	60
Figure 3-1 Structural comparison of detergent molecules and a PSII lipid	63
Figure 3-2 First anion exchange column	65
Figure 3-3 Second anion exchange column.....	65
Figure 3-4 Third strong anion exchange column.....	66
Figure 3-5 Size exclusion chromatography and BN-PAGE of βDM-PSIIcc standards and PSII samples	69
Figure 3-6 MALDI-MS spectra of standard dPSIIcc	70
Figure 3-7 MALDI-MS spectra of dPSIIcc with ATP-Synthase contamination	71

Figures and Tables

Figure 3-8 MALDI-MS spectra of dPSIIcc after chromatographic purification	71
Figure 3-9 MALDI-MS spectra of dPSIIcc crystals	72
Figure 3-10 dPSIIcc crystals	74
Figure 3-11 dPSIIcc structure at 2.44 Å resolution.....	77
Figure 3-12 Cofactors in dPSIIcc at 2.44 Å resolution	78
Figure 3-13 Mn ₄ Ca-cluster and detected water molecules.....	79
Figure 3-14 Integral lipids of dPSIIcc at 2.44 Å resolution	82
Figure 3-15 Crystal packing in the dPSIIcc unit cell	85
Figure 3-16 Protein rearrangement within C ₁₂ E8-dPSIIcc crystals.....	85
Figure 3-17 Crystal contacts in type I dPSIIcc crystals	87
Figure 3-18 Overlay of the X-ray structure of dPSIIcc and electron micrographs of PSII dimers in the thylakoid membrane	89
Figure 3-19 Overlay of the X-ray structure of dPSIIcc and electron micrographs of crystalline membrane arrays of PSII dimers.....	90
Figure 3-20 Influence of PEG 5000 MME on the CMC of the detergents C ₁₂ E ₈ and βDM.....	92
Figure 4-1 Setup of the nanoflow electrospun injector used for SFX at the CXI endstation ..	99
Figure 4-2 Glycerol gradient for size separation of dPSIIcc microcrystals	102
Figure 4-3 dPSIIcc microcrystals with XRD pattern	105
Figure 4-4 Electron density maps of dPSIIcc microcrystals from fs XRD at CXI.....	108
Figure 4-5 Comparison of electron density of dPSIIcc obtained from fs XRD and SR XRD	109
Figure 4-6 Setup of simultaneous XRD and XES with the pump-probe illumination.....	110
Figure 4-7 Diffraction image of dPSIIcc microcrystals.....	113
Figure 4-8 X-ray emission spectra of dPSIIcc	114

Tables

Table 1-1 Summary of the subunit and cofactor composition of dPSIIcc crystal structures... 36	36
Table 1-2 Lipid and detergent comparison of dPSIIcc crystal structures	42
Table 3-1 Table Oxygen evolution activity of PSII samples	67
Table 3-2 MALDI-MS masses of PSIIcc.....	72
Table 3-3 Data collection statistics and refinement statistics	76
Table 3-4 Lipid positions in the βDM-dPSIIcc, βDM/HTG-dPSIIcc and C ₁₂ E ₈ -dPSIIcc	81
Table 3-5 Lipids and UNLs of the 2.44 Å resolution dPSIIcc crystal structure	83
Table 4-1 Data collection and refinement statistics.....	106

References

1. Bacon Ke (2001) *Photosynthesis-Photobiochemistry and Photobiophysics* ed. Govindjee (Kluwer Academics Publisher).
2. Allen JP, Williams JC (2011) The evolutionary pathway from anoxygenic to oxygenic photosynthesis examined by comparison of the properties of photosystem II and bacterial reaction centers. *Photosynth Res* 107:59–69.
3. Blankenship RE, Hartman H (1998) The origin and evolution of oxygenic photosynthesis. *Trends Biochem Sci* 23:94–7.
4. Blankenship RE (2010) Early evolution of photosynthesis. *Plant Physiol* 154:434–8.
5. MacColl R (1998) Cyanobacterial phycobilisomes. *J Struct Biol* 124:311–34.
6. W. Sidler (2004) in *Advances in Photosynthesis and Respiration Volume 1*, ed Donald A. Bryant (Springer Netherlands), pp 139–216.
7. Deisenhofer J, Michel H (1989) The photosynthetic reaction centre from the purple bacterium. *J Mol Biol* 8:2149–2170.
8. Gould SB, Waller RF, McFadden GI (2008) Plastid evolution. *Annu Rev Plant Biol* 59:491–517.
9. Yamaoka T, Satoh K, Katoh S (1978) Photosynthetic activities of a thermophilic blue-green alga. *Plant and Cell Physiol* 19:943–954.
10. Nakamura Y et al. (2002) Complete genome structure of the thermophilic cyanobacterium *Thermosynechococcus elongatus* BP-1. *DNA Res* 9:135–48.
11. Sugiura M et al. (2004) Site-directed mutagenesis of *Thermosynechococcus elongatus* photosystem II: the O₂-evolving enzyme lacking the redox-active tyrosine D. *Biochemistry* 43:13549–63.
12. Vavilin D V (2004) Isolation of functional photosystem II core particles from the Cyanobacterium *synechocystis* sp. PCC 6803. *Methods Mol Biol* 274:37–47.
13. Austin JR, Staehelin LA (2011) Three-dimensional architecture of grana and stroma thylakoids of higher plants as determined by electron tomography. *Plant Physiol* 155:1601–11.
14. Bryant DA ed. (1994) *The Molecular Biology of Cyanobacteria* (Kluwer Academic Publishers).
15. Wada H, Murata N eds. (2009) *Lipids in Photosynthesis - Essential and Regulatory Functions* (Springer Netherlands).

References

16. Yokono M, Murakami A, Akimoto S (2011) Excitation energy transfer between photosystem II and photosystem I in red algae: larger amounts of phycobilisome enhance spillover. *Biochim Biophys Acta* 1807:847–53.
17. Folea IM, Zhang P, Aro E-M, Boekema EJ (2008) Domain organization of photosystem II in membranes of the cyanobacterium *Synechocystis* PCC6803 investigated by electron microscopy. *FEBS Lett* 582:1749–54.
18. Mörschel E, Schatz GH (1987) Correlation of photosystem-II complexes with exoplasmatic freeze-fracture particles of thylakoids of the cyanobacterium *Synechococcus* sp. *Planta* 172:145–54.
19. Loll B, Kern J, Saenger W, Zouni A, Biesiadka J (2005) Towards complete cofactor arrangement in the 3.0 Å resolution structure of photosystem II. *Nature* 438:1040–4.
20. Kurisu G, Zhang H, Smith JL, Cramer W a (2003) Structure of the cytochrome b_6f complex of oxygenic photosynthesis: tuning the cavity. *Science* 302:1009–14.
21. Deisenhofer J, Epp O, Miki K, Huber R, Michel H (1985) Structure of the protein subunits in the photosynthetic reaction center of *Rhodospseudomonas viridis* at 3 Å resolution. *Nature* 318:618–624
22. Zouni, A., Witt, H.-T., Kern, J., Fromme, P., Krauß, N., Saenger, W., and Orth P (2001) Crystal Structure of Photosystem II from *Synechococcus elongatus* 3.8 Å resolution. *Nature* 409:739–743.
23. Guskov A et al. (2009) Cyanobacterial photosystem II at 2.9-Å resolution and the role of quinones, lipids, channels and chloride. *Nat Struct Mol Biol* 16:334–342.
24. Broser M et al. (2010) Crystal structure of monomeric photosystem II from *Thermosynechococcus elongatus* at 3.6-Å resolution. *J Biol Chem* 285:26255–62.
25. Umena Y, Kawakami K, Shen J-R, Kamiya N (2011) Crystal structure of oxygen-evolving photosystem II at a resolution of 1.9 Å. *Nature* 473:55–60.
26. Piano D et al. (2010) Crystallization of the photosystem II core complex and its chlorophyll binding subunit CP43 from transplastomic plants of *Nicotiana tabacum*. *Photosynth Res* 106:221–6.
27. Pagliano C, Chimirri F, Saracco G, Marsano F, Barber J (2011) One-step isolation and biochemical characterization of a highly active plant PSII monomeric core. *Photosynth Res* 108:33–46.
28. Nickelsen J, Rengstl B (2013) Photosystem II Assembly: From Cyanobacteria to Plants. *Annu Rev Plant Biol* 64:609–35.

References

29. Lyon MK (1998) Multiple crystal types reveal photosystem II to be a dimer. *Biochim Biophys Acta* 1364:403–19.
30. Watanabe M, Iwai M, Narikawa R, Ikeuchi M (2009) Is the photosystem II complex a monomer or a dimer? *Plant Cell Physiol* 50:1674–80.
31. Takahashi T et al. (2009) Photosystem II complex in vivo is a monomer. *J Biol Chem* 284:15598–606.
32. Deisenhofer J, Epp O, Sinning I, Michel H (1995) Crystallographic refinement at 2.3 Å Resolution and Refined Model of the Photosynthetic Reaction Centre from *Rhodospseudomonas viridis*. *J Mol Biol* 246:429–57.
33. Jordan P et al. (2001) Three-dimensional structure of cyanobacterial photosystem I at 2.5 Å resolution. *Nature* 411:909–17.
34. Müh F, Zouni A (2013) The nonheme iron in photosystem II. *Photosynth Res* 116:295–314.
35. Raymond J, Blankenship RE (2004) The evolutionary development of the protein complement of photosystem 2. *Biochim Biophys Acta* 1655:133–9.
36. Krieger-Liszakay A (2005) Singlet oxygen production in photosynthesis. *J Exp Bot* 56:337–46.
37. Allen JF (2003) Botany. State transitions—a question of balance. *Science* 299:1530–2.
38. Aro EM, Virgin I, Andersson B (1993) Photoinhibition of Photosystem II. Inactivation, protein damage and turnover. *Biochim Biophys Acta* 1143:113–34.
39. Kato Y, Sakamoto W (2009) Protein quality control in chloroplasts: a current model of D1 protein degradation in the photosystem II repair cycle. *J Biochem* 146:463–9.
40. Nixon PJ, Michoux F, Yu J, Boehm M, Komenda J (2010) Recent advances in understanding the assembly and repair of photosystem II. *Ann Bot* 106:1–16.
41. Kós PB, Deák Z, Cheregi O, Vass I (2008) Differential regulation of psbA and psbD gene expression, and the role of the different D1 protein copies in the cyanobacterium *Thermosynechococcus elongatus* BP-1. *Biochim Biophys Acta* 1777:74–83.
42. Loll B et al. (2008) Modeling of variant copies of subunit D1 in the structure of photosystem II from *Thermosynechococcus elongatus*. *Biol Chem* 389:609–617.
43. Kawakami K et al. (2011) Roles of PsbI and PsbM in photosystem II dimer formation and stability studied by deletion mutagenesis and X-ray crystallography. *Biochim Biophys Acta* 1807:319–25.

References

44. Bentley FK, Luo H, Dilbeck P, Burnap RL, Eaton-rye JJ (2008) Effects of Inactivating psbM and psbT on Photodamage and Assembly of Photosystem II in *Synechocystis* sp PCC 6803. 11637–11646.
45. Kawakami K, Iwai M, Ikeuchi M, Kamiya N, Shen J-R (2007) Location of PsbY in oxygen-evolving photosystem II revealed by mutagenesis and X-ray crystallography. *FEBS Lett* 581:4983–7.
46. Kamiya N, Shen J-R (2003) Crystal structure of oxygen-evolving photosystem II from *Thermosynechococcus vulcanus* at 3.7-Å resolution. *Proc Natl Acad Sci U S A* 100:98–103.
47. Koua FHM, Umena Y, Kawakami K, Shen J-R (2013) Structure of Sr-substituted photosystem II at 2.1 Å resolution and its implications in the mechanism of water oxidation. *Proc Natl Acad Sci U S A* 110:3889–94.
48. Shi L-X, Hall M, Funk C, Schröder WP (2012) Photosystem II, a growing complex: updates on newly discovered components and low molecular mass proteins. *Biochim Biophys Acta* 1817:13–25.
49. Murray JW, Barber J (2006) Identification of a calcium-binding site in the PsbO protein of photosystem II. *Biochemistry* 45:4128–30.
50. Williamson AK (2008) Structural and functional aspects of the MSP (PsbO) and study of its differences in thermophilic versus mesophilic organisms. *Photosynth Res* 98:365–89.
51. Yi X, McChargue M, Laborde S, Frankel LK, Bricker TM (2005) The manganese-stabilizing protein is required for photosystem II assembly/stability and photoautotrophy in higher plants. *J Biol Chem* 280:16170–4.
52. Stewart AC, Ljungberg U, Åkerlund H-E, Andersson B (1985) Studies on the polypeptide composition of the cyanobacterial oxygen-evolving complex. *Biochim Biophys Acta - Bioenerg* 808:353–362.
53. Veerman J et al. (2005) The PsbU subunit of photosystem II stabilizes energy transfer and primary photochemistry in the phycobilisome-photosystem II assembly of *Synechocystis* sp. PCC 6803. *Biochemistry* 44:16939–48.
54. Guerrero F et al. (2011) A high redox potential form of cytochrome c550 in photosystem II from *Thermosynechococcus elongatus*. *J Biol Chem* 286:5985–94.
55. Roncel M, Kirilovsky D, Guerrero F, Serrano A, Ortega JM (2012) Photosynthetic cytochrome c550. *Biochim Biophys Acta* 1817:1152–63.
56. Mamedov F, Nowaczyk MM, Thapper A, Rögner M, Styring S (2007) Functional characterization of monomeric photosystem II core preparations from *Thermosynechococcus elongatus* with or without the Psb27 protein. *Biochemistry* 46:5542–51.

References

57. Roose JL, Wegener KM, Pakrasi HB (2007) The extrinsic proteins of Photosystem II. *Photosynth Res* 92:369–87.
58. Renger G (2008) in *Primary Process of Photosynthesis - Part 2*, ed Renger G (RCS Publishing), pp 237–290.
59. Cardona T, Sedoud A, Cox N, Rutherford a W (2012) Charge separation in photosystem II: a comparative and evolutionary overview. *Biochim Biophys Acta* 1817:26–43.
60. Scheer H (2008) in *Primary Process of Photosynthesis - Part 1*, ed Renger G (RCS Publishing), pp 101–149.
61. Renger G, Renger T (2008) Photosystem II: The machinery of photosynthetic water splitting. *Photosynth Res* 98:53–80.
62. Raszewski G, Renger T (2008) Light harvesting in photosystem II core complexes is limited by the transfer to the trap: can the core complex turn into a photoprotective mode? *J Am Chem Soc* 130:4431–46.
63. Müh F, Renger T, Zouni A (2008) Crystal structure of cyanobacterial photosystem II at 3.0 Å resolution: a closer look at the antenna system and the small membrane-intrinsic subunits. *Plant Physiol Biochem* 46:238–64.
64. Müh F, Glöckner C, Hellmich J, Zouni A (2012) Light-induced quinone reduction in photosystem II. *Biochim Biophys Acta* 1817:44–65.
65. Renger T, Schlodder E (2010) Primary photophysical processes in photosystem II: bridging the gap between crystal structure and optical spectra. *Chemphyschem* 11:1141–53.
66. Rappaport F, Diner B (2008) Primary photochemistry and energetics leading to the oxidation of the (Mn)₄Ca cluster and to the evolution of molecular oxygen in Photosystem II. *Coord Chem Rev* 252:259–272.
67. Hirschberg J, Chamovitz D (1994) in *The Molecular Biology of Cyanobacteria*, ed Bryant DA (Kluwer Academic Publishers), pp 559–579.
68. Pogson BJ, Rissler HM, Frank HA (2005) in *Photosystem II - The light-driven Water:Plastoquinone Oxidoreductase*, eds Wydrzynski TJ, Satoh K (Springer), pp 515–537.
69. Telfer A (2002) What is β-carotene doing in the photosystem II reaction centre? *Philos Trans R Soc Lond B Biol Sci* 357:1431–39; discussion 1439–40, 1469–70.
70. Martinez-Junza V et al. (2008) Triplet Photoprotection by Carotenoid in Intact Photosystem II Cores. *Photosynth Energy from Sun*:137–140.

References

71. Brose K, Zouni A, Müh F, Mroginski MA, Maultzsch J (2013) Simulations of the polarisation-dependent Raman intensity of β -carotene in photosystem II crystals. *Chem Phys* 418:65–73.
72. Hasegawa K, Noguchi T (2012) Molecular interactions of the quinone electron acceptors Q_A , Q_B , and Q_C in photosystem II as studied by the fragment molecular orbital method. *Photosynth Res*.
73. Ishikita H, Hasegawa K, Noguchi T (2011) How Does the Q_B site influence propagate to the Q_A site in Photosystem II? *Biochemistry* 50:5436–5442.
74. Saito K, Rutherford a W, Ishikita H (2013) Mechanism of proton-coupled quinone reduction in Photosystem II. *Proc Natl Acad Sci U S A* 110:954–9.
75. Kern J, Zouni A, Guskov A, Krauß N (2009) in *Lipids in Photosynthesis - Essential and Regulatory Functions*, eds Wada H, Murata N (Springer), pp 203–242.
76. Sakurai I et al. (2006) Lipids in oxygen-evolving photosystem II complexes of cyanobacteria and higher plants. *J Biochem* 140:201–9.
77. Mizusawa N, Wada H (2012) The role of lipids in photosystem II. *Biochim Biophys Acta* 1817:194–208.
78. Kern J, Guskov A (2011) Lipids in photosystem II: multifunctional cofactors. *J Photochem Photobiol B* 104:19–34.
79. Leng J, Sakurai I, Wada H, Shen J-R (2008) Effects of phospholipase and lipase treatments on photosystem II core dimer from a thermophilic cyanobacterium. *Photosynth Res* 98:469–78.
80. Sakurai I, Hagio M, Gombos Z (2003) Requirement of phosphatidylglycerol for maintenance of photosynthetic machinery. *Plant Physiol* 133:1376–1384.
81. Gabdulkhakov A et al. (2009) Probing the accessibility of the Mn_4Ca cluster in photosystem II: channels calculation, noble gas derivatization, and cocrystallization with DMSO. *Structure* 17:1223–34.
82. Findlay JBC, Pifat G, Kinnunen PKJ, Marsh D, Páli T (2006) Lipid conformation in crystalline bilayers and in crystals of transmembrane proteins. *Chem Phys Lipids* 141:48–65.
83. Jones MR (2007) Lipids in photosynthetic reaction centres: structural roles and functional holes. *Prog Lipid Res* 46:56–87.
84. Grundmeier A, Dau H (2012) Structural models of the manganese complex of photosystem II and mechanistic implications. *Biochim Biophys Acta* 1817:88–105.

References

85. Kawakami K, Umena Y, Kamiya N, Shen J-R (2011) Structure of the catalytic, inorganic core of oxygen-evolving photosystem II at 1.9 Å resolution. *J Photochem Photobiol B* 104:9–18.
86. Vinyard DJ, Ananyev GM, Charles Dismukes G (2013) Photosystem II: The Reaction Center of Oxygenic Photosynthesis. *Ann Rev Biochem* 82:577–606.
87. Joliot P, Barbieri G, Chabaud R (1969) Un nouveau modèle des centres photochimiques du système II (in french). *Photochem Photobiol* 10:309–329.
88. Kok B, Forbush B, McGloin M (1970) Cooperation of charges in photosynthetic O₂ evolution-I. A linear four step mechanism *Photochem Photobiol* 6:457–475.
89. Sartorel A, Bonchio M, Campagna S, Scandola F (2013) Tetrametallic molecular catalysts for photochemical water oxidation. *Chem Soc Rev* 42:2262–80.
90. Tommos C, Babcock GT (2000) Proton and hydrogen currents in photosynthetic water oxidation. *Biochim Biophys Acta* 1458:199–219.
91. Renger G (2004) Coupling of electron and proton transfer in oxidative water cleavage in photosynthesis. *Biochim Biophys Acta* 1655:195–204.
92. Kern J, Renger G (2007) Photosystem II: structure and mechanism of the water:plastoquinone oxidoreductase. *Photosynth Res* 94:183–202.
93. Razeghifard MR, Pace RJ (1999) EPR kinetic studies of oxygen release in thylakoids and PSII membranes: a kinetic intermediate in the S₃ to S₀ transition. *Biochemistry* 38:1252–7.
94. Clausen J, Junge W (2005) Search for intermediates of photosynthetic water oxidation. *Photosynth Res* 84:339–45.
95. Dau H, Haumann M (2007) Eight steps preceding O-O bond formation in oxygenic photosynthesis—a basic reaction cycle of the Photosystem II manganese complex. *Biochim Biophys Acta* 1767:472–83.
96. Shevela D, Beckmann K, Clausen J, Junge W, Messinger J (2011) Membrane-inlet mass spectrometry reveals a high driving force for oxygen production by photosystem II. *Proc Natl Acad Sci U S A* 108(9):3602-7
97. Brudvig GW (2008) Water oxidation chemistry of photosystem II. *Philos Trans R Soc Lond B Biol Sci* 363:1211–8; discussion 1218–9.
98. Renger G (2011) Light induced oxidative water splitting in photosynthesis: energetics, kinetics and mechanism. *J Photochem Photobiol B* 104:35–43.
99. Rapatskiy L et al. (2012) Detection of the water-binding sites of the oxygen-evolving complex of Photosystem II using W-band ¹⁷O electron-electron double resonance-detected NMR spectroscopy. *J Am Chem Soc* 134:16619–34.

References

100. Cox N, Messinger J (2013) Reflections on substrate water and dioxygen formation. *Biochim Biophys Acta* 8-9:1020–30.
101. Kawakami K, Umena Y, Kamiya N, Shen J-R (2009) Location of chloride and its possible functions in oxygen-evolving photosystem II revealed by X-ray crystallography. *Proc Natl Acad Sci U S A* 106:8567–72.
102. Murray JW et al. (2008) X-ray crystallography identifies two chloride binding sites in the oxygen evolving centre of Photosystem II. *Energy Environ Sci* 1:161.
103. Olesen K, Andréasson L-E (2003) The function of the chloride ion in photosynthetic oxygen evolution. *Biochemistry* 42:2025–35.
104. Ishida N et al. (2008) Biosynthetic exchange of bromide for chloride and strontium for calcium in the photosystem II oxygen-evolving enzymes. *J Biol Chem* 283:13330–40.
105. Popelková H, Yocum CF (2007) Current status of the role of Cl⁻ ion in the oxygen-evolving complex. *Photosynth Res* 93:111–21.
106. Broser M et al. (2011) Structural basis of cyanobacterial photosystem II Inhibition by the herbicide terbutryn. *J Biol Chem* 286:15964–72.
107. Lindberg K, Andréasson LE (1996) A one-site, two-state model for the binding of anions in photosystem II. *Biochemistry* 35:14259–67.
108. Loll B et al. (2005) Thermostability and Ca²⁺ binding properties of wild type and heterologously expressed PsbO protein from cyanobacterial photosystem II. *Biochemistry* 44:4691–8.
109. Chayen NE, Saridakis E (2008) Protein crystallization: from purified protein to diffraction-quality crystal. *Nat Methods* 5:147–53.
110. Li M, Chang W (2009) Protein crystallization. *Photosynth Res* 102:223–9.
111. Kang HJ, Lee C, Drew D (2013) Breaking the barriers in membrane protein crystallography. *Int J Biochem Cell Biol* 45:636–44.
112. Bergfors T (2003) Seeds to crystals. *J Struct Biol* 142:66–76.
113. Zhang Y, Cremer PS (2006) Interactions between macromolecules and ions: The Hofmeister series. *Curr Opin Chem Biol* 10:658–63.
114. Rayment I (2002) Small-Scale Batch Crystallization Ways & Means of Proteins Revisited: An Underutilized Way to Grow Large Protein Crystals. *Structure* 10:147–151.
115. Russo Krauss I, Merlino A, Vergara A, Sica F (2013) An overview of biological macromolecule crystallization. *Int J Mol Sci* 14:11643–91.

References

116. Garavito RM, Ferguson-Miller S (2001) Detergents as tools in membrane biochemistry. *J Biol Chem* 276:32403–6.
117. Maire M, Champeil P, Möller J V (2000) Interaction of membrane proteins and lipids with solubilizing detergents. *Biochim. Biophys. Acta* 1508:86–111.
118. Müh F, Zouni A (2005) Extinction coefficients and critical solubilisation concentrations of photosystems I and II from *Thermosynechococcus elongatus*. *Biochim Biophys Acta* 1708:219–28.
119. Hellmich J (2009) Kristallisation von Photosystem II aus dem Cyanobakterium *Thermosynechococcus elongatus* mit Zusatz von nativen Lipiden. (Diploma thesis, TU Berlin).
120. Kern J, Loll B, Lüneberg C (2005) Purification, characterisation and crystallisation of photosystem II from *Thermosynechococcus elongatus* cultivated in a new type of photobioreactor. *Biochim Biophys Acta* 1706:147–57.
121. Berthaud A, Manzi J, Pérez J, Mangenot S (2012) Modeling detergent organization around aquaporin-0 using small-angle X-ray scattering. *J Am Chem Soc* 134:10080–8.
122. Garman EF, Nave C (2009) Radiation damage in protein crystals examined under various conditions by different methods. *J Synchrotron Radiat* 16:129–32.
123. Garman EF (2010) Radiation damage in macromolecular crystallography: what is it and why should we care? *Acta Crystallogr D Biol Crystallogr* 66:339–51.
124. Ravelli RB, McSweeney SM (2000) The “fingerprint” that X-rays can leave on structures. *Structure* 8:315–28.
125. Henderson R (1990) Cryo-Protection of Protein Crystals against Radiation Damage in Electron and X-Ray Diffraction. *Proc R Soc B Biol Sci* 241:6–8.
126. Owen RL, Rudiño-Piñera E, Garman EF (2006) Experimental determination of the radiation dose limit for cryocooled protein crystals. *Proc Natl Acad Sci U S A* 103:4912–7.
127. Sliz P, Harrison SC, Rosenbaum G (2003) How does Radiation Damage in Protein Crystals Depend on X-Ray Dose? Notes from the Bench. *Structure* 11:13–19.
128. Weik M et al. (2000) Specific chemical and structural damage to proteins produced by synchrotron radiation. *Proc Natl Acad Sci U S A* 97:623–8.
129. Grabolle M, Haumann M, Müller C, Liebisch P, Dau H (2006) Rapid loss of structural motifs in the manganese complex of oxygenic photosynthesis by X-ray irradiation at 10–300 K. *J Biol Chem* 281:4580–8.

References

130. Davis KM, Kosheleva I, Henning RW, Seidler GT, Pushkar Y (2013) Kinetic modeling of the X-ray-induced damage to a metalloprotein. *J Phys Chem B* 117:9161–9.
131. Yano J et al. (2005) X-ray damage to the Mn₄Ca complex in single crystals of photosystem II: a case study for metalloprotein crystallography. *Proc Natl Acad Sci U S A* 102:12047–52.
132. Ferreira KN, Iverson TM, Maghlaoui K, Barber J, Iwata S (2004) Architecture of the photosynthetic oxygen-evolving center. *Science* 303:1831–8.
133. Glöckner C et al. (2013) Structural changes of the oxygen-evolving complex in photosystem II during the catalytic cycle. *J Biol Chem* 288:22607–20.
134. Neutze R, Wouts R, van der Spoel D, Weckert E, Hajdu J (2000) Potential for biomolecular imaging with femtosecond X-ray pulses. *Nature* 406:752–7.
135. Chapman HN et al. (2011) Femtosecond X-ray protein nanocrystallography. *Nature* 470:73–7.
136. Wittig I, Braun H-P, Schägger H (2006) Blue native PAGE. *Nat Protoc* 1:418–28.
137. Burkhardt A et al. (2012) Fast high-pressure freezing of protein crystals in their mother liquor. *Acta Crystallogr Sect F Struct Biol Cryst Commun* 68:495–500.
138. Burkhardt A et al. (2013) Structure determination from a single high-pressure-frozen virus crystal. *Acta Crystallogr D Biol Crystallogr* 69:308–12.
139. Mueller U et al. (2012) Facilities for macromolecular crystallography at the Helmholtz-Zentrum Berlin. *J Synchrotron Radiat* 19:442–9.
140. Sanchez-Weatherby J et al. (2009) Improving diffraction by humidity control: a novel device compatible with X-ray beamlines. *Acta Crystallogr D Biol Crystallogr* 65:1237–46.
141. Kabsch W (2010) XDS. *Acta Crystallogr D Biol Crystallogr* 66:125–32.
142. McCoy AJ et al. (2007) Phaser crystallographic software. *J Appl Crystallogr* 40:658–674.
143. Emsley P, Lohkamp B, Scott WG, Cowtan K (2010) Features and development of Coot. *Acta Crystallogr D Biol Crystallogr* 66:486–501.
144. Afonine P V et al. (2012) Towards automated crystallographic structure refinement with phenix.refine. *Acta Crystallogr D Biol Crystallogr* 68:352–67.
145. Chen VB et al. (2010) MolProbity: all-atom structure validation for macromolecular crystallography. *Acta Crystallogr D Biol Crystallogr* 66:12–21.

References

146. Moriarty NW, Grosse-Kunstleve RW, Adams PD (2009) electronic Ligand Builder and Optimization Workbench (eLBOW): a tool for ligand coordinate and restraint generation. *Acta Crystallogr D Biol Crystallogr* 65:1074–1080.
147. Winn MD et al. (2011) Overview of the CCP4 suite and current developments. *Acta Crystallogr D Biol Crystallogr* 67:235–42.
148. Abuin EB, Lissi EA, Aspée A, Gonzalez FD, Varas JM (1997) Fluorescence of 8-Anilino-naphthalene-1-sulfonate and Properties of Sodium Dodecyl Sulfate Micelles in Water–Urea Mixtures. *J Colloid Interface Sci* 186:332–338.
149. Siewert F et al. (2012) Ultra-precise characterization of LCLS hard X-ray focusing mirrors by high resolution slope measuring deflectometry. *Opt Express* 20:4525–36.
150. Koerner LJ, Philipp HT, Hromalik MS, Tate MW, Gruner SM (2009) X-ray tests of a Pixel Array Detector for coherent X-ray imaging at the Linac Coherent Light Source. *J Instrum* 4:P03001.
151. Paithankar KS, Owen RL, Garman EF (2009) Absorbed dose calculations for macromolecular crystals: improvements to RADDOS. *J Synchrotron Radiat* 16:152–62.
152. Zhang Z, Sauter NK, van den Bedem H, Snell G, Deacon AM (2006) Automated diffraction image analysis and spot searching for high-throughput crystal screening. *J Appl Crystallogr* 39:112–119.
153. Sauter NK, Grosse-Kunstleve RW, Adams PD (2004) Robust indexing for automatic data collection. *J Appl Crystallogr* 37:399–409.
154. Bowler MW, Montgomery MG, Leslie AGW, Walker JE (2006) Reproducible improvements in order and diffraction limit of crystals of bovine mitochondrial F₁-ATPase by controlled dehydration. *Acta Crystallogr D Biol Crystallogr* 62:991–5.
155. McCoy AJ et al. (2007) Phaser crystallographic software. *J Appl Crystallogr* 40:658–674.
156. Adams PD et al. (2010) PHENIX: a comprehensive Python-based system for macromolecular structure solution. *Acta Crystallogr D Biol Crystallogr* 66:213–221.
157. Afonine P V et al. (2010) Phenix.Model_Vs_Data: a High-Level Tool for the Calculation of Crystallographic Model and Data Statistics. *J Appl Crystallogr* 43:669–676.
158. V. Hámos L (1933) Röntgenspektroskopie und Abbildung mittels gekrümmter Kristallreflektoren. I. Geometrisch-optische Betrachtungen. *Ann Phys* 409:716–724.

References

159. Loll B, Kern J, Saenger W (2007) Lipids in photosystem II: Interactions with protein and cofactors. *Biochim Biophys Acta* 1767:509–519.
160. Renger G, Hanssum B (2009) Oxygen detection in biological systems. *Photosynth Res* 102:487–98.
161. Zouni A et al. (2005) Size determination of cyanobacterial and higher plant photosystem II by gel permeation chromatography, light scattering, and ultracentrifugation. *Biochemistry* 44:4572–81.
162. Broser M (2010) Purification, crystallization and structural analysis of the monomeric Photosystem II core complex from *Thermosynechococcus elongatus*. *Dissertation*, TU Berlin
163. Kawakami K, Umena Y, Kamiya N, Shen J-R (2011) Structure of the catalytic, inorganic core of oxygen-evolving photosystem II at 1.9 Å resolution. *J Photochem Photobiol B* 104:9–18.
164. De Las Rivas J, Barber J (2004) Analysis of the Structure of the PsbO Protein and its Implications. *Photosynth Res* 81:329–43.
165. Kouřil R, Wientjes E, Bultema JB, Croce R, Boekema EJ (2013) High-light vs. low-light: effect of light acclimation on photosystem II composition and organization in *Arabidopsis thaliana*. *Biochim Biophys Acta* 1827:411–9.
166. Kirchhoff H, Mukherjee U, Galla H-J (2002) Molecular architecture of the thylakoid membrane: lipid diffusion space for plastoquinone. *Biochemistry* 41:4872–82.
167. Kirchhoff H (2008) Molecular crowding and order in photosynthetic membranes. *Trends Plant Sci* 13:201–7.
168. Krissinel E, Henrick K (2007) Inference of macromolecular assemblies from crystalline state. *J Mol Biol* 372:774–97.
169. Renger T, Müh F (2013) Understanding photosynthetic light-harvesting: a bottom up theoretical approach. *Phys Chem Chem Phys* 15:3348–3371.
170. Van Amerongen H, Croce R (2013) Light harvesting in photosystem II. *Photosynth Res* 116:251–63.
171. Renger T, Schlodder E (2011) Optical properties, excitation energy and primary charge transfer in photosystem II: theory meets experiment. *J Photochem Photobiol B* 104:126–41.
172. Caffarri S, Broess K, Croce R, van Amerongen H (2011) Excitation energy transfer and trapping in higher plant Photosystem II complexes with different antenna sizes. *Biophys J* 100:2094–103.

References

173. Govindjee, van de Ven M, Preston C, Seibert M, Gratton E (1990) Chlorophyll a fluorescence lifetime distributions in open and closed photosystem II reaction center preparations. *Biochim Biophys Acta* 1015:173–9.
174. Deng X, Davidson WS, Thompson TB (2012) Improving the diffraction of apoA-IV crystals through extreme dehydration. *Acta Crystallogr Sect F Struct Biol Cryst Commun* 68:105–10.
175. Heras B, Martin JL (2005) Post-crystallization treatments for improving diffraction quality of protein crystals. *Acta Crystallogr D Biol Crystallogr* 61:1173–80.
176. Boutet S, Williams G (2010) The Coherent X-ray Imaging (CXI) instrument at the Linac Coherent Light Source (LCLS). *New J Phys* 12:035024.
177. Emma P et al. (2010) First lasing and operation of an Ångstrom-wavelength free-electron laser. *Nat Photonics* 4:641–647.
178. DePonte DP et al. (2008) Gas dynamic virtual nozzle for generation of microscopic droplet streams. *J Phys D: Appl Phys* 41:195505.
179. Ganan-Calvo AM, Montanero JM (2009) Revision of capillary cone-jet physics: Electro spray and flow focusing. *Phys Rev E* 79:066305.
180. Fridrikh S V., Yu JH, Brenner MP, Rutledge GC (2003) Controlling the Fiber Diameter during Electrospinning. *Phys Rev Lett* 90.
181. Sierra RG et al. (2012) Nanoflow electrospinning serial femtosecond crystallography. *Acta Crystallogr D Biol Crystallogr* 68:1584–7.
182. Hunter MS et al. (2011) X-ray Diffraction from Membrane Protein Nanocrystals. *Biophys J* 100:198–206.
183. Starodub D et al. (2008) Dose, exposure time and resolution in serial X-ray crystallography. *J Synchrotron Radiat* 15:62–73.
184. Barty A et al. (2011) Self-terminating diffraction gates femtosecond X-ray nanocrystallography measurements. *Nat Photonics* 6:35–40.
185. Kern J et al. (2012) Room temperature femtosecond X-ray diffraction of photosystem II microcrystals. *Proc Natl Acad Sci U S A* 109:9721–6.
186. Kern J et al. (2013) Simultaneous femtosecond X-ray spectroscopy and diffraction of photosystem II at room temperature. *Science* 340:491–5.
187. Shevela D, Messinger J (2013) Studying the oxidation of water to molecular oxygen in photosynthetic and artificial systems by time-resolved membrane-inlet mass spectrometry. *Front Plant Sci* 4:473.

References

188. Messinger J et al. (2001) Absence of Mn-Centered Oxidation in the $S_2 \rightarrow S_3$ Transition: Implications for the Mechanism of Photosynthetic Water Oxidation. *J Am Chem Soc* 123:7804–7820.
189. Debus RJ (2008) Protein Ligation of the Photosynthetic Oxygen-Evolving Center. *Coord Chem Rev* 252:244–258.
190. Iizasa M, Suzuki H, Noguchi T (2010) Orientations of carboxylate groups coupled to the Mn cluster in the photosynthetic oxygen-evolving center as studied by polarized ATR-FTIR spectroscopy. *Biochemistry* 49:3074–82.
191. Kern J et al. (2013) Simultaneous Femtosecond X-ray Spectroscopy and Diffraction of Photosystem II at Room Temperature. *Science Suppl. Material*

Danksagung

Mein größter Dank geht an meine Betreuerin Prof. Dr. Athina Zouni für ihre jahrelange Unterstützung und Motivation, sowie hilfreiche Besprechungen und Ratschläge. Außerdem ermöglichte sie mir die Teilnahme an vielen interessanten, internationalen Konferenzen, Kooperationen und Messreisen, die mir immer in besonderer Erinnerung bleiben werden. Ein großer Dank geht an meine komplette Arbeitsgruppe. Allen voran danke ich meiner langjährigen Kollegin Dr. Carina Glöckner, mit der mich viel Zeit im grün abgedunkelten Labor verbindet, aber auch gemeinsame Messzeiten und Konferenzen mit vielen schönen, unvergesslichen Erlebnissen und eine daraus entstandene Freundschaft. Dr Jan Kern und Dr Matthias Broser danke ich für die erste Einarbeitung im Labor und viele hilfreiche Ratschläge und Gespräche. Ein weiterer Dank geht an Dörte DiFiore für ihre Unterstützung durch unzählige PSII Präparationen und Messungen am PSII. Meinem ehemaligen Kollegen Dr. Joachim Frank danke ich für die angenehme erste Arbeitszeit und die wissenschaftliche Unterstützung. Dr. Frank Müh danke ich für die perfekte Mischung aus albernem Unterhalten in den Kaffeepausen und interessanten wissenschaftlichen Fachdiskussionen. Meiner lieben ehemaligen Kollegin Selcan Ceylan danke ich für ihre Unterstützung im Labor und ihre dabei stets positive, belebende Art. Mohamed Ibrahim danke ich für seine engagierte Zusammenarbeit im Labor und bei Messreisen. Danke auch an Ina Seuffert, die grad neu in den Arbeitskreis wechselte als ich mich in den letzten Zügen der Laborarbeit befand und mich sofort mit Rat und Tat unterstützte. Sabine Kussin danke ich für die zahlreiche Vorbereitung und Assistenz bei den BN-PAGE Experimenten.

Außerdem bedanke ich mich bei allen Kolleginnen und Kollegen im Max-Volmer Institut für ihre Unterstützung sei es durch nette Gespräche, das Ausleihen von Chemikalien oder das zur Verfügung stellen von Messgeräten. Danke an Lars Paasche für die meist sofortige Hilfe bei diversen technischen Problemen und für seine Backkünste.

Für die Zusammenarbeit mit den Kristallographen Dr. Albert Guskov und Dr. Azat Gabdulkhakov aus der Arbeitsgruppe von Prof. Dr. Wolfram Saenger und die darüber ermöglichten anfänglichen Messzeiten bedanke ich mich hiermit herzlich.

Vielen Dank an Dr. Chris Weise für die schnellen und sorgfältigen Durchführungen der massenspektrometrischen Messungen an PSII Proben.

In Gedenken an Prof. Dr. Gernot Renger bedanke ich mich für die heiteren Gespräche am Morgen und das Teilen seines immensen Wissensschatzes über Photosystem II.

Allen Kollegen der Arbeitsgruppe von Dr. Vittal Yachandra danke ich für die produktive Zusammenarbeit an unserem Kooperationsprojekt und die trotz hohem Druck durchweg positive Arbeitsatmosphäre. Danke an Dr. Jan Kern für seine

Danksagung

fachliche Unterstützung in den Messzeiten und die Bereitschaft während dieser Zeit bei seiner Familie zu wohnen, wo ich mich immer sehr wohl gefühlt habe.

Prof. Dr. Johannes Messinger danke ich für den angenehmen kurzen Forschungsaufenthalt in Umeå, sowie Sergey Koroidov für die Zusammenarbeit im dortigen Labor.

Ein großer Dank geht an Dr. Anja Burkhardt, die unsere Messzeiten am DESY stets sehr bemüht unterstützte. Zusammen mit Dr. Martin Warmer führte sie die HPF-Vorbereitungen durch und ermöglichte mir immer einen angenehmen Forschungsaufenthalt in Hamburg. Danke auch an Prof. Dr. Alke Meents für die bereitgestellte Messzeit und die Kooperation.

Vielen Dank an Prof. Dr. Holger Dobbek und seine Arbeitsgruppe für die nette Zusammenarbeit, die Bereitstellung des Kristallisationsroboters und das ermöglichen zahlreicher Messzeiten. Der größte Dank geht an Dr. Martin Bommer, der immer sehr engagiert und hilfsbereit als Kristallograph unseren Arbeitskreis bereicherte, für die Unterstützung in den zahlreichen Messzeiten, die umfangreiche Datenauswertung und Modellierung der neuen PSII Struktur. Weiterhin möchte ich mich für die sehr produktive Zusammenarbeit an unserer gemeinsamen Veröffentlichung bedanken.

Ein großer Dank geht an Prof. Dr. Thomas Friedrich (TU Berlin) und Prof. Dr. Bernhard Grimm (HU Berlin) für die sofortige Bereitschaft diese Arbeit zu begutachten. Vielen Dank an Prof. Dr. N. Budisa (TU Berlin) für den Prüfungsvorsitz zu dieser Arbeit.

Besonderer Dank geht an meine ehemaligen Kollegen und Freunde aus den Nachbararbeitskreisen, Dr. Sara Bruun, Dr. Neslihan Tavraz, Dr. Khoa Ly, Dr. Ingo Hoffmann, Dr. Murat Sezer und Francisco Valesquez-Escobar, für hilfreiche Gespräche und viele gemeinsamen Mensabesuche und Kaffeepausen. Bei meiner Familie, allen meinen Freunden und meinem Freund Niklas Alt bedanke ich mich für die andauernde Unterstützung.

Danke an Dr. Jan Kern, Dr. Martin Bommer und Dr. Sara Bruun für das Korrekturlesen von Teilen dieser Arbeit.

Schlussendlich bedanke ich mich für die Finanzierung dieses Projektes beim Exzellenzcluster UniCat (Teilprojekt B1).